2810376378

UNIVERSITY OF LONDON THESIS

Degree *PHD*   Year *2008*   Name of Author *BRANSON, JAMES ALEXANDER, DAVID.*

COPYRIGHT
This is a thesis accepted for a Higher Degree of the University of London. It is an unpublished typescript and the copyright is held by the author. All persons consulting the thesis must read and abide by the Copyright Declaration below.

COPYRIGHT DECLARATION
I recognise that the copyright of the above-described thesis rests with the author and that no quotation from it or information derived from it may be published without the prior written consent of the author.

LOAN
Theses may not be lent to individuals, but the University Library may lend a copy to approved libraries within the United Kingdom, for consultation solely on the premises of those libraries. Application should be made to: The Theses Section, University of London Library, Senate House, Malet Street, London WC1E 7HU.

REPRODUCTION
University of London theses may not be reproduced without explicit written permission from the University of London Library. Enquiries should be addressed to the Theses Section of the Library. Regulations concerning reproduction vary according to the date of acceptance of the thesis and are listed below as guidelines.

A.   Before 1962. Permission granted only upon the prior written consent of the author. (The University Library will provide addresses where possible).

B.   1962 - 1974. In many cases the author has agreed to permit copying upon completion of a Copyright Declaration.

C.   1975 - 1988. Most theses may be copied upon completion of a Copyright Declaration.

D.   1989 onwards. Most theses may be copied.

☐   This copy has been deposited in the Library of _____*UCL*_____

☐   This copy has been deposited in the University of London Library, Senate House, Malet Street, London WC1E 7HU.

Propagation Modelling for the Analysis of Radar Systems

James Branson

A dissertation submitted in fulfilment

of the requirements for the degree of

Doctor of Philosophy

of the

University of London

Department of Electronic and Electrical Engineering

University College London

April 24th, 2008

UMI Number: U592569

UMI

Dissertation Publishing

UMI U592569

ProQuest

I, James Branson, confirm that the work presented in this thesis is my own. Where information has been derived from other sources, I confirm that this has been indicated in the thesis.

Abstract

It is well understood in the defence procurement industry that there is a shortfall in the understanding of military mobile radar system performance in complex meteorological environments. To meet this challenge, the work presented in this thesis has combined advanced radar propagation methods with a novel clutter modelling algorithm to describe system performance at the level needed to meet modern naval requirements. The need for these new methods is demonstrated by sets of data gathered in anomalous propagation (anaprop) environments by the author. A new flexible radar model created during this project has allowed the author to analyse the radar data taken and to explore the benefits of performance modelling of radar systems in complex littoral and anaprop environments. A prototype system that exploits the model to try to estimate the local conditions has also been developed. Tests on this technology demonstrator have indicated that more advanced applications of these techniques could allow future radar systems to sense their local environment to improve tactical awareness and enhance sensor optimisation.

Acknowledgements

Novel Research

This thesis presents a systems approach which has extended existing methods and combined them to produce a new analysis tool. The novel research carried out during this work is outlined in this section.

Section 4 of this thesis presents a unique set of baseband radar data collected from an operational radar system in anomalous propagation conditions. The radar data environment was simultaneously sampled by GPS instrumented radiosonde launches and other meteorological data which was another first from an operational RN platform.

Section 5 details a new radar model (named NEMESiS) which has been designed and coded in Matlab that combines a cutting edge parabolic equation propagation model with a detailed but generic system model. This model was one of the first that could create three dimensional probability of detection plots showing radar performance in realistic scenarios. Uniquely for a generic radar propagation model, a number of important system effects have been added to show critical radar effects of anomalous propagation.

The model uses a novel surface effects algorithm developed during this project (see section 5.3.1). For the first time this algorithm allows clutter strength to be derived directly from a parabolic equation propagation model. (Other similar models have to make use of ray tracing and subsidiary techniques.) This new capability allows more consistent radar environment modelling.

The analysis of the radar trials data using this new model (Section 6) has improved the understanding of anaprop trials data and validated that the NEMESiS method can show the effects of the environment on radar systems.

The accuracy and realism of the clutter model have allowed a new environmental inversion algorithm for rapid environment assessment to be created and assessed as detailed in section 7.

Publications arising from the research

During the research described in this document the author contributed to and presented a large number of reports and papers based on the work to the MOD and to various conferences. Some of the most important publications are detailed below. The MOD reports listed below are unpublished.

Dec '96   Branson, J. *Comparison of Naval Radar Propagation Models,* DERA report for MOD

Mar '97   Mabogunje, A. Branson, J. *DLQ trials report,* HMS Richmond radar trials report prepared for the MOD, DERA/SSWI/WP97027/A

Sep '97   Money, D.G. Branson, J. Hooker, M. Mabogunje, A. 'Radar littoral environment predictions and measurements', *Radar 97,* IEE Conf. Pub. No. 449, 164-168

July '98   Branson, J. 'Tropospheric propagation and applications to environmental inversion', *IEE Radar and Sonar Signal Processing meeting* paper

Aug '98   *Radar detection in littoral conditions,* Magazine article in the *Review of Naval Engineering,* Vol. 51 No 4, Summer '98

Apr '00   Branson, J. *The Effects of Anomalous Propagation on SAMPSON Performance,* MOD customer report, DERA/SS/AWS/TR000061

Jun '00   Branson, J. *Environmentally Aware Radar Research,* Paper presented to NATO Workshop

Aug '01   Branson, J. *Clutter Collection at Whale Island Using The MPBR,*
           Trials Plan and Analysis using NEMESiS, QINETIQ/FST/MCSC/
           TI011279

Jun '02   Branson, J. *Environmentally Aware Future Radar Research,*
           Journal of Defence Science paper (this paper won a JDS annual
           award for novel research)

Oct '02   Branson, J. Dawber, W. & Wooding, S. 'Modelling of the littoral
           environment for real-time radar performance assessment',
           RADAR 2002, 15-17 Oct. 2002 Page(s): 41 - 46

Jan '03   Branson, J. *Synthetic Environments for Radar Acceptance,*
           QINETIQ/FST/CR0300489/1.0,

Apr '03   Branson, J. *Naval Environmental Clutter Attenuation and
           Propagation Specification.* DERA/SS/CS/WP000023/1.0
           (Standard clutter specification used industry wide for maritime
           surveillance radar programmes)

May '05   Dawber, W. & Branson, J. 'Use of site specific radar modelling to
           improve CFAR performance in the littoral', *IEEE International
           Radar Conference,* 2005, 9-12 May 2005, Pages:161 - 166

Oct '06   Appleton, S. & Branson, J. 'Stealthy Wind Turbines: - addressing
           the radar issue', QinetiQ Ltd, *British Wind Energy Association
           conference, 2006*

Apr '07   Dawber, W.N. Hunter, G.J. Branson, J.A. Modelling of Adaptive
           Multifunction Radars for Trials Planning and Acceptance, *Radar
           2007,* 17-20 April 2007, Pages: 396-401

Contents

List of Figures

Acronyms

AEGIS	US Navy phased array radar based combat system
Anaprop	Anomalous propagation
AOA	Angle of arrival
APM	Advanced propagation model
ARM	Anti-radiation missile
AREPS	Advanced refractive effects prediction software
CFAR	Constant false alarm rate
CPLD	Complex programmable logic device
CVS	Concurrent versions system
DCS	Ducting climatology summary
DLQ	Designation of HMS Richmond radar trial
DMX	Designation of HMS Illustrious radar trial
DTED	Digital terrain elevation database
Easat	Radar systems company
EMCON	Emission control
ENVAR	Environmentally aware future radar research
ESM	Electronic surveillance measures

FFT	Fast Fourier transform
GIT	Georgia Institute of Technology
GPS	Global positioning system
GUI	Graphical user interface
HMS	Her Majesty's ship
IREPS	Integrated refractive effects prediction software
Matlab	Matrix maths analysis and visualisation tool
MFR	Multifunction radar
MTD	Moving target detector
MTI	Moving target indicator
NaRCoSiS	Naval radar computer simulation suite
NECAPS	Naval radar environment clutter, attenuation and propagation specification
NEMESiS	Naval electromagnetic environment simulation suite
NR	Normal radar
OTH	Over the horizon
PCPEM	Personal computer PEM
PE	Parabolic Equation
PEM	Parabolic equation model

PDF	Probability density function
PPI	Plan position indicator
PRF	Pulse repetition frequency
PRI	Pulse repetition interval
Radar	Radio detection and ranging
RADAS	Radar data acquisition system
RAF	Royal Air Force
REA	Rapid environmental assessment
RCS	Radar cross section
RN	Royal Navy
SCR	Signal to clutter ratio
SNR	Signal to noise ratio
SNCR	Signal to noise plus clutter ratio
SRTM	Shuttle radar tomography mission
STC	Sensitivity time control
SPAWAR	Space and Naval Warfare Systems Command
T996	Current RN surveillance radar in use throughout the fleet
TEMPER	Tropospheric electromagnetic parabolic equation routine
TERPEM	Signal Science Ltd PEM model

TNR   Threshold to noise ratio

TOGA-COARE   Boundary layer meteorological model (long acronym)

UCL   University College London

1 Introduction

There is a shortfall in the understanding of radar system performance in complex meteorological environments. This is especially a problem for military mobile radar systems which have to deal with a wide variety of changing environments. This document describes research into helping to solve this problem by creating a better understanding of how environmental conditions have an impact on complex sensor systems. This chapter sets out the background and history of radar systems.

1.1 Summary of aims

This work aims to:

- Collect radar data in anomalous propagation (anaprop) environments

- Develop a new computer model capable of simulating the effects of anaprop on the whole radar system

- Use this model to analyse the trials data to define the critical anaprop phenomena that affect fundamental radar performance

- Use the model to develop a candidate solution to a current radar system performance shortfall.

1.2 A brief history of radar

The concept of using radio waves to build up a picture of the surroundings was first considered by Hertz in the 1880s and he demonstrated reflection of radio signals by electrical conductors.

Radar, in its simplest form, takes this concept much further by sending out a short pulse[1] of radio waves from an antenna. The received signal, which arrives back at the antenna due to backscatter from the environment, is then broken up the into discrete steps in time. As radio waves travel at a known speed, the speed of light, these time steps are equivalent to range steps. The distance to any objects causing backscatter can therefore be measured by seeing which range bins have the largest signal strength. The position of these objects can then be derived by combining this range information with the direction that the antenna was being pointed in. This simple principle gives radar its name: RAdio Detection And Ranging (although the name wasn't coined until the 1940s, almost 40 years after its inception).

The first patents for a radar like device were registered early in the 1900s but the first real demonstrations of radar principles were in the late 1920s. From then until the outbreak of World War II (WW2) many countries researched ways to use radio waves, with wavelengths of around a metre, to search for ships and aircraft. In Great Britain this culminated in the huge Chain Home system that protected the coastline of England during the Battle of Britain. The antennas of one Chain Home station are shown in Figure 1-1.

---

[1]Not all radar systems use pulsed energy. Some systems transmit continuously and reconstruct an equivalent picture to a pulsed radar by clever processing (e.g. FMCW radar).

Figure 1-1 Chain Home antennas

At the beginning of the war, British radar technology was much more primitive than German systems. However, early in 1940, a critical step forward was by made Randall and Boot at Birmingham University. They enhanced existing designs for the cavity magnetron (ironically this was originally developed in Germany by Hans Hollmann but the technology was not supported by the German military) to generate high power, short wavelength (~10cm) microwaves. Their first cavity magnetron is shown in Figure 1-2.
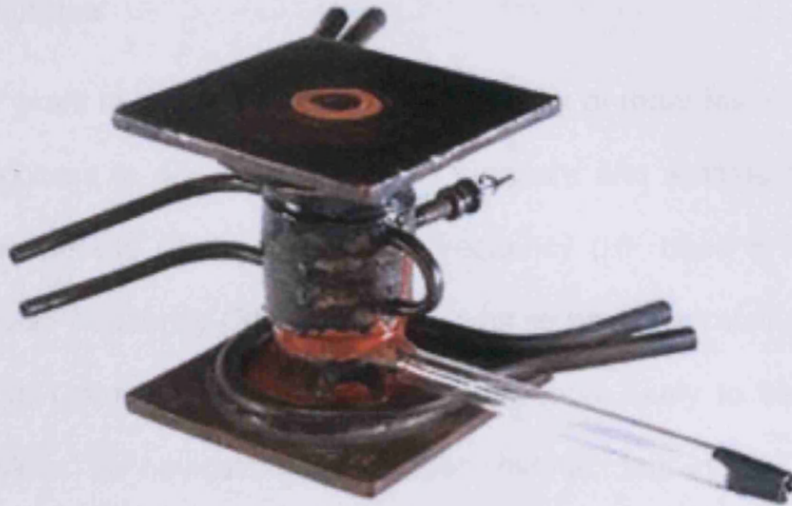
Figure 1-2 The original 1940 cavity magnetron developed by Randall and Boot (Courtesy of Science Museum/Science & Society Picture Library)

The magnetron increased the power of microwave sources by several orders of magnitude and this meant that radar systems could be made that were smaller, more efficient and more mobile. A lack of the resources needed to properly take advantage of the magnetron led to it being shared with the US. In a major effort on a similar scale to the creation of the atomic bomb at Los Alamos, some of the best US scientists and engineers were teamed together at the newly created MIT Radiation Lab. During the remainder of the War, this lab provided rapid advances in radar capabilities and developed many new radar systems which military historians believe had an important influence on the outcome of the War. The types of systems created during this intense period of development have been steadily refined and improved during the Cold War to produce the sensitive, integrated systems that are used today.

1.3   The radar system

In the early years of WW2 the Chain Home system of radar towers was critical to British success in dealing with enemy bombers and winning the Battle of Britain. However the Chain Home high frequency (HF band is in the range 3-30MHz) radio-frequency (RF) technology was so primitive, relative to German systems, that German analysts thought it was more likely to be involved in communications or navigation than radar. Indeed, individual Chain Home stations only gave a fairly basic idea of incoming raids and so its success was not just down to the individual radar antenna sites themselves. Its strength came from the complex system of reporting, tracking, decision making and finally fighter airfield designation that followed. Much of this took place at the Royal Air Force's (RAF's) Filter Rooms (see Figure 1-3) and it was there, rather than in the radar design, that British innovation was superior to the German equivalent. The German Luftwaffe didn't develop effective procedures and systems for using their more technically proficient radar technology [Clark, 1997].
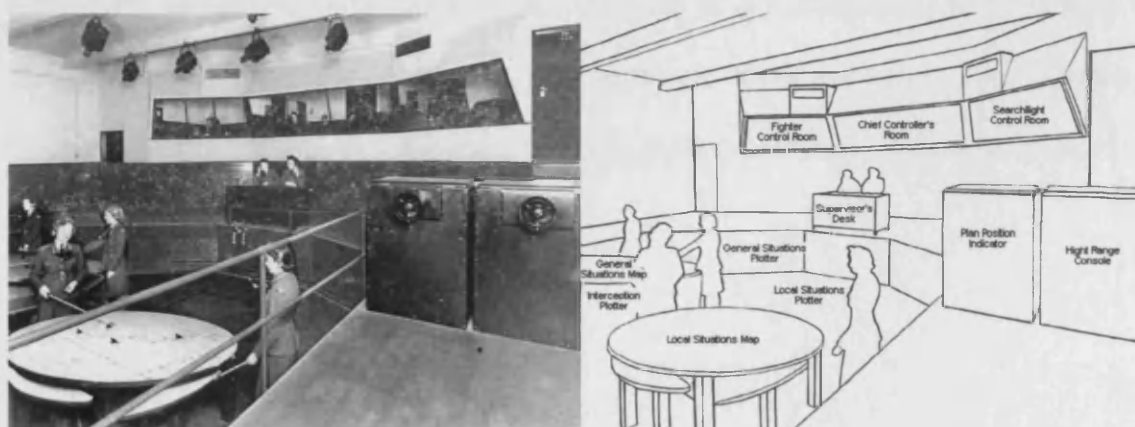
Figure 1-3 Layout of an RAF Filter room

Much of the development work on radar since WW2 has concentrated on enhancing the radar 'system'. The system is no longer spread through different geographical locations, but has been reduced in size to a few cabinets of RF electronics and digital signal processors to provide filtered information at the fingertips of the radar operator. This is normally achieved by condensing the raw information gathered by the radar firstly into plots and then tracks and ultimately into decisions on how to treat incoming targets.

Modern military radar systems gather a huge amount of data, the equivalent of hundreds of Megabytes per second. This data stream has to be pared down to a very simple set of continuous target tracks to reduce the information that the operators have to deal with and allow their commanders to make the best decisions. The radar must continue to detect and track a hostile target through clutter (unwanted backscattered returns) and fades (loss of target signal) and then pass on the track information to a weapon system which will often take over the tracking function as the first stage of engaging the target.

A modern defensive radar system is made up of a transmitter, an antenna, a receiver, signal processor, detector, plot extractor, track extractor, and a display to visualise the results. A simplified flow diagram of a radar system is shown in Figure 1-4.
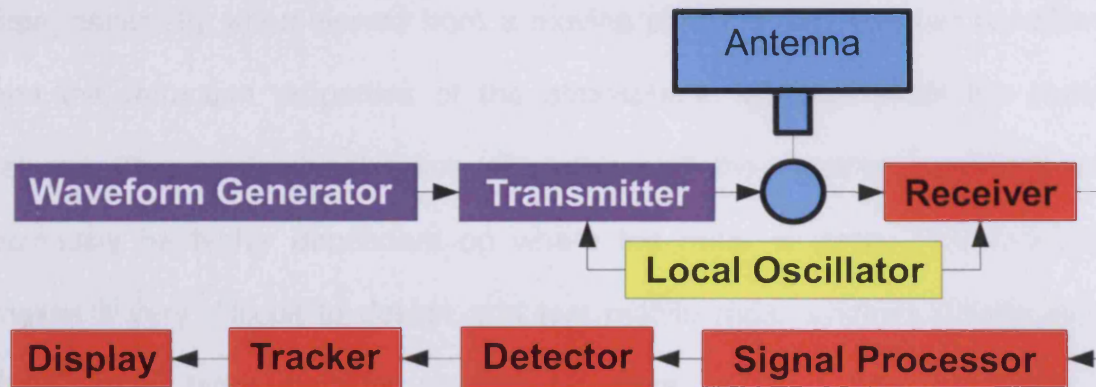
Figure 1-4 Parts of a typical radar system

Bespoke hardware and experienced radar operators have traditionally been needed to handle this data stream. However, as computer processing has become faster and cheaper, digitisation of the radar has crept further into the radar system making the radar output simpler to understand for less skilled operators.

As radar systems have become more sensitive, their ultimate performance has become limited by the effects of the environment. The effects may be small but they can be amplified by the design of the radar system. These system effects will be examined in this thesis.

1.4   The radar environment

Radar systems aim to filter the continuous stream of data that they receive to provide an operator with information about a small number of relevant target objects. This job is complicated by radar backscatter from everything else in the vicinity of the radar. These unwanted returns are termed clutter and can include reflections from the sea surface, rocks, buildings, rain, and birds. Clutter is highly specific to the scenario in which the radar is being used and it varies with

time, especially when viewed from a moving platform. The weather conditions and the refraction properties of the atmosphere will also affect the clutter returns. The predominant types of clutter and the weather conditions will obviously be highly dependant on where the radar is used. This variability makes it very difficult to design and test mobile radar systems [Watts et al, 2002]. New radar systems tend to be more sensitive than the previous generation and so new unexpected clutter effects will limit the achievable performance.

1.5 Naval radar systems

Military naval platforms provide difficult challenges for their radar systems. Ships have available power and weight carrying capability to allow radar engineers free rein (apart from cost) in designing the most sensitive systems. A number of different radar systems are usually deployed on each ship to perform a variety of tasks. The ship may also be required to sail to different environments and operate in all sorts of mission roles.

During the Cold War, Royal Navy (RN) ship design was based around a North Atlantic role combining convoy protection and submarine detection (for example the Type 23 Frigate shown in Figure 1-5). The radar system requirements reflected this and so radar systems were designed to detect small fast moving targets (missiles and fast jets) against a background of sea clutter when the ship was situated in the deep ocean. The environmental challenges in this theatre were limited to heavy seas and storms of rain and ice.

These ship designs were seriously tested during the Falklands Conflict. A Task Force of ships was sent out to the Falkland Islands carrying troops and supplies to retake the Islands from the Argentine occupation force. The main threat to the ships would be from fast jets carrying bombs and anti-ship missiles. The most formidable threat came from the Excocet missile which was small and fast enough to provide a significant challenge to the weapon systems on the ships.

To support the landing of troops on the Falkland Islands the task force had to move in close to land. In this environment the commanders knew that their radar and other defensive systems would be hampered by land clutter (which they weren't designed to deal with) and so a landing bay was chosen where hills and cliffs would partially screen the ships from air attack. Land based weapon systems (the land based Rapier system was eventually deployed) and Harrier jets were used to plug the defensive holes. Even so, several ships were sunk and one of the lessons learnt was that more flexible shipborne radar systems (and weapons systems) were needed that could perform well when close to land in the littoral zone.

Figure 1-5 The Type 23 Frigate carries four different radar systems including the T996 radar atop its main mast

Since the end of the Cold War the old requirements for Atlantic operation have all but disappeared and there is now a need for more flexible systems that can adapt to new missions and roles.

More recent operations in the Persian Gulf have shown the extra problems caused by extreme environments. Ship radar systems are necessarily sited close to the sea in a region of complex meteorology called the boundary layer. As will be described later, radar performance can be affected inside this layer.

The requirements for modern flexible radar systems (such as the SAMPSON radar system developed for the RN's Type 45 Destroyer shown in Figure 1-6) capable of dealing with all of these new problems are so diverse that procurement processes also need to be revised. Testing and acceptance of these systems is now a critical challenge for MOD and advanced modelling is one of the most important tools in the modern procurement process [Watts et al, 2002].

Figure 1-6 Type 45 Destroyer HMS Daring showing off her egg-like SAMPSON radar during sea trials

1.6   History of radar modelling

Radar modelling has developed in parallel with radar systems. However the speed of bespoke hardware in a radar system coupled with the complexity of the radar environment has meant that radar modelling has always lagged behind real systems and so did not usually predict radar performance very realistically. Lack of good models means that it is difficult to understand how a radar will perform until it is delivered and working in theatre. This has contributed to procurement problems for a number of UK radar systems [National Audit Office, 2000].

Over the last decade this gap has been closing because of the rise in computer processing speed which has lead to radar systems becoming more software based and so easier to model whilst the models have become quicker and more complex.

Radar modelling has its roots in Maxwell's equations that describe the transmission of radio waves through the atmosphere. These equations are too complicated to solve in most realistic cases and many simplifications must be made to make calculations possible.

The radar equation described in section 2.1 is the simplest solution to Maxwell's equations for an isotropic emitter in free space. During WW2, physicists and engineers in the US and the UK refined the radar equation to help with the rapid development of various radar systems [Kerr, 1965]. However, they noticed that radar performance was often worse than that predicted by their models. A

number of approaches have been used in an attempt to solve this inconsistency. Probabilistic methods were introduced to model how random noise in the radar receivers and clutter returns from the environment around the radar influence radar detection [Blake, 1980]. More complex propagation models, which produced better solutions to Maxwell's equations, were also developed. However these models became too complicated to solve efficiently and so the refined radar equation approach remained the only way to compare radar performance.

As computing power has improved and a larger body of radar data have been analysed, radar models have become steadily more sophisticated. Probabilistic models still form the backbone of system modelling, whilst enhanced propagation models are used to examine the effects of the environment, and detailed modular simulations can be used to develop improved signal processing algorithms.

1.7 Propagation modelling

Radar models have used a number of approaches to model the propagation of radio waves through the atmosphere. These algorithms all aim to model the effect of varying refractive index on the passage of radio waves above a spherical reflecting surface which can also vary in roughness and height depending on the sea and land scenario to be modelled. The approaches trade accuracy against calculation speed and the flexibility to model a wide range of scenarios. These algorithms have often been developed in parallel with those

used for modelling sonar propagation (there are even combined sonar and radar conferences that feature propagation and other common research topics [IEE Mtg, 1998]) although the sonar problem is more challenging due to the more complicated refractive environment and sound wave dispersion.

1.8 Thesis structure

This chapter introduces the topic by looking at the history of radar and radar modelling. Chapter 2 sets out some of the basic theory of radar propagation, defining some basic concepts and looking at structures in the atmosphere that lead to a phenomena called anomalous propagation, or anaprop, before looking at how radar propagation is modelled. Chapter 3 examines the propagation models used by researchers around the world and highlights the lack of good radar data and the problems with current radar simulations. Chapter 4 describes a set of trials aimed to gather anaprop radar data and chapter 5 describes the model developed by the author to overcome some of the problems with current radar modelling. Chapter 6 shows how this model has been used to analyse the trials data detailed in chapter 4 and examines the effects of anaprop and the radar system problems that it can cause. Chapter 7 describes how the model has been applied to providing rapid environmental assessment and looks at exploiting anaprop effects. The remaining sections summarise the conclusions from this study, highlight where further work is needed and examine if the work has achieved its aims.

2 Theoretical Background

This chapter reviews the basic theory of radar propagation and how microwaves are influenced by common atmospheric refraction structures. The most important detrimental effect of the environment on radar performance is clutter backscatter. The types of clutter and the ways that they are modelled are described in section 2.7. Some of the signal processing algorithms that are normally used in radar systems and can be compromised by refractivity effects are presented in section 2.8. The chapter also discusses how different types of radar model implement different levels of sophistication in describing refraction, clutter and radar system effects. The most advanced of these types are examined and compared in chapter 3 and developed further into the model described in chapter 5.

2.1 Radar propagation basics

In a radar detector the mean power received from a target is the critical parameter for modelling whether that target would be detected. The *radar equation* is a model for calculating the power received for analysing the performance of simplified radar systems in basic environments. The form of the equation is derived by applying the principle of *conservation of energy* to an isotropic radar emitter in free space (Point A in Figure 2-1). A short pulse of energy from this emitter will propagate outwards in a spherical shell, represented by the red circle, at the speed of light.

$P_A = P_{Transmit}$	$P_B \propto \dfrac{P_{Transmit}}{R^2}$	$P_A \propto \dfrac{P_{Transmit} \cdot \sigma}{R^4}$
1. RF pulse transmitted from A	2. Pulse reaches target B Pulse absorbed and remitted	3. Reflected pulse reaches A
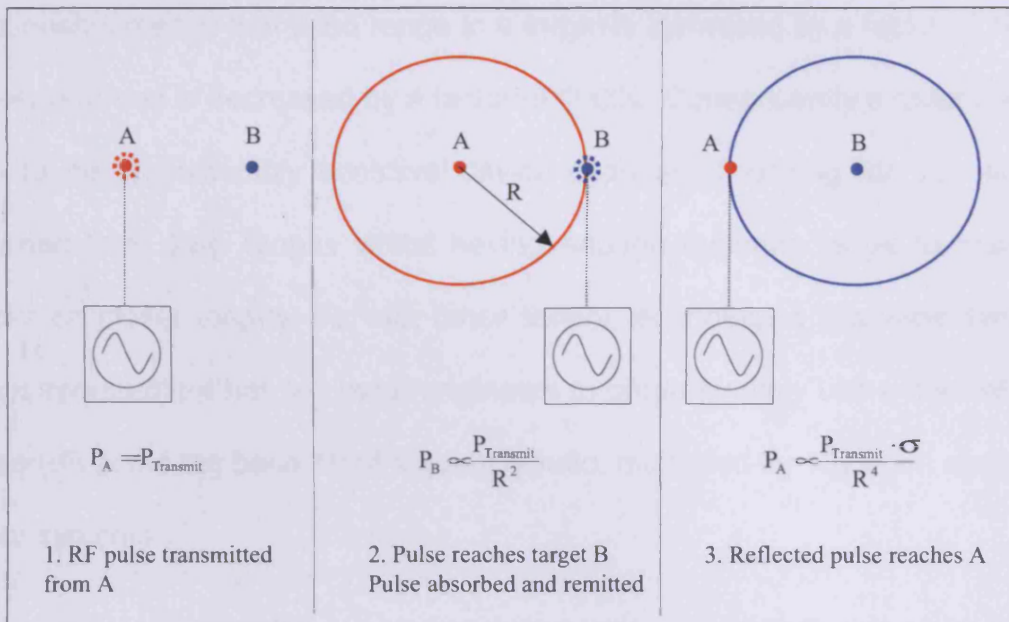
Figure 2-1 Radar Equation Fundamentals

The total power must be conserved and so the power density at a point reflector (marked B in the figure) on the shell's surface will be inversely proportional to the surface area of the shell and so proportional to the reciprocal of the range squared. Some of that power will be reflected by B (the proportion reflected is represented by B's radar cross section, RCS, σ) leading to a two-way propagation and so, to calculate the power returned back to the radar at A, this relationship needs to be squared. So in freespace the received power (P_r) decreases at a rate proportional to the reciprocal of the range (R) to the fourth power.

$$P_r \propto \frac{1}{R^4}$$

Equation 2.1

If the returned power is significantly greater than the noise power inherent in any radar system then the target should be detected. Radar systems have to be capable of detecting targets over a wide range of signal strengths. The above

relationship means that if the range to a target is increased by a factor of 10 the power returned is decreased by a factor of 10000. Consequently a radar system has to be an incredibly sensitive device capable of looking for tiny signals returned from long ranges whilst having enough dynamic range to maintain tracks on closer targets. As with other sensor technologies this wide dynamic range requirement has led radar engineers to predominately use a decibel (dB) scale (dB is the log base 10 of a quantity ratio, multiplied by 10) when analysing radar systems.

More detailed analysis of the radar equation, given in radar textbooks [e.g. Skolnik, 1986, Blake, 1980, Skolnik, 1970, Barton, 1990, Kerr, 1965], leads to the following more complicated equation for the power received by the radar from a target:

$$P_r = \frac{P_t G_t G_r \lambda^2 \sigma}{(4\pi)^3 R^4 L} \cdot F(R,z)^4 \qquad\qquad \textit{Equation 2.2}$$

Most of the terms in this equation are not relevant to the understanding of radar propagation and so are are not defined here (the radar textbooks referenced above describe the other terms in detail). What is important for this work is that the right hand side of the equation breaks down into two parts. The terms contained in the fraction are all defined for a given radar system and target. They represent an isotropic[2] emitter in freespace. These parameters are unaffected by the environment around the radar. The rest of the equation, $F(R,z)^4$, where z is target height above the ground, is a modulation of the

---

[2]An isotropic emitter exhibits the same intensity regardless of the direction of measurement

freespace result to account for non-isotropic effects which include the antenna pattern, reflections from the earth's surface, refraction, and diffraction. This modulation is called the *propagation factor*.

For a shipborne radar system, reflection of energy off the flat sea surface (called multipath) causes the propagating energy to form an interference pattern of standing waves. This gives a fixed spatial pattern of peaks and troughs. Reflected returns for objects moving through this pattern can be up to a factor of sixteen, or twelve dB, more than the freespace radar equation would predict. Figure 2-2 demonstrates this effect with a graph of how the propagation factor for a target would oscillate between −40 and +12 dB if it travelled at a constant height towards a radar antenna.
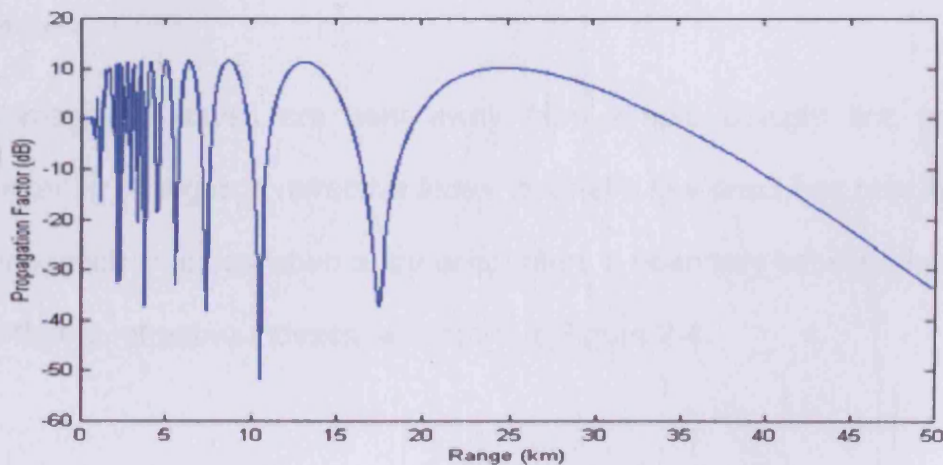
Figure 2-2 Multipath effects

Figure 2-3 shows this effect in two dimensions (Figure 2-2 is a single 1D slice through this 2D pattern). The figure is a range along the ground versus height plot, or coverage plot, with propagation factor proportional to the colour scale on the right of the main graph. The multipath lobes are clearly visible as red areas

in this standard atmosphere (as defined in section 2.2) simulation. Note that the x-axis of this graph represents the curved earth's surface which has been bent upwards to fit to a straight line. This has the effect of curving the multipath lobes upwards as well.
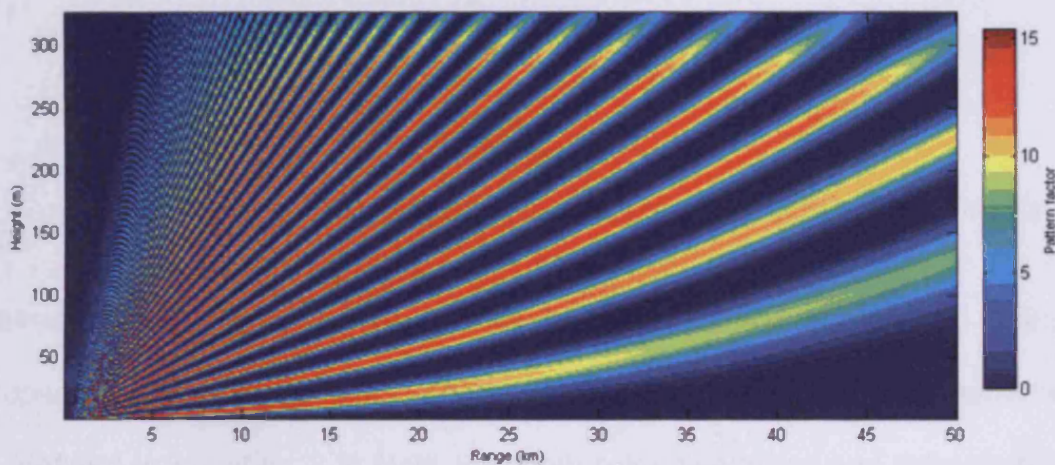
Figure 2-3 Standard atmosphere propagation factor coverage diagram

2.2 Refraction

Electromagnetic waves are bent away from simple straight line paths on encountering changes in *refractive index, n*. Snell's law describes how the angle of propagation changes when a ray encounters a boundary between two media with different refractive indexes, as shown in Figure 2-4.
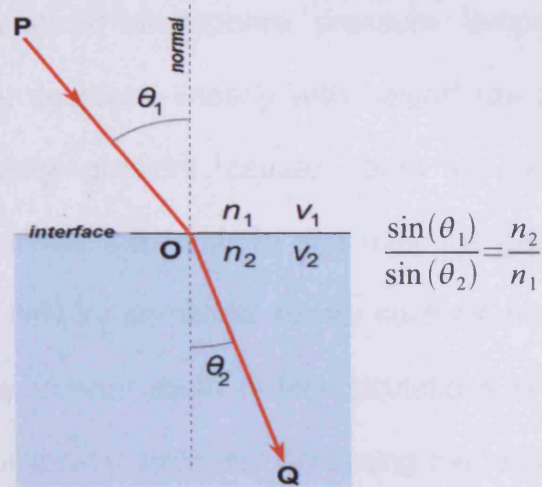
Figure 2-4 Bending of electromagnetic ray according to Snell's law

Refractive index is often very close to one and so to highlight changes propagation analysis generally often uses a related quantity called *refractivity*, N, defined in equation 2.3. Note that both refractive index and refractivity are dimensionless quantities.

$$N = (n-1) \times 10^6$$ *Equation 2.3*

In the lowest part of the atmosphere, the atmospheric boundary layer, refractivity is a complicated function of the bulk atmospheric properties: pressure, temperature and humidity (defined in Equation 4.1). These bulk properties change with altitude and so to understand their effects on propagation they must be measured as a function of height by using a meteorological balloon radiosonde. Fortunately refractivity usually varies fairly slowly with distance and so one vertical profile can often be assumed to apply over a relatively wide area, especially over the ocean.

In a 'standard' fully mixed atmosphere, pressure, temperature, humidity, and therefore refractivity decrease linearly with height[3] (as shown in Figure 2-7). This weak refractivity gradient causes radio waves to curve gradually downwards which allows the radar to see over the geometrical horizon that would be the range limit for an optical sensor such as a camera. To account for this extra curvature, curved earth radar calculations are usually modified to extend the radar horizon by artificially increasing the radius of the earth by one third. Simple geometry[4] shows that for a video camera at a height of 25m the horizon would be at 17.8km, but for a radar at the same height the horizon would be 20.6km

In reality, this simple picture of refraction is complicated by changes in the atmosphere that cause the temperature or humidity gradient to deviate from the fully mixed model. This leads to changes in the refractivity gradient and therefore the curvature of radio waves. In *sub-refracting* conditions, often encountered in weather conditions that also lead to fog, upward curvature is increased so that the radar horizon becomes decreased. More commonly *super-refracting* conditions cause the downward curvature of radio waves to be enhanced and so the radar horizon will increase.

It is important to note that only low angle coverage is altered by refraction effects. Radio waves propagating at angles of greater than one degree from the horizontal will not be strongly affected by the weak refractivity structures found

---

[3] Bulk parameters actually follow an exponential relationship with height but a linear approximation is accurate enough for the lower atmosphere

[4] horizon range $\approx \sqrt{(2 \times \text{radius of earth} \times \text{sensor height})}$

in our atmosphere. However, as the low angle coverage region affected contains surface clutter and the all important sea-skimming targets, refraction can have a major effect on military radar performance.

2.3 Ducting and anaprop

Strong super-refraction can cause the bending of the radio waves to exceed the curvature of the earth's surface so that the radar horizon becomes infinite. The waves are effectively trapped in a radio *duct*, repeatedly reflecting off the earth's surface before curving back downward to be reflected again. This is shown in Figure 2-5 by the energy below 100 metres becoming curved over and trapped in the duct. Any propagation effect (such as ducting) which creates unexpected performance in a radio wave system is referred to as anomalous propagation or *anaprop.*
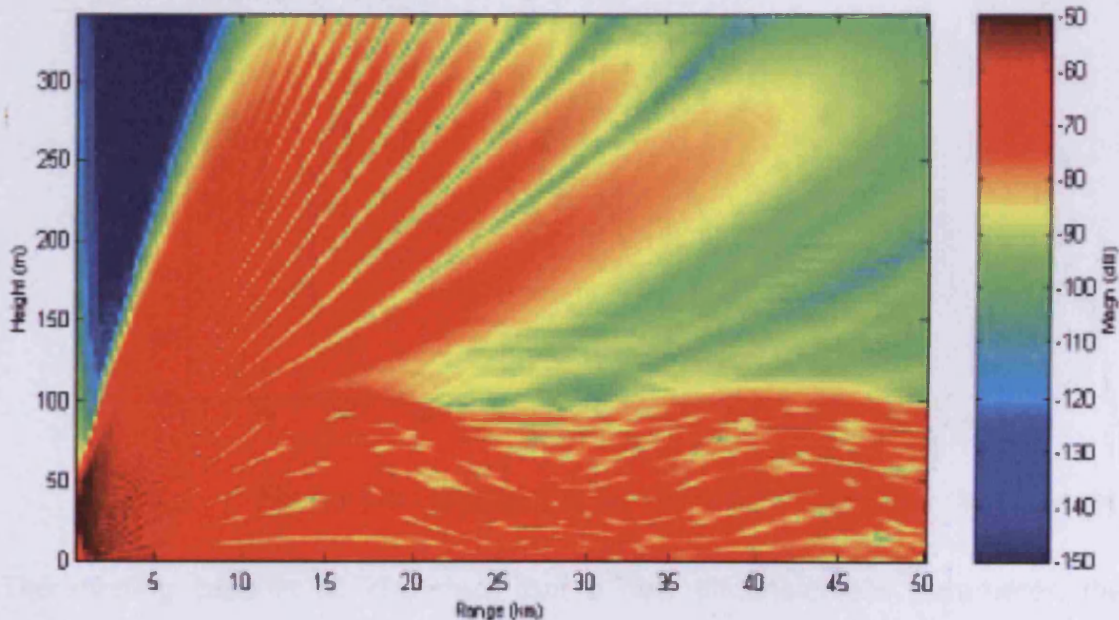
Figure 2-5 Strong ducting propagation coverage diagram

Inside the duct the simple assumptions that lead to the basic radar equation are no longer true. A trapped energy pulse propagates outward in a cylindrical shell so that two-way returned power is proportional to the reciprocal of the range squared and no longer the range to the fourth power. This makes a huge difference to the returns from low targets and clutter within the duct. In this $1/r^2$ regime, propagation factors can theoretically become very large, hundreds of times larger than in standard conditions. Figure 2-6 shows a plot of propagation factor with range inside a duct. Due to the high values simulated, the y-axis is in dBs. Comparison of both Figure 2-2 with Figure 2-6 and Figure 2-3 with Figure 2-5 indicates that target returns could be tens of dBs larger inside a duct. However, similar increases in surface clutter will mean that system performance could actually be degraded despite the increase in target signal strength.
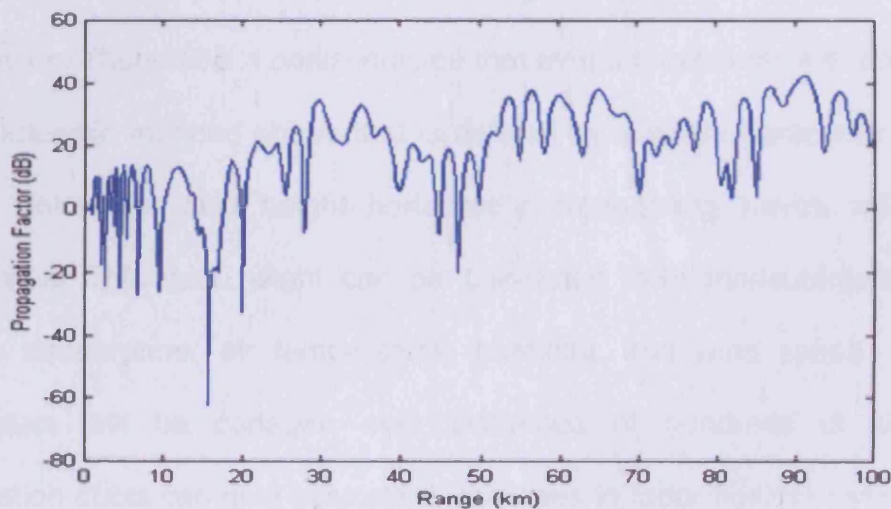
Figure 2-6 Propagation factor versus range for a ducting case

The ducting case is so important that a new dimensionless parameter, the *modified refractivity (M)* [5], is defined so that a negative modified refractivity

---

[5] M = (refractive index –1+height/radius of the earth) $\times 10^6$

gradient indicates the presence of a duct. A graph of modified refractivity versus height for a standard atmosphere would be a straight line with a positive gradient of around 11 M-units per kilometre and a value at the sea surface of around 300 to 350 M-units (as shown in Figure 2-7).

2.4 Types of duct

Evaporation ducts are very common in the maritime environment [Paulus, 1990]. Studies have shown that a weak evaporation duct is more common than the so-called 'standard' atmosphere even in cold climates like the North Atlantic [METOC, 1994]. These ducts are caused by the rapid changes in temperature and humidity close to the sea surface. These effects lead to the formation of a duct that may extend up to around 50 metres in height. Even in coastal scenarios, the evaporation duct is likely to be the dominant anaprop mechanism. Theoretical models indicate that evaporation ducts will tend to have a characteristic rounded shape that is defined by a single parameter, the *duct height*. Below the duct height horizontally propagating waves will be bent downwards. This duct height can be calculated from measurements of sea surface temperature, air temperature, humidity, and wind speed. As these parameters will be constant over distances of hundreds of kilometres, evaporation ducts can give consistent increases in radar horizon range for long periods of time.

Figure 2-7 compares the modified refractivity versus height profiles, or M-profiles, of a 'standard' atmosphere and a 15 metre evaporation duct over the

first 100 metres above the sea surface (The theoretical form of the evaporation duct is given in chapter 7 in equation 7.1). The plot of the evaporation duct shows that the first 15 metres of altitude the gradient of M is negative and so radio waves will be bent downwards, back towards the surface of the Earth. If radio waves were transmitted from below 15 metres in this atmosphere or were to enter the sub-fifteen metre region at a shallow enough angle, they will be trapped. Appendix B shows simulations (created with the NEMESiS model described in chapter 5) of how radar coverage for an antenna operating at E/F band (3 GHz) is altered by different height evaporation ducts and shows the onset of trapping.
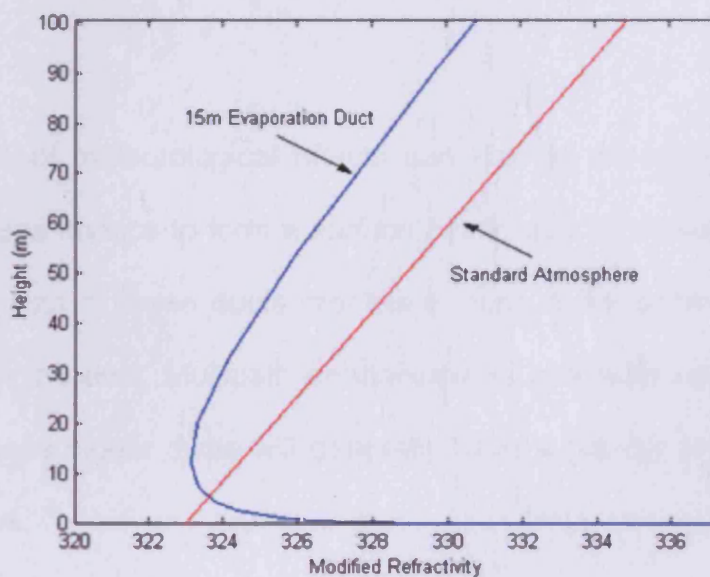
Figure 2-7 M-profiles of an evaporation duct and standard atmosphere

Evaporation duct heights vary with geographical region and season, but they are present most of the time over the sea, even in cool climates. For example, the yearly mean height in the North Sea is around five metres, whereas in the

Persian Gulf it is nearer 20 metres. The world average duct height is thirteen metres [METOC, 1994].

Large evaporation ducts of heights up to 200 metres, called *advection ducts*, may also be found in coastal regions and enclosed seas adjoining hot land masses (examples include the Mediterranean and Persian Gulf). They form when hot, dry continental air mixes with cooler moist air over the sea, leading to a strong localised duct when looking towards the coastline. There is a large diurnal and seasonal variation in this type of duct as the largest land/sea temperature contrasts will occur on summer evenings. Other meteorological processes such as subsidence and night time cooling can cause similar ducting effects.

Combinations of meteorological effects can lead to an advection duct being lifted off the sea surface to form a *surface based duct* at altitudes of up to 1000 metres. The size of these ducts creates a much more complicated coverage pattern within the duct. Multipath enhancements and nulls can become highly localised. These higher ducts will generally have a greater impact on airborne radar systems.

2.5 Refractivity in real scenarios

The effects of local climatology lead to a very complicated refractivity structure which varies in range and altitude. The influence of terrain on climate and propagation is another range dependent feature. To further complicate matters, scattering from aerosols, rough or absorbing surfaces, and turbulent

atmospheres will all affect the propagation. A difficult balance must usually be struck between a model and scenario that captures the important characteristics of the performance of a radar system, whilst highlighting the limitations and simplifications within the scenario.

2.6 Noise and noise modelling

Thermal noise is a background signal in a radar detector that limits the minimum detectable signal. It is inherent in all electronic systems due to thermal motions of current in components and is 'white' as it has a constant power at all frequencies. The mean noise power is related to Boltzmann's constant, k_B, the temperature of the components (usually set to standard temperature, T_0 = 290K) the bandwidth of the system, B, and the quality of their construction (usually rolled up into measure called noise factor, NF). The mean noise power in a receiver system is often described by equation 2.4, although there are many different formulae in radar text books to model various parts of the radar system that contribute to the total system noise.

$$P_n = k_B \cdot T_0 \cdot B \cdot NF$$ *Equation 2.4*

Noise is a simple random process and so the noise voltage probability density function (PDF) is Gaussian. As military radar systems tend to have two channels (I & Q[6]) the absolute voltage, x, is usually more important for radar analysis and has a Rayleigh PDF:

$$P(x) = x \cdot e^{\frac{-x^2}{P_n}}$$ *Equation 2.5*

---

[6] In-phase and Quadrature – defined in section 2.8.1

Detection is often carried out in power, X, rather than voltage (power is proportional to the square of the voltage). The power PDF is negative exponential:

$$P(X)=\frac{1}{P_n}e^{\frac{-X}{P_n}}$$

Equation 2.6

The voltage and power PDFs for noise are compared in Figure 2-8. The noise PDF distribution can be integrated to look at the probability of exceeding a given level X_0:

$$P(X>X_0)=\int_{X_0}^{\infty}\frac{1}{P_n}e^{\frac{-X}{P_n}}=e^{\frac{-X_0}{P_n}}$$

Equation 2.7

which is crucial for defining a threshold for limiting the likelihood of false alarms in the detector (as discussed in 2.8.2).
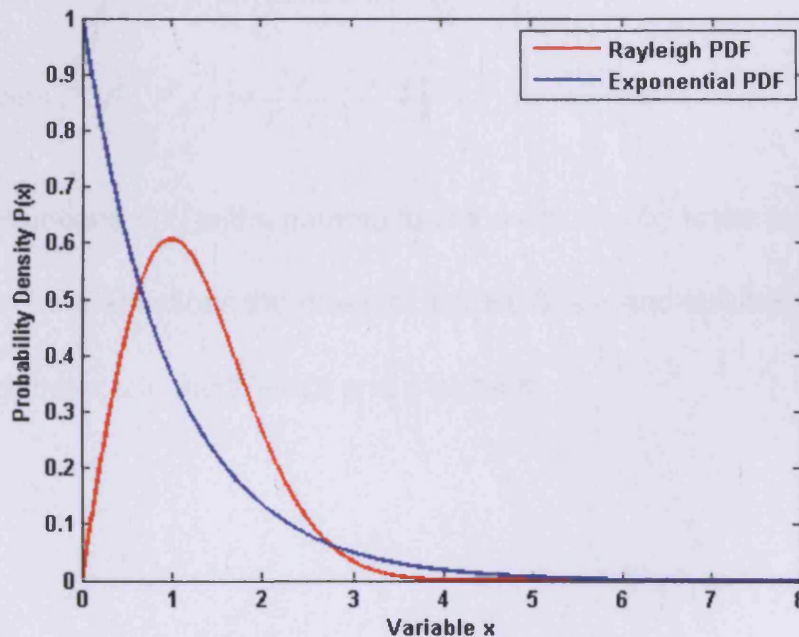
Figure 2-8 Absolute voltage and power PDFs for thermal noise

2.7 Clutter and clutter modelling

The effects of clutter are critical to examining radar performance. The strength and statistical variation of clutter returns, in comparison to those from targets, limits the performance and robustness of any radar system. The elevated levels associated with anaprop make clutter modelling even more important.

Clutter returns are usually parametrised by analysing real radar data to fit a probability distribution model characterised by mean RCS and spikiness. Spikiness represents how the clutter differs from the noise-like signals inherent in all radar receivers. Noise can be described by a simple exponential PDF but clutter data usually fits to more skewed distributions such as the Weibull or K distributions [Sayama & Sekine, 2000 and Ward et al, 2006]:

Weibull PDF $\quad P_W(X) = \dfrac{1}{\alpha} \cdot \left[\dfrac{\Gamma(1+\alpha)}{\sigma} \right]^{\frac{1}{\alpha}} \cdot X^{\frac{1}{\alpha}-1} \cdot e^{-\left[\frac{\Gamma(1+\alpha)}{\sigma} \cdot X \right]^{\frac{1}{\alpha}}}$ $\qquad$ *Equation 2.8*

K-distribution PDF $\quad P_K(x) = \dfrac{2\sigma}{\Gamma(v)} \cdot \left(\dfrac{\sigma \cdot x}{2} \right)^{v} \cdot K_{v-1}(\sigma \cdot x)$ $\qquad$ *Equation 2.9*

In these equations $\Gamma(x)$ is the gamma function and $K_{v-1}(x)$ is the modified Bessel function. In both equations the mean clutter RCS is σ and spikiness is controlled by the parameter α in the Weibull and v in the K.
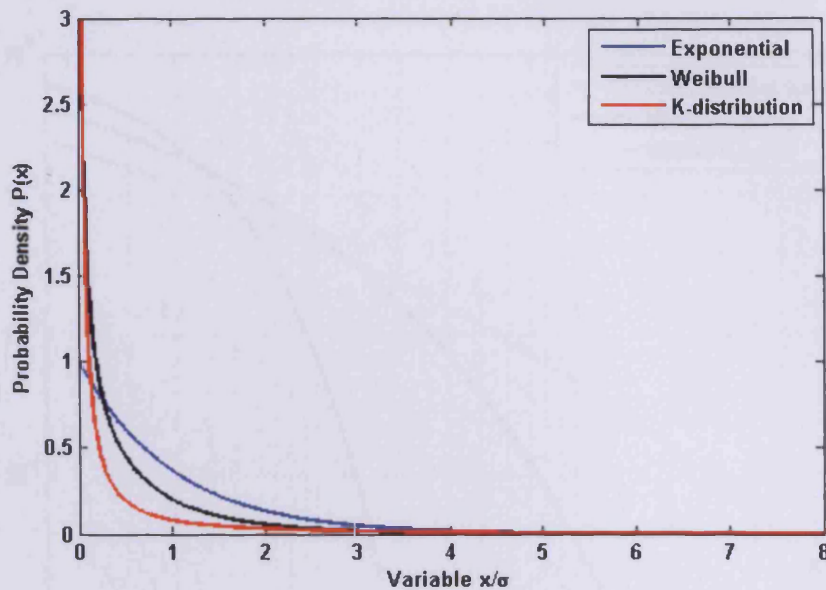
Figure 2-9 Comparison of different clutter PDFs which all have the same mean value

These two sea clutter PDFs (shown with the noise PDF in Figure 2-9) are quite similar and importantly they have much longer tails than noise (as can be seen in the log scale plots in Figure 2-10 and the simulation plots in Figure 2-11) and so have much higher false alarm rates at larger clutter amplitudes. For realistic radar clutter the Weibull distribution parameter α can range between one (which is a non-spiky noise-like PDF equivalent to $\nu \rightarrow \infty$ for the K-distribution) to four (very spiky, usually only applicable to land clutter, equivalent to $\nu \simeq 0.156$ for the K-distribution). To overcome this, radar systems must usually raise detection thresholds in cluttered regions to keep the false alarm rate down at the expense of small target sensitivity.
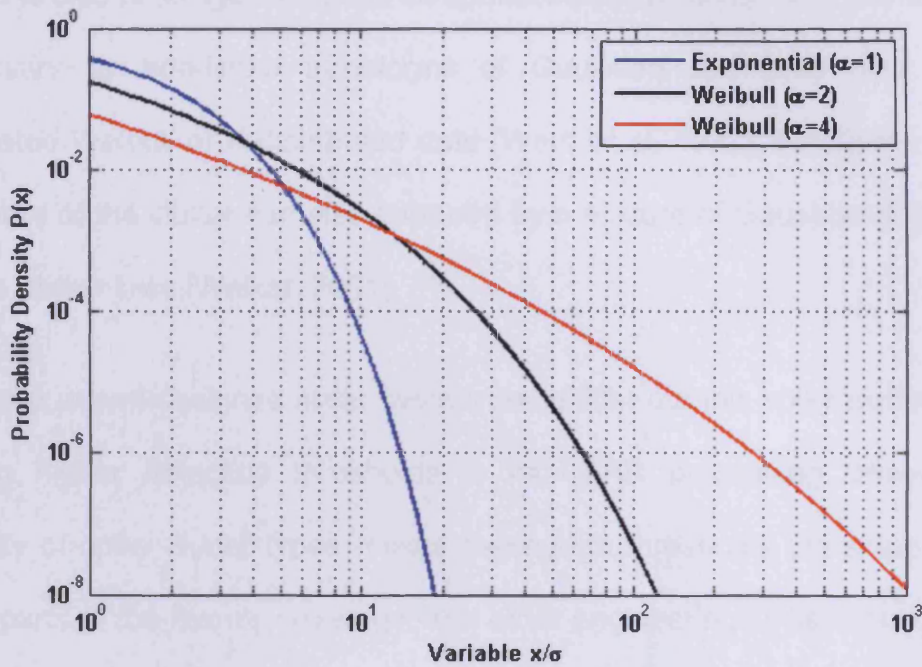
Figure 2-10 Comparison of Weibull PDFs with the same mean and varying
α showing the long tails found in real clutter data
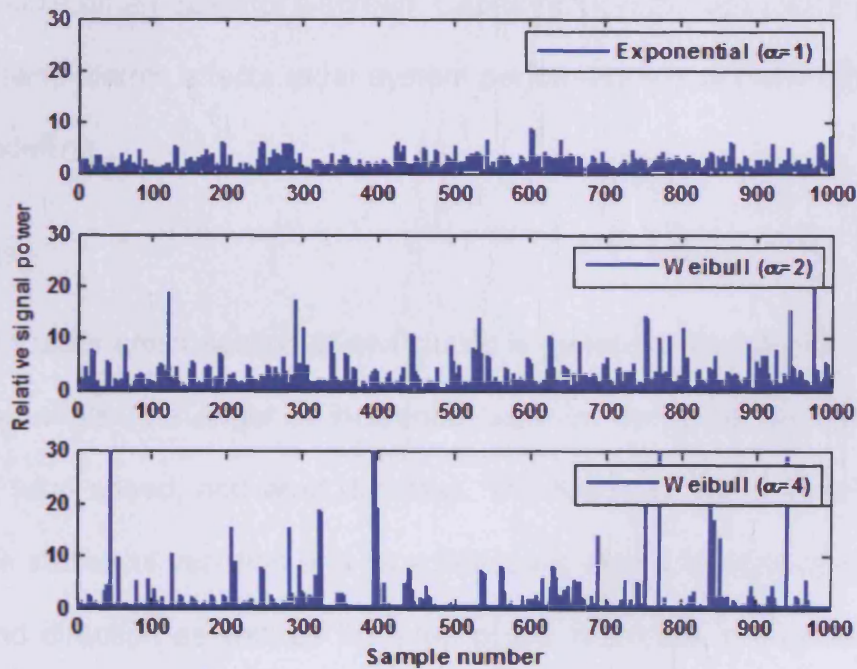
Figure 2-11 Simulation of radar clutter returns simulated from the PDFs

shown in Figure 2-10

Clutter is also heterogeneous and so spatial correlations can also be modelled if necessary by non-linear transforms of Gaussian correlated data to give correlated Weibull or K-distributed data [Ward et al, 1997]. Finally the Doppler signature of the clutter can also captured by a mixture of Gaussian shapes and simple power laws [Walker, 2001].

In theory, a well designed radar system could filter out this spiky clutter fully by setting higher detection thresholds in its CFAR processing. However the scarcity of spiky clutter types makes these high thresholds unnecessary over large parts of the radar's coverage, and other engineering limitations mean that this clutter will tend to break through. Therefore in real world systems, spiky correlated clutter creates site specific target-like returns which will create false alarms visible on an operator's screen. Capturing how the operator's perception of these false alarms affects radar system performance is another challenge for radar modelling.

2.7.1 Sea clutter

The mean radar cross section of sea clutter is generally modelled as a function of grazing angle (the angle of incidence between the radar antenna and the surface), wind speed, and wind direction. The K-distribution is usually used to model the statistical variation and its spikiness is also a function of angle, wind speed and direction as well as the area of the radar cell in question (smaller radar cells tend to be spikier in nature, larger ones average out the spikes). Correlation lengths and Doppler shape are also dependent on the wind speed

and can be derived from theoretical sea surface spectra such as the Pierson-Moskowitz spectrum [Pierson, 1976]. Figure 2-12 shows a comparison between real sea surface RCS measurements and simulated data created from a Pierson-Moskowitz wave spectrum. The wave height field created from the spectrum has been modified to give data fitting to a Weibull distribution to create an approximate model of the spatial variation of sea clutter radar data.
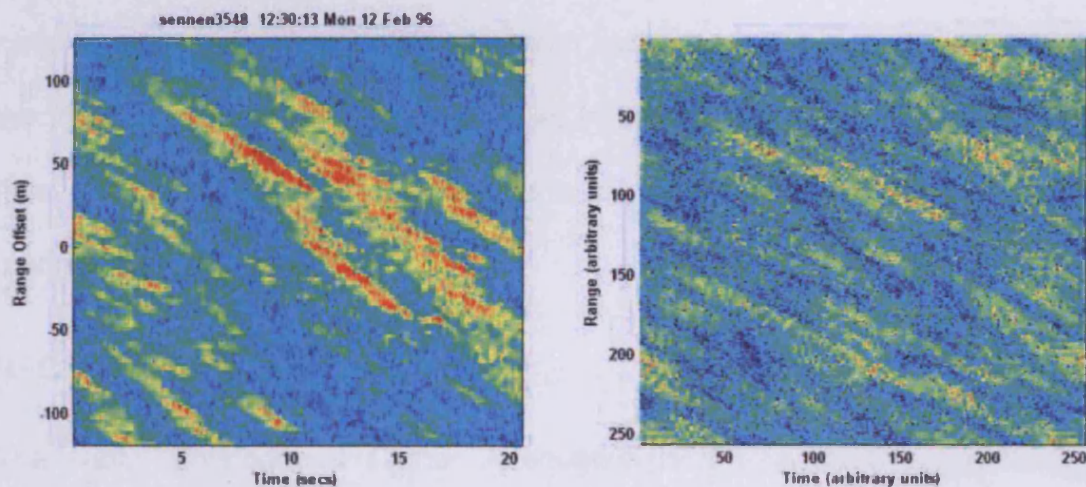
Figure 2-12 Comparison of real (left plot) and simulated radar data (right) of the

sea surface

Another phenomena that can be modelled are sea spikes. These events are caused by breaking waves and can create a relatively long lasting region of higher returns and can lead to false alarms [Walker, 2001].

2.7.2 Land clutter

Land clutter RCS is modelled as a function of clutter type (various types are usually defined). Land clutter variation is generally modelled by a Weibull distribution and is spikier than sea clutter [Billingsley, 2002]. Land clutter spikes

(spatially correlated long lasting regions of clutter) are of course more long lived than sea clutter and so the position of a land clutter spike must be retained when simulating consecutive scans of a rotating radar [Moon & Moon, 1996].

2.7.3 Clutter description standards

A clutter description defines a coherent set of these simple clutter models for a range of clutter types. Standardised clutter definitions can be used in different radar models to define the clutter strength and statistical variation to ensure that the final model outputs are comparable. In the UK defence industry, NECAPS (see section 2.7.4) is often used as a common basis for shipborne radar modelling.

2.7.4 NECAPS

The Naval Environment Clutter Attenuation and Propagation Specification, NECAPS [Branson, 2006], is a set of algorithms defining the environmental effects on naval sensors. The specification is suitable for current high level modelling and procurement requirements. The algorithms in the specification have been based on experimental data and a distillation of theoretical modelling techniques.

NECAPS defines algorithms for representing sea, land, bird, insect, rain, and chaff clutter. Both the clutter statistics and spectral characteristics are defined. Attenuation coefficients for the atmosphere, rain, and clouds are also presented. The effects of multipath are defined, and anaprop effects are also discussed. With care and experience the simple algorithms can be expanded

for use within propagation and baseband models as well as the radar equation models they were designed for.

NECAPS is also used for defining land clutter, although the model produced by Lincoln Labs [Billingsley, 2002], which is based on 40 years experimental data gathering and analysis, has also been implemented for certain studies.

2.8 Radar signal processing

Radar systems employ various real-time signal processing techniques to analyse the data being gathered. The aim of these techniques is to increase the contrast between targets, system noise, and unwanted backscatter from clutter. At the design stage there are a series of decisions made that trade-off detection performance against the costs of high speed processing and the time budget available to the radar to employ the waveforms that support advanced processing. A few of the most important waveforms and algorithms are covered in the following sections. Note that some important subsystems and algorithms commonly found in radar processing systems have been omitted for clarity.

2.8.1 Normal radar

Normal radar (NR) waveforms are the simplest form of radar transmission. A pulse is generated, mixed with the radar carrier frequency, before being transmitted out through the antenna. Next the receiver is switched on and the backscatter is gathered via the antenna until the receiver is switched off before the next pulse is transmitted. The time between pulses is called the pulse repetition interval (PRI) and the frequency of these pulses is the pulse repetition

frequency (PRF). The PRI and the velocity of light (c), usually defines the maximum range (R_{max}) that the radar is capable of detecting targets.

$$R_{max} = \frac{c \cdot PRI}{2}$$ *Equation 2.10*

The factor of two in the equation above is due to the radar pulse having to travel to the target and back within the PRI. The minimum detectable range, without using special processing, is half the length of the transmit pulse because you cannot receive whilst transmitting and the maximum range is reduced by the same amount.

In a coherent radar the received signal is mixed down from the carrier frequency by a superheterodyne process that produces two orthogonal channels of data. These two channels, termed in-phase and quadrature or I & Q, are filtered down to reduce their bandwidth and minimise interference. The signals are sampled at a constant rate and processed so the range to targets can finally be measured by looking for peaks in the sampled data.

2.8.2 Detection

After the NR signal data is sampled, the samples are squared to create a data stream which for historical reasons is termed radar video (probably because early radar systems sent this stream directly to a cathode ray tube, CRT, screen with no further processing). The samples are squared which converts from voltage to power and creates an approximately optimum detector of targets in a noise background [Marcum 1960]. This video is then compared to a threshold value and a detection is declared if any sample exceeds the threshold as shown

in Figure 2-13. The size of the threshold is chosen to reduce the number of false alarms to a low enough constant false alarm rate (CFAR) that won't overload downstream subsystems such as the radar tracker. If a signal is to be detected against a background of thermal noise then Equation 2.7 can be inverted to calculate the threshold ratio, T_0, needed to give a given CFAR:

$$P(X > X_0) = CFAR$$

$$\frac{X_0}{P_n} = T_0 = -\log_e(CFAR) \qquad\qquad \textit{Equation 2.11}$$

So for a CFAR of one false alarm in a million (10^{-6}) the threshold will be 13.8 times larger than the mean noise. In clutter the CFAR threshold must be set much higher to exclude false alarms. For Weibull clutter (see section 2.7) the threshold needed is:

$$T_0 = \frac{\{-\log_e(CFAR)\}^\alpha}{\Gamma(1+\alpha)} \qquad\qquad \textit{Equation 2.12}$$

Now the CFAR threshold can be as high as 1000 (or 30 dB) to maintain low false alarm rate of 10^{-6} in very spiky clutter. As the usable dynamic range of older radar systems won't be much greater than 30 dB, clutter becomes a significant problem. (Note that the calculation of the CFAR threshold for a realistic returns signal, which is a mix of clutter and system noise, is a difficult problem that cannot be solved analytically in general. This creates a problem for system modelling which can be solved by the numerical methods such as those described in section 5.5.2.)
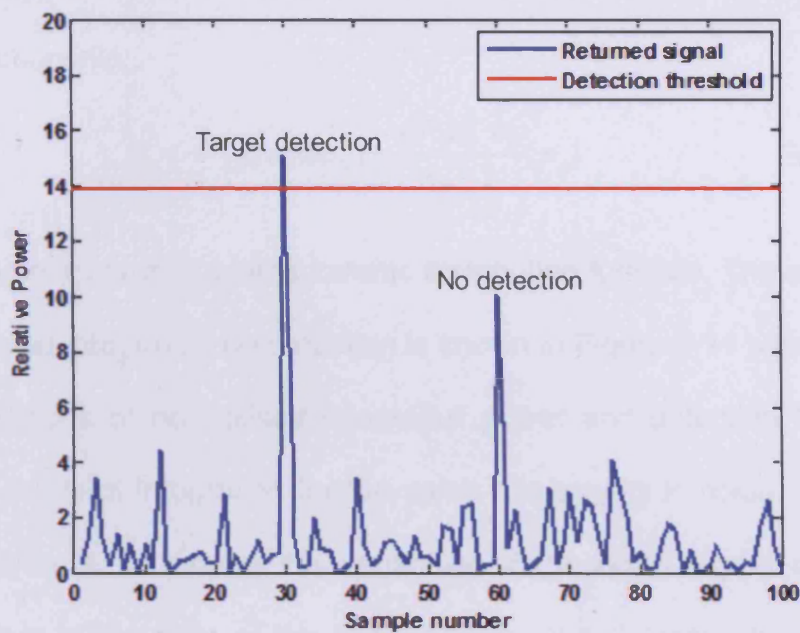
Figure 2-13 Detection of a target in a background of thermal noise

Threshold crossing events are termed detections or plots and the range and azimuth of each plot is then passed by the detector into the tracker as a real-time plot stream.

2.8.3 Non-coherent integration

In a rotating antenna radar system the rotation rate is likely to be such that several pulses will be transmitted during the time it takes for the beam pattern to scan over a target. This allows several pulses, n_p, to be incoherently summed together. Although this process doesn't improve the mean signal to noise ratio (SNR) in the radar receiver, it reduces the variability of the noise allowing a lower detection threshold T_0 to be set for a given *CFAR* and so improves detection performance (this is often considered to be equivalent to an improvement in SNR). The normalised threshold to noise ratio can be

calculated by successive convolutions of the exponential PDF to give the general relationship:

$$T_0 = \frac{1}{n_p} qgamma \left(1 - \frac{CFAR \cdot n_p}{n_p - 1}, n_p \right)$$

Equation 2.13

Where *qgamma()* is the gamma inverse distribution function. The effect of non-coherent pulse integration on detection is shown in Figure 2-14 which compares three simulations of normalised integrated power and detection threshold for increasing levels of integration for the same two targets in noise. The effect of the integration is to reduce the variability of the noisy signal regions. The smaller target to the right of the plots is below the detection threshold in the single pulse case (top plot) due to the high threshold required to give a suitable false alarm rate. It is easily detected after non-coherent integration as simulated in the lower two plots which need a lower threshold to achieve the same false alarm rate.
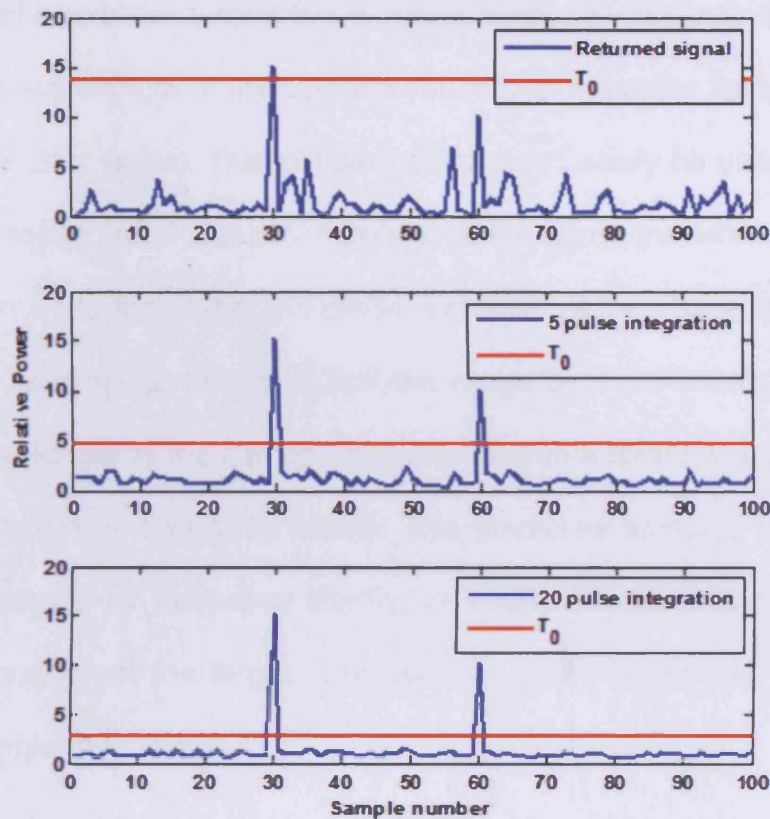
Figure 2-14 Detection improved by pulse integration

Changing the carrier frequency between pulses (termed frequency agility or frequency hopping) can decorrelate the clutter backscatter between pulses allowing non-coherent integration to also help with clutter processing.

2.8.4 Coherent integration and detection (MTI, MTD and Doppler)

When a coherent radar pulse is transmitted it has a known amplitude and phase. The phase is fixed by the phase of the local oscillator at the time of transmission but the phase of the local oscillator continues to rotate with time. A phase sensitive radar receiver compares the phase of the received backscatter with that of the local oscillator to produce an IQ signal. Sampling produces a phase angle for each range gate. The phase will be proportional to the range of

the target and is extremely sensitive to range because the phase will completely rotate in one wavelength of the carrier frequency of the radar system (i.e. every 10cm for a 3 GHz radar). This phase rotation can't easily be used to measure the range directly, but if a burst of pulses of the same transmit frequency are sent out then a moving object will cause a rotation of the phase of the returned signal for a fixed range bin (note that the range bins are usually much larger than the wavelength of the carrier frequency and so a target is unlikely to move between range bins during the burst). This discretely sampled phase rotation can be processed by frequency filtering or Fourier series analysis to give the Doppler frequency of the target. The velocity of the target can be calculated from the Doppler frequency.

Coherent radar receivers allow pulses to be coherently integrated. The noise in the receiver is spread across the Doppler frequency space whereas the target signal sums at one frequency. Doppler processing can therefore give an SNR improvement proportional to the number of pulses in the burst.

Another advantage of coherent integration is that since most environmental clutter is stationary or slow moving it won't cause such a significant phase rotation and so moving targets can be separated from stationary clutter by using appropriate filters. The simplest way to do this is to apply a high pass filter to the response from a small number of pulses (n_p is usually 3 or 4). This process is called a moving target indicator or MTI. A strong response from MTI implies a moving target is in the range bin being tested.

If velocity needs to be measured then more pulses are usually used (n_p is perhaps 8 or 16 pulses) and fast Fourier transform (FFT) Doppler processing (using filter windows) is employed allow the pulsed returns to be processed into a series of equally spaced velocity bins. The velocity of a target can be measured by discounting any slow bins containing clutter and then picking the velocity bin with the highest signal strength. Better clutter cancellation can be achieved by using tailor made filter banks called moving target detector banks or MTDs instead of the simple FFT.

Doppler waveforms tend to use quite high PRFs to detect fast moving targets. This limits their maximum range of detection.

In summary the main advantages of Doppler processing are that it detects moving objects (which usually implies that they are man made), cancels clutter (which increases the signal to noise plus clutter ratio or SNCR), and increases SNR. The disadvantages are that Doppler bursts require significant radar time and can have limited range.

2.8.5 Ambiguous range problems

Naval radar systems usually operate range unambiguously which means that clutter is expected to be found inside their maximum range (R_{max} see equation 2.10) of a clutter cancelling waveform. If there is a strongly reflective clutter region beyond this maximum range then the clutter returns caused by the first pulse reflecting from this region will be be picked up in the second pulse's receive period and then in all subsequent pulses. As there were no returns from

this clutter during the first pulse receive, the clutter in the second pulse will be assumed to lie inside the maximum range and so is folded in from its true position. So on an operators screen these returns will appear to be closer to the radar than they should because their true range is ambiguous to the radar system. This will increase clutter levels generally at close range and may lead to a reduction in radar performance. This effect can happen if the the clutter region is at any range between R_{max} and $n_p.R_{max}$ and the clutter will first appear in the pulse receive period corresponding to the range of the clutter. (Note that other types of radar systems such as tracking radar and airborne radar often intentionally use high PRF range ambiguous waveforms and resolve the true range of objects by further processing of waveforms with different PRFs.)

Ambiguous range clutter is a particularly important problem for coherent radar processing. Usually a small fast moving target that is swamped by slow moving clutter can be extracted in a coherent radar using Doppler or MTI processing. However, if a target is in a region free of clutter within the maximum range is masked by ambiguous folded clutter then a step like amplitude increase will appear somewhere in the series of returns for the target range bin. This is because the target will not be masked until the clutter reflections outside the unambiguous range reach the receiver. This sudden step in amplitude raises the clutter bandwidth and reduces clutter cancellation and target detectability. Mathematically this can be shown by looking at the Fourier transform of the Heaviside function, $H(X)$, where H is 0 for $X<0$, 0.5 for $X=0$ and 1 for $X>0$. If the

clutter were unambiguous and appeared in every pulse then its Fourier transform ($\mathscr{F}\{u\}$) is a delta function at zero velocity.

Unambiguous range $\qquad \mathscr{F}\{y=1\}=\delta(x)$ $\qquad\qquad$ Equation 2.14

In ambiguous clutter the Fourier transform gives:

Ambiguous range $\qquad \mathscr{F}(H(x))=\delta(x)+i\pi$ $\qquad\qquad$ Equation 2.15

This means that the velocity response is now against a background of magnitude π rather than zero. In a real radar system the discrete version of this analysis is carried out with an FFT but the background to the velocity response will still be increased which reduces the target SNR and therefore reduces detection sensitivity and may also increase the false alarm rate.

One way to mitigate this performance loss is to discard the pulses before the amplitude step, which are then called guard pulses. The remaining pulses containing the target and the ambiguous clutter can then be processed correctly. This solution means that more pulses have to be transmitted to maintain the processing gain. In anaprop conditions, many guard pulses may be necessary to prevent loss of performance. This will take up further radar time and so may reduce target detection range.

2.8.6 CFAR processing

The output from NR or Doppler processing produces a video stream. As described in section 2.8.2, to carry out detection in a particular test range cell a local CFAR threshold must be set that reduces false alarms due to noise and

background clutter to an acceptably low level. Many radar systems use a cell averaging CFAR (CA-CFAR) to estimate this threshold. A simple averaging filter is applied to the range cells up-range and down-range of the test cell to calculate the mean background noise plus clutter level. A pre-calculated threshold is then multiplied on to this and compared with the test cell to look for a detection. This detection will create a 'plot', a detection associated with a range and azimuth (and possibly other information such as strength and Doppler), which is passed out of the signal processor and onto a display screen or into an automated tracker.

One problem with the CA-CFAR is that the fixed threshold approach cannot account for changes in clutter properties. This can lead to large numbers of false detections in spiky clutter that limit the effectiveness of the system. Other CFAR algorithms can be used that attempt to solve this problem but they are more complex and need to use many more radar samples which leads to reduced performance at boundaries between different types of clutter.

2.8.7 Pulse compression

A simplistic view of how a radar works suggests that the range resolution of a radar is limited by the pulse length transmitted. More fundamentally though, the resolution is limited by the bandwidth contained within the transmitted pulse. Pulse compression aims to increase the bandwidth of the transmitted pulse to allow greater resolution from a longer transmit pulse. The longer transmit pulse means that more energy reaches a target and so a well designed pulse

compressor increases SNR which ultimately increases probability of detection. However SCR will not always be increased (e.g. if the clutter and target are in the same compressed range cell) but detection in clutter may be improved because clutter peaks will often become separated from targets due to the higher compressed resolution. The higher resolution also allows better target positioning and more accurate tracking.

The disadvantages of pulse compression include increased system complexity and a loss of performance close to the radar. This is because the longer pulses mean that there is a long dead time during the pulse transmission in which no returns can be received and so close-in radar detection will be lost.

2.8.8 Signal processing chains

Most radar systems interleave different waveforms to attempt to give the best of all worlds. Short range detection is usually handled by Doppler processed, short pulse, high PRF waveforms. Longer range detection can use simpler normal radar processing with longer pulses which employ greater pulse compression.

2.8.9 Tracking

All the detections from the signal processing chains are fed into a tracker. A tracker maintains a map of detections over several scans of the radar system and uses probabilistic algorithms to look for target-like motion. Once a target is spotted and declared the tracker can highlight it to the radar operator for further assessment.

2.9 Radar Modelling

Radar systems are very complex and often critical to the safety of life and so are expensive to develop and to procure. A system that doesn't have the necessary performance could be a life threatening procurement error that would be expensive to put right. Accurate radar modelling is an essential part of the reducing the risk of such a mistake as well as defining what performance is needed to fulfil a particular role.

The aim of any radar model is to try to capture and describe the performance envelope of a radar system. In basic terms, this involves calculating the signal reflected from a target of interest in order to judge whether it is far enough in excess of the other signals present in the radar so that the target should be detected. Turning this relatively simple calculation into a useful description of real world performance remains a challenge for radar research. The next few sections of this chapter outline the different types of model used in the radar industry today to try and meet this challenge.

A radar performance model is made up of a number of smaller models. Simulations of the radar transmitter, the propagation of energy through the atmosphere, the reflection of energy from targets and clutter, and a model of the radar receiver all must be linked together. The results must then be fed through a simulation of the signal processing and tracking radar functions to finally produce an estimate of radar system performance.

2.9.1 Simple radar models

Simple radar models based on the radar equation can be very effective at comparing the relative performance of radar systems in standard atmospheric conditions and can be rapidly built using a spreadsheet application. However, it is difficult to incorporate the effects of clutter and the environment.

2.9.2 Probabilistic models

Probabilistic models are used for high quality comparative modelling of current and future radar systems. The fluctuating returns from noise, targets, and clutter are modelled statistically with a given mean power and statistical variation. Two path ray models are used to model the effects of multipath and diffraction on target strength in standard atmospheres. The underlying principles of such models can be found in radar textbooks [Skolnik, 1986, Blake, 1980]. This type of statistical model can capture the performance envelope of a system but can run faster than real-time. Therefore detailed modelling of well understood radar systems can be achieved using appropriate statistical representations of real system complexity. Various modelling wrappers can be added to provide models of complex radar systems such as multifunction radar (MFR) scheduler and tracking functions and so can provide information on how these more complicated closed loop systems will operate in difficult conditions. An example of the output of this type of radar model is shown in Figure 2-15 which plots SNR for a target (in dBs), the threshold modelled (in dBs) and the consequent probability of detection.
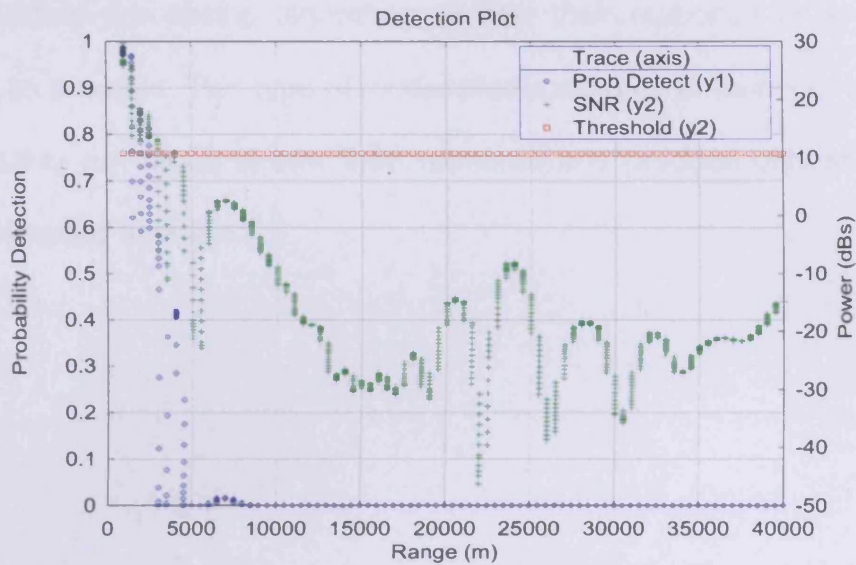
Figure 2-15 Radar model output showing various radar performance metrics

2.9.3 Radar propagation models

Radar propagation models look at how RF energy is affected as it propagates through the lower layers of the atmosphere. They are usually approximate numerical solutions to the fundamental equations underpinning the physics of radar and are therefore more realistic than the radar equation methods that are the basis of most system models. With careful processing of the predicted propagation fields, these models can also model the effects of the environment on clutter and target returns, which are critical factors for evaluating radar performance. Chapters 3 & 5 contain much more detail concerning radar propagation models and their applications.

2.9.4 Baseband models

Baseband models simulate the returns from targets and clutter including the effects of thermal noise and phase noise. These returns can then be run

through signal processing algorithms to test their response in as realistic a situation as possible. This type of model produces large amounts of data and so will generally run much slower than real-time and produce only small sets of data for detailed analysis.

3 Literature Review

This chapter examines the research carried out into radar propagation effects through modelling and data recording trials. The models used and their applicability to radar system modelling in complex scenarios are considered.

The effect of anaprop on radar and radio performance has been recognised for many years as a significant problem in certain theatres and situations. Slade [Slade, 1996] describes the USS Sterett's radar picture as being 'extremely confused' due to anaprop in the Battle of Dong Hoi during the Vietnam war. Anaprop conditions in the Persian Gulf also provide a significant challenge to maintaining radar performance due to large increases in sea clutter [Devereux & Van Egmond, 1989].

Anaprop is also understood to have an impact on Royal Navy sensors and communications and every RN ship carries a guidance memo concerning its effects [METOC, 1994].

The benefits of improved modelling of these effects have often been overlooked due to the complexity of the problem and the difficulty in drawing general conclusions from site specific propagation modelling.

3.1 Propagation model history and development

As radar models have developed, the problem of modelling the propagation from the antenna out to the backscatter environment and back again has

proved to be a difficult one. The propagation model started with freespace modelling, then the interference pattern was added by considering flat earth reflection paths (multipath) and then curved earth reflections. This multipath model was then bolted onto a diffraction model to cover over the horizon effects. This diffraction model could also used to model terrain as a series of knife edge diffractions (such as SEKE [Ayasli, 1986]).

Over the years many attempts have been made to add the effects of anaprop into propagation models. The first efforts to include anaprop merely modified the curvature of the earth to extend the radar horizon further and further. This showed some of the effects of increased target detection ranges, and may have approximated to the effect of a low evaporation duct, but this was not an accurate model of most real world scenarios.

As computers became more powerful new types of modelling became possible that used much more accurate approximations to the solutions of Maxwell's equations. One problem is the size of the modelling domain. Many methods of electromagnetic modelling can analyse small regions but radar requires large regions, millions of wavelength in range, to be modelled.

3.1.1 Geometric optics model

This simple approach is often still used in legacy or high level models. It divides the modelling domain into two regions in which simple approximate solutions to Maxwell's equations above a spherical earth can be applied. The two regions are the interference zone, which is usually at shorter ranges above the horizon,

and the diffraction zone [Pryce, 1953], which is the long range field over the earth's horizon. The interference zone multipath field is calculated by evaluating the two straight-line paths (direct and reflected) from the radar to any point in space. An enlarged earth's radius (usually 4/3 of the real earth's radius) is used to account for standard atmospheric refraction [Domb & Pryce, 1947]. The space between the two regions is modelled by fairly arbitrary interpolation approaches which splice together interference calculations evaluated near to the horizon with diffraction results from well over it. The approach has the advantage of producing an answer without pre-calculating the solution on a grid beforehand. This ensures computation times during radar simulations are short, but variable refractive index, ducting effects and propagation over terrain are impossible to model accurately.

3.1.2 Ray tracing

Ray tracing treats the antenna as a source of rays, lines running perpendicular to the wavefronts, propagating out from the antenna [Patterson et al, 1987]. The surface reflections and bending of the rays can be modelled using geometric optics and Snell's law. The number of rays used affects the speed and accuracy of the result but refractive index variation can be modelled until, in stronger ducting conditions, multiple rays overlap one another in regions called caustics where the approximations of this approach break down. Propagation into diffraction zones such as over the horizon or behind terrain is difficult to model as different equations must be applied and the number of calculation regions builds up rapidly. Despite these limitations, ray tracing can provide an excellent

quick look at radio wave propagation and efficient codes are available thanks to the need to generate realistic visual computer graphics for games and other media.

3.1.3 Waveguide models

Waveguide modelling uses waveguide mode theory [Yeoh, 1990] to provide a one way propagation field solution. The solutions produced are slow but very accurate for range independent rough sea surface scenarios. This type of model is often used as the baseline solution for testing of less accurate but faster and more flexible methods [Wu, 1993].

3.1.4 Parabolic equation

Maxwell's equations were simplified into the parabolic equation (PE) during work by Fock [Leontovich & Fock, 1946] which allowed a few simple refractivity cases to be analysed. The advent of computers lead to the development of numerical solutions to PEs based on a number of methods.

The PE is a one way propagation model and so backscatter processes must be modelled by approximate methods. The PE is also used in optics (where it is called the beam propagation method) and in acoustics (for the modelling of sonar propagation). The most direct solution is to use Finite Difference Time-Domain or Finite Element [Levy, 2000] approaches which allow the propagation field on a given calculation grid to iteratively approach the correct solution. These methods produce accurate results but involve long calculation times.

In 1973 an efficient method of solving the parabolic equation was developed that used a linear stepping method which iteratively steps the solution out from the antenna using FFTs [Hardin and Tappert, 1973]. The simplicity and speed of the FFT allows results to be calculated much more rapidly than other methods and various boundary conditions can be applied to simulate the effects of terrain. The split-step method is limited to modelling propagation within a few degrees of the horizontal but this region covers most of the phenomena associated with the benign refractive index changes found in the atmosphere. The history and use of the parabolic equation is described by Levy [Levy, 2000].

3.1.5 Integral solutions

Integral methods [Tough et al, 2004] aim to provide exact solutions to certain propagation problems such as the interaction of radio waves with a small region of realistically shaped sea surface. They have the advantage of modelling the full two way Helmoltz equation and so can accurately model backscatter from complex surfaces. Although this approach will model the propagation field very accurately its complexity and glacial speed makes it more appropriate for understanding of low level phenomenology such as wave scattering mechanisms rather than the simulation of whole radar systems.

3.2 Propagation models

Table 3.1 below shows a list of microwave propagation models commonly used in radar research.

Model Type	Name(s)	Description	Issues
Simple multipath and diffraction	RE3, NaRCoSiS	UK naval radar MOD procurement computer model developed in 1995 and still used	No anaprop, no terrain
Knife edge terrain diffraction	SEKE	1989 US research computer model of propagation over terrain	No anaprop
Waveguide model	MLAYER	Accurate model of propagation over the sea	Slow, range independent, no terrain, no clutter modelling
Ray trace model	IREPS, EREPS	US Navy operational integrated refractive effects predictions (IREPS, early 1980s) and its engineering/research counterpart (EREPS developed in 1989)	Inaccurate anaprop modelling in complex conditions, no clutter modelling
Split-step PEM and ray trace	AREPS (APM, RPO)	US PEM operational and research model created by SPAWAR in San Diego. PEM is used for low angles and ray tracing for high angles. Available for download	Clutter strength algorithms, difficult to modify for research purposes
Split-step PEM	TEMPER	US PEM model used in USN Aegis SPY-1 radar system research. Development of this model has driven PEM techniques forward significantly.	Clutter strength algorithms, difficult to obtain for research purposes
Ray trace model	PIRAM	French model expanded from an atmospheric model into a propagation prediction using ray tracing	Inaccurate anaprop modelling in complex conditions, no clutter modelling
Split-step PEM	TERPEM (HPPEM, PCPEM)	UK PEM model developed by Rutherford Appleton Labs from 1988 and marketed commercially by Signal Science	Clutter strength algorithms, radar system model

Model Type	Name(s)	Description	Issues
Split-step PEM	NEMESiS	UK PEM model written in Matlab for UK RN procurement assessment and research	High angle coverage not modelled
Finite difference PEM	FDPEM	UK model developed by Rutherford Appleton Labs	Slow, not well used

Table 3.1 Comparison of common radar propagation models

3.3 Choice of model for this thesis

The modelling approaches covered in the sections above and the existing propagation models listed in Table 3.1 are all useful when examining specific aspects of radio propagation. To model a radar system in realistic environments that include terrain and range varying refractivity, it was decided that the split-step parabolic method gave the best combination of qualities necessary for rapid system modelling over large scenarios.

3.4 UK propagation modelling

Historically, the advances made in propagation modelling have not been pulled through into the UK defence research and procurement process. There are many reasons for this including:

- Inertia – existing probabilistic models are better understood

- Model speed – propagation models are slower than traditional methods

- Lack of coordinated funding across different projects

- Validation – very difficult to prove that the results are accurate

- 'So what' factor – even when you've modelled propagation effects, it's still a difficult problem to solve

In 1989 Rutherford Appleton Labs was funded by the MOD to develop PCPEM [Craig & Levy, 1991], the UK's first dedicated propagation model, but its use in UK defence procurement seems to have been limited by licensing restrictions when the model was sold commercially by Signal Science. In 1994, the Defence Research Agency (DRA) developed PEMAWI to research upgrades to its probabilistic modelling using parallel processing architectures to improve run times [Branson, 1996]. In 1996 the increased speed of PCs led to this model being recoded and upgraded in Matlab by the author as NEMESiS (described in Section 5) to research improved clutter modelling. In parallel, the Maritime Warfare Centre (MWC) funded Signal Science to upgrade PCPEM so that it could be included within a tactical support aid for RN ships. This improved model was called TERPEM and it was successfully evaluated by comparison with other propagation models for a set of standard scenarios [Branson, 1996]. TERPEM & NEMESiS have similar capabilities, and produced similar results, although TERPEM has stronger links to meteorological databases whilst NEMESiS is better integrated with RN radar models.

3.5 Data gathering and model validation

There have been very few experimental campaigns which have aimed to gather radar data in anaprop conditions, to validate radar propagation models, or to demonstrate the advantages of advanced propagation modelling over traditional propagation methods. This is mainly due to cost and a lack of appreciation of

how better environment modelling would benefit the specification and procurement of modern radar systems.

Anaprop data has been collected in the Persian Gulf following up anecdotal evidence and subsequent analysis [Devereux & Van Egmond, 1989] this data was analysed using the TEMPER PEM.

The performance of PEM models (TEMPER again) in predicting land clutter levels in littoral scenarios has been looked at by John Hopkins University [Reilly et al, 1992 and Lin & Reilly, 1995].

The SPANDAR satellite tracking radar in the US has been used to record anaprop radar data which has been used for environmental assessment testing [Gerstoft et al, 2000].

Another form of anaprop data has been provided by RCS measurement campaigns. The measurement of the RCS of military platforms is an important part of judging their susceptibility to being detected and supports research into reducing the RCS to make them more stealthy. European and NATO RCS measurement campaigns carried out in the Mediterranean have also shown the effect of ducting conditions. In these trials the RCS of a calibrated sphere appeared to reflect more energy that would be expected by simple radar equation analysis. This has important operational impact as the RCS of a platform is critical to modelling its survivability.

3.6 Clutter modelling in propagation models

The full backscatter of the propagation field can not be fully modelled by one-way propagation models, including PE models. Therefore surface clutter must be calculated from parameters derived from the propagation field at the clutter surface which provide input into empirical clutter models. In simple radar environments, clutter power returned for a given range is usually calculated from a clutter radar cross section (RCS) algorithm, which is usually a function of the incident angle and range gate size (from basic geometric theory), and the power at that range (given by the basic radar equation).

One problem with many surface clutter algorithms is that they are fits to experimental data that may have been influenced by anaprop conditions. Whilst this may lead to sensible results for a basic calculation, more detailed propagation modelling could lead to propagation effects being included twice. Fortunately the well-known Georgia Institute of Technology, or GIT, sea clutter algorithm [Horst et al, 1978] chose experimental data that was backed up by a full set of meteorological measurements.

Another problem is that in complex atmospheric conditions, such as anaprop, more complicated modelling is required to estimate the surface power and the incident angle of arrival. PEMs can simulate complex conditions but, to use existing clutter models, the output field must be converted back to radar equation-like variables [Dockery, 1990]. Electromagnetic image theory is used in PEMs to insert the earth's surface. Therefore surface reflection effects are

modelled by introducing an appropriate image antenna, effectively below the surface of the earth (as represented in Figure 3-1). The wavefront that seeds the PEM is modified to add this image antenna so that the correct Dirichlet boundary conditions for a conducting surface are met. The boundary conditions require that the field *u(z)* fulfils the polarisation dependent condition:

$$\partial_z u_{(z=0)} + \alpha u = 0$$

where
$$\alpha_v = \frac{ik}{\sqrt{\epsilon_e}}, \quad \alpha_h = ik \cdot \sqrt{\epsilon_e}$$
Equation 3.1

In these equations *k* is the wavenumber of the incident radiation and ε_e is the permittivity of free space. The boundary conditions used are polarisation dependent and α_V is used for vertical polarisation modelling and α_H for horizontal. The polarisation effect is generally fairly small at the angles relevant to propagation modelling and so vertical and horizontal coverage maps look virtually identical.
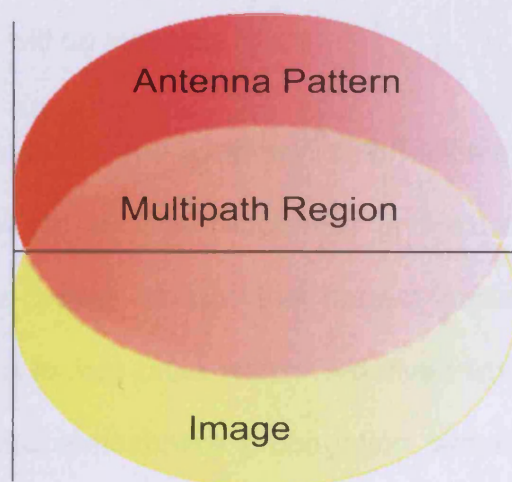
Figure 3-1 Image antenna used to simulate reflection and multipath

Use of image antennas accurately produces zero power at the sea surface to meet the boundary conditions. Any spectral analysis of this negligible field to assess angle of arrival will be sensitive to numerical instability. So PEM clutter modelling requires some way of removing the effects of reflection at the range of interest so that the incident energy field can be analysed to calculate range dependent clutter returns.

3.6.1 Reflection removal for surface power calculation

Groups working with PEMs have used several rough methods to calculate clutter returns without losing the multipath information.

The simplest method is to remove the image antenna entirely, which simulates freespace propagation through a stratified refractivity atmosphere. This produces range dependent clutter for simple cases where there is no ducting of energy back to the surface. However the multipath simulation is lost and so coverage information will be incorrect.

A well used approximate method [Dockery, 1990] estimates the mean height of the sea clutter based on surface roughness and extracts the power at this height. Although this power is not the correct surface power, it can be normalised by using a lookup table which is derived from the comparison of a pre-calculated standard atmosphere propagation simulation with a freespace radar equation model. This method can certainly show trends in the gradient of clutter strength and was therefore tested in early versions of the NEMESiS model described in chapter 5. The clutter simulation results showed that

multipath effects led to unrealistic frequency dependent fades (in reality smooth surface multipath reflections cannot lead to clutter fades at the surface because the surface is the source of the multipath) and therefore the method will not produce realistic clutter return power.

Another method described in early PEM literature sets the negative half of the propagating wavefront, $u(z)$ [7], effectively anything below the surface of the earth, in the image domain, to be zero at every step in the simulation process.

$$u'(z) = H(z) \cdot u(z)$$

where $\quad H(z>0)=1, \quad H(0)=\dfrac{1}{2}, \quad H(z<0)=0$ [8] $\qquad$ *Equation 3.2*

This is meant to simulate an absorbing layer. The half wavefront is then propagated forwards one step and the power is then evaluated in the surface bin of the wavefront. This drastic operation doesn't fit the boundary conditions of the problem and produces an effective impedance mismatch that causes similar reflections to the standard propagation method. Again, analysis using early versions of the model described in chapter 5 gave results that included unrealistic fades.

In both of these methods the look of the results can be improved by averaging over several height grid points, but this process is rather arbitrary. NEMESiS modelling showed that it was difficult to design a robust algorithm that worked in all cases.

---

[7]This notation is used more extensively in section 5.2 and appendix A
[8]H(z) is the Heaviside function

3.6.2 Angle estimation methods

Angles of incidence can be estimated from spectral analysis of the propagating wavefront. However the combination of the incident and reflected fields means that several bins representing a large chunk of wavefront above and below the surface need to be used to provide a reasonable spectrum. This makes localisation of an angle of incidence a difficult trade off.

Spectral analysis can be combined with the power estimation methods described above to try to localise the angle of arrival more precisely. However the angles produced in regions influenced by fades are unstable due to numerical inaccuracies. As with the power estimation, larger height windows can be used to get more consistent angles but the result can no longer be localised to the surface.

To achieve robust angle estimation current PEM models use hybrid methods that employ a mixture of ray tracing and spectral analysis. This requires two propagation models to be used and so could lead to inconsistent results.

3.6.3 Improved model

The approach developed in this thesis to estimate grazing angle and surface power exploits the symmetry about the surface to remove the reflections. The method and its implementation is described in section 5.3.1.

3.7 Other applications of propagation/clutter modelling

One interesting new area of research is the use of the radar to sense its own environment and therefore predict any gaps in its performance. These gaps can be assessed and, if necessary, measures can be taken to maintain mission effectiveness. For example, the platform could be moved to a safer location or the mode of operation of the radar could be changed to exploit the measured conditions.

Such rapid environmental assessment (REA) has traditionally been carried out using standard meteorological tools such as radiosondes, but these don't always give appropriate timely information. Environmental inversion techniques use the returns from the environment or the strength of signal in a point to point radio link to infer the local environment. Techniques such as frequency or antenna height diversity can help provide enough data to provide REA. Realistic operational techniques will generally not have enough data for a full unambiguous inversion but there is still scope for learning enough about the local conditions to assist with tactical advice.

Several researchers at SPAWAR in San Diego have looked at ways of achieving this inversion [Rogers, 1998, Gerstoft et al, 2000, and Rogers, 2000]. They have combined a complex optimisation algorithm with a PEM to estimate surface ducting and evaporation duct features. They have developed their refractivity from clutter technique in detail over a number of years and have examined the sensitivity in complex environments.

One area which the Gerstoft/Rodgers approach cannot examine is refractivity inversion using the true strength of the clutter returns. Their approaches have looked at the gradient and shape of the clutter returns and relative strengths because of the failure of PEM models to predict clutter strengths in a robust consistent manner.

3.8   Gaps in current research

This literature research has identified the following gaps in current research:

- Lack of anaprop radar data sets

- Limited modelling of anaprop effects

- Too simple description of the radar system in anaprop models

- Inaccurate PEM clutter strength models

- Limited use of 3D and video visualisation of PEM modelling

- No description of anaprop phenomena supported by real data and simulation analysis

- Limited clutter strength based radar inversion research

The remainder of this document will examine these shortcomings (building on the aims stated in section 1.1).

4 Anaprop Radar Data Collection

4.1 Introduction

Performance effects due to anaprop are highly variable and depend on a number of diverse parameters. Site specific clutter and meteorology combined with complicated waveforms, signal processing, and hardware limitations within the radar system can lead to a wide variety of effects. This chapter describes a series of radar trials which recorded radar data from an operational radar in anaprop conditions. The trials also quantified the strength of the phenomena which lead to anaprop by collecting meteorological data. The data sets collected formed a unique resource for anaprop research which will be examined in chapter 6.

4.2 Radar trials summary

Three distinct trials recorded data from several points in an RN radar system from baseband through to plot and track level. The radar that was instrumented was a high power coherent, E band (2.8 – 3.0 GHz), horizontally polarised, surveillance system optimised to search for fast moving airborne targets using MTI to suppress clutter. The radar had a bandwidth of around 5 MHz giving a range accuracy of 30 metres. The radar antenna was at a height of around 30 metres.

Meteorological data were also recorded, including occasional vertical atmospheric profiles using a high quality balloon GPS radiosonde system.

4.3   Data gathering system

High integrity (in-phase and quadrature or I and Q) raw data and associated radar status messages were recorded during the trials using RADAS (radar data acquisition system, shown in Figure 4-1) from an RN shipboard surveillance radar. This provided an excellent opportunity for measuring the clutter backscatter in a true marine environment.
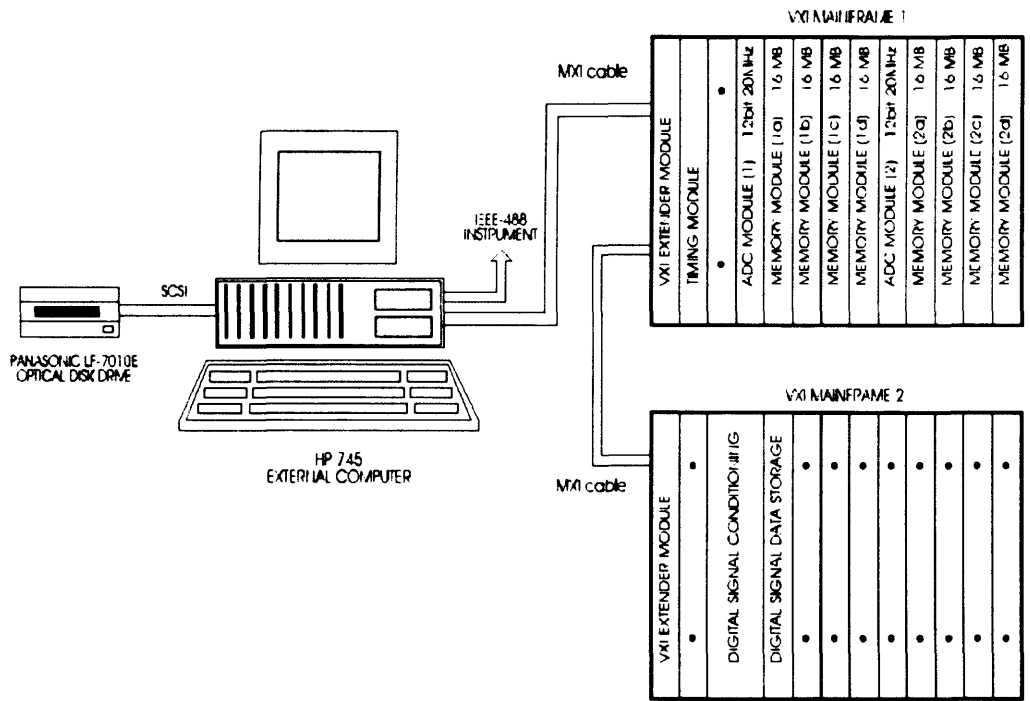
Figure 4-1 RADAS system

The RADAS data gathering system interfaced with the radar via eight interface cards, shown schematically in Figure 4-2. Some of the interface cards provided the analogue radar I, Q, and clock signals. Other interfaces provided digital information detailing the radar state at each transmitted pulse. These interface boards did not affect the normal operation of the radar.

RADAR CABINET   RADAS
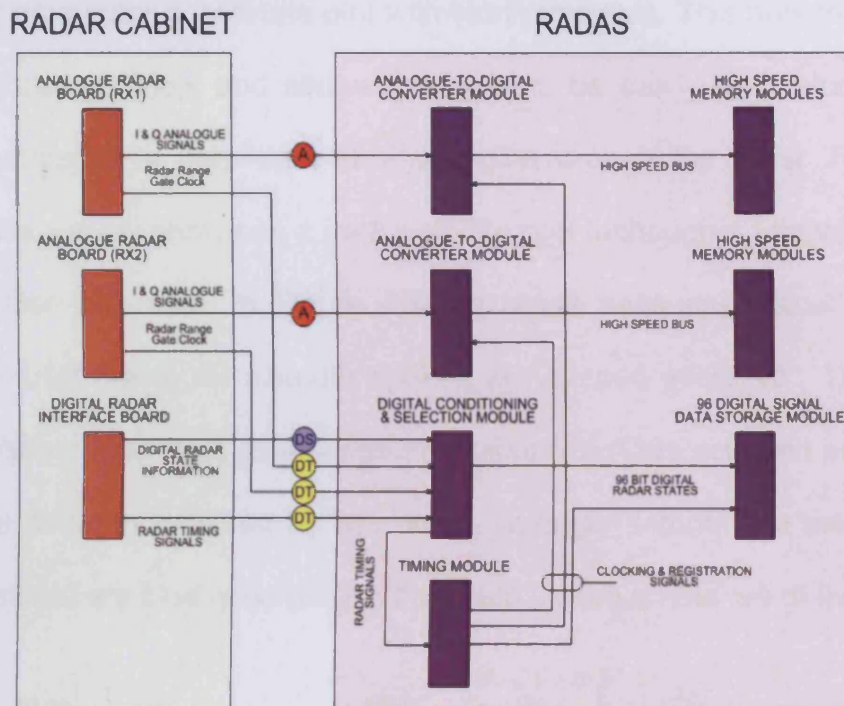
Figure 4-2 RADAS to radar interface

RADAS implemented several features that ensured low probability of measurement errors via strong data checking tags and software. There was a high level of flexibility within the basic equipment design, especially in the use of a complex programmable logic device (CPLD). The CPLD used the radar digital state information to filter the data recorded. This selective data capture allowed optimum use of the system memory available which would otherwise have become flooded by data rates of up to 80 MBytes per second.

The radar signals digitised included a mixture of real targets and clutter (sea, land or unwanted objects). An example of the data recorded during a two second radar scan is shown in Figure 4-3 which has been replayed in the lab in a plan position indicator (PPI) format. In a PPI format picture the radar data, which is received as the radar rotates in azimuth as a series of range swathes,

is laid out on a polar coordinate plot with North upwards. This presents the data from a bird's eye view and allows the data to be easily understood and be rapidly compared to map data for the region around the radar. Range and azimuth are usually shown as a dark web-like grid (although a normal Cartesian grid can also be used). In Figure 4-3 the range rings are spaced at 10 km intervals whilst the radial azimuth spokes are spaced every 10°. This type of plot shows the radar data as a series of spokes which are coloured according to the signal strength received by the radar. Stronger returns are coloured red, weaker returns are blue according to the scale shown on the left of the plot..
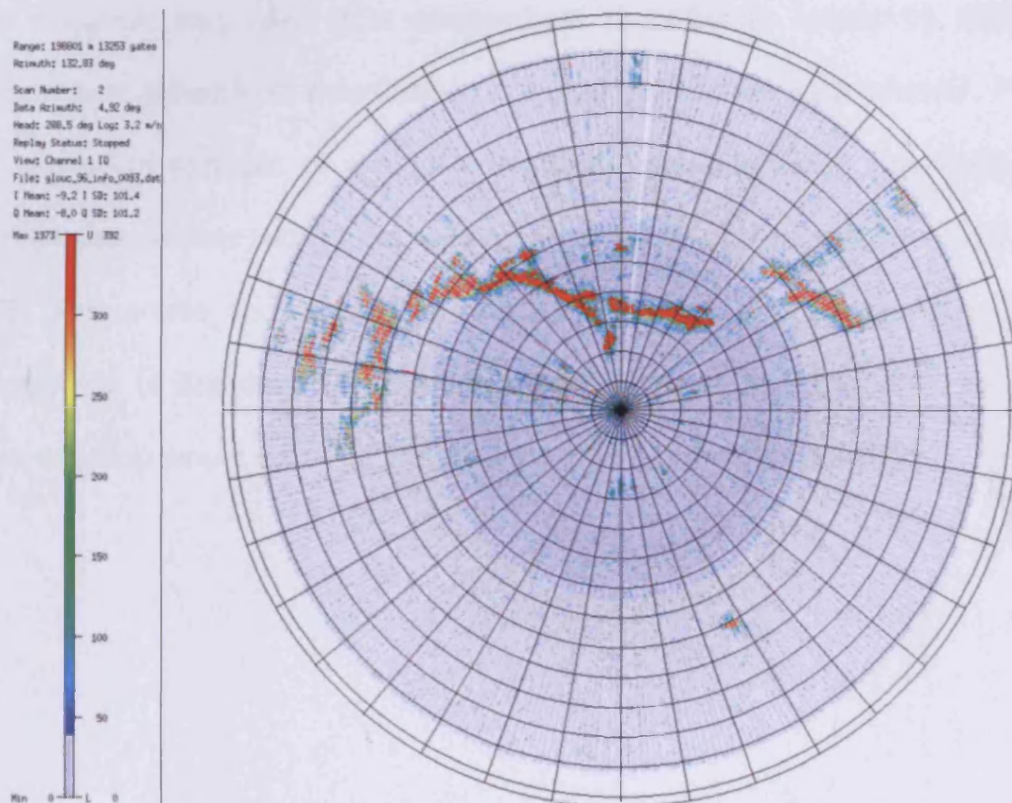
Figure 4-3 RADAS data showing one scan of radar returns on a PPI display. The scales used are described in the text

4.4 Atmospheric profile measurements

During sea trials, when clutter data was gathered, a GPS radiosonde system also provided spot measurements of the atmospheric parameters required for input into propagation prediction models. The modified refractivity M depends on altitude z, the radius of the earth r_e, the atmospheric pressure P (millibars), the temperature T (Kelvin) and the partial pressure of water vapour (which is related to relative humidity) e (millibars) according to equation 4.1.

$$M = 77.6\frac{P}{T} + 3.73 \times 10^5 \frac{e}{T^2} + 10^6 \frac{z}{r_e} \qquad\qquad \textit{Equation 4.1}$$

This equation was used in a spreadsheet to calculate refractivity from the atmospheric parameters downloaded from the radiosonde data receiver. Figure 4-4 shows an example of a modified refractivity profile which was calculated from measurements taken from a ship sailing south of Portland Bill on 24 April 1996. This profile shows that the atmosphere doesn't fit the standard linear atmosphere (a standard atmosphere profile is shown in Figure 2-7), but only weak anaprop would occur as the gradient of M is generally positive.
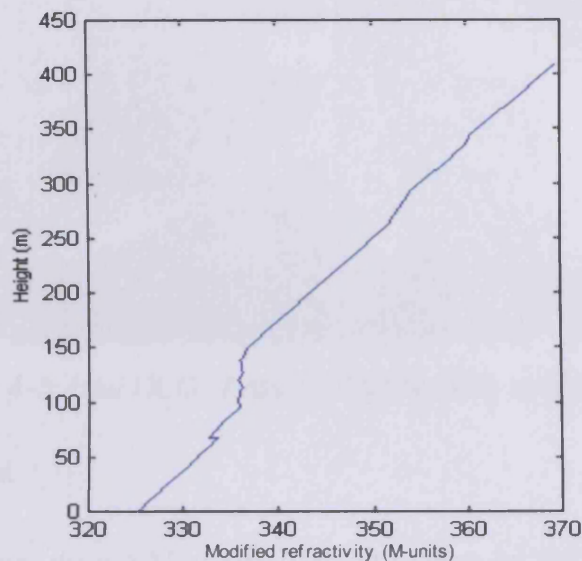
*Figure 4-4 Example of a modified refractivity profile from a radiosonde
ascent*

4.5   Trials description

4.5.1 Portland trial

Trials in the English Channel, South of Portland Bill, during April 1996 recorded

the effects of an evaporation duct on radar systems aboard HMS Gloucester

(an RN Type 42 destroyer) although no meteorological data were recorded.

4.5.2 Red Sea and Persian Gulf trial

The second trial, designated DLQ by the RN, ran from February to March 1997

on HMS Richmond (a Type 23 frigate). During this time she sailed from Port

Said to Abu Dhabi through the Red Sea and the Indian Ocean (as shown in

Figure 4-5). Strong ducting conditions, occasional heavy rain squalls and high

levels of land clutter were encountered and some very interesting results were

recorded [Mabogunje, 1997].

Figure 4-5 Trial DLQ. Type 23 frigate (left) and the trials route (right)

4.5.3 HMS Illustrious trial

Trial DMX took place during May 1997 whilst sailing on HMS Illustrious (an RN CVS aircraft carrier) between Singapore and Tokyo. The nature of aircraft carrier operations meant that, in general, littoral data collection was rare and no strong ducting was evident from on-board radar systems (although anaprop affects were visible on helicopter radar systems).

4.6   Method

At the beginning of each trial the RADAS equipment was installed into the radar system. RADAS was installed in the radar office in the ship which was one deck away from the operations room, where the radar operators actually used the radar picture. The radar and RADAS equipment were thoroughly checked to ensure that the equipment was working properly and had no effect on the operational use of the radar.

Once at sea, RADAS was used to record hundreds of short snapshots of radar data. Opportunistic recordings of passing targets and ships aircraft were taken to support signal processing research work and, during every hour of work, at

least one recording of a complete scan of returns was taken and reviewed to look for any unexpected radar phenomena. Internal ship's communications were used to coordinate data capture with radar operators and aircraft controllers.

To take a recording, the area of interest was assessed using the radar PPI repeater in the radar office or by talking to the ops room. An excel spreadsheet was then used to convert azimuth and range limits into the correct variables to program the CPLD in RADAS. Finally the appropriate capture macro was run on the HP controller computer to capture the required pulse patterns from the radar. This process was fairly time consuming which made it quite challenging to capture fast moving targets. During the trials, the author made several changes to the software in the system to reduce the delays in the process of capturing data.

Each data recording was carefully logged in an excel spreadsheet and also in the trials log book. Where possible, the local conditions were also recorded in the log book and the ship's regular meteorological measurements, recorded from a standard set of instruments at bridge level, were copied along with the bridge officer's comments on sea conditions.

The position of the ship was constantly measured using the ship's GPS which recorded positions at 10 sec intervals. The time stamp used by GPS sets the clocks in the ship's command system. The RADAS system was monitored to ensure that the system clock matched to ship's time to within a second.

Most of the recordings were taken during the day. At certain points in each journey the ship's route would pass close to land, such as at the southern end of the Red Sea or in the Straits of Hormuz. At these choke points the tempo of data capture was increased and recording continued during the night if necessary.

If there was any evidence of anaprop, either from reviewing the RADAS results or from discussion with RN radar operators, a concentrated set of runs were taken in an effort to support analysis of the phenomena involved.

Data was archived initially to the HP PC hard disk and then onto 1Gb optical drives.

Simultaneous recordings of radar plots and tracks were also recorded to see if anaprop and other clutter phenomena affected other parts of the radar system.

When ships operations allowed, two radiosonde launches were carried out during each day of recording and extra launches were made if anaprop returns were visible on the radar. Initially radiosonde launches were carried out at noon (which is the traditional time for meteorological measurements) but discussions with the ops room staff on HMS Richmond revealed that the most obvious anaprop phenomena occurred at dawn and dusk. The radiosonde launch times were adapted to try and capture the refractivity conditions at these important times.

At the end of the trial all the RADAS equipment was removed from the radar system and another system health check was carried out to ensure that the radar hadn't been affected by the trial.

After the trial, the clutter data was replotted and analysed. The raw data was reprocessed to look for anaprop clutter phenomena. All the trials data (including logbooks, spreadsheets, software, raw radar data, and radiosonde data) were carefully archived for later research work.

4.7   Results

The trials recorded thousands of instances of radar clutter. This section highlights some of the most important sets including several that showed anaprop phenomena. Some other examples of radar data are shown in Appendix E.

4.7.1 Portland trial

Figure 4-6 compares radar returns gathered from just south of Portland Bill on two consecutive days during the April 1996 trial.
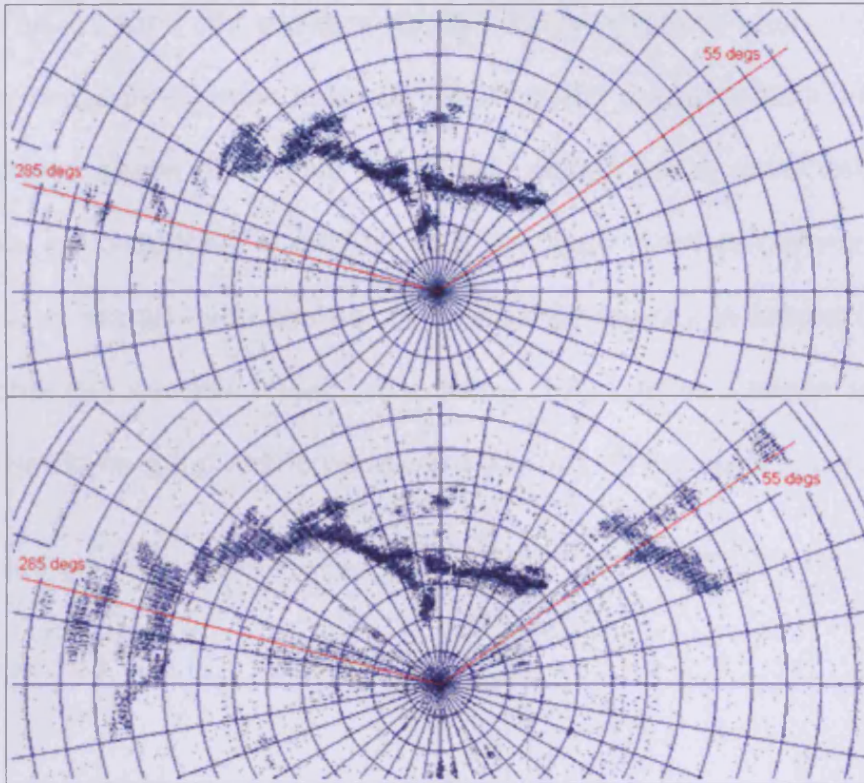
Figure 4-6 Two PPI views showing a change in radar clutter visibility

As in previous PPI figures, the range rings are separated by 10 km and the azimuth spokes are at 10° intervals. In this case the radar data (land clutter from the south coast of England) has been simplified by comparison to a threshold value and so is shown as blue where the threshold has been exceeded. The same threshold was used in both PPIs.

Figure 4-6 shows that the land clutter visibility has changed markedly between the two sets of data. The reasons for this will be examined in section 6.1.

4.7.2 Red Sea and Persian Gulf trial

During trial DLQ stronger ducting phenomena were common. Figure 4-7 shows two modified refractivity profiles measured by weather balloon ascents during

the trial. The left hand plot shows a strong negative gradient where the modified refractivity drops by 60 units between 300 and 400 metres altitude indicating a strong surface based duct. This led to skip effects which were visible in the radar data, as described in section 6.6. The right hand refractivity profile in Figure 4-7 shows an even sharper (a drop of 50 M-units in around 20 metres altitude change) surface based duct below 100 metres altitude which was recorded whilst anaprop phenomena were obvious on the radar recordings.
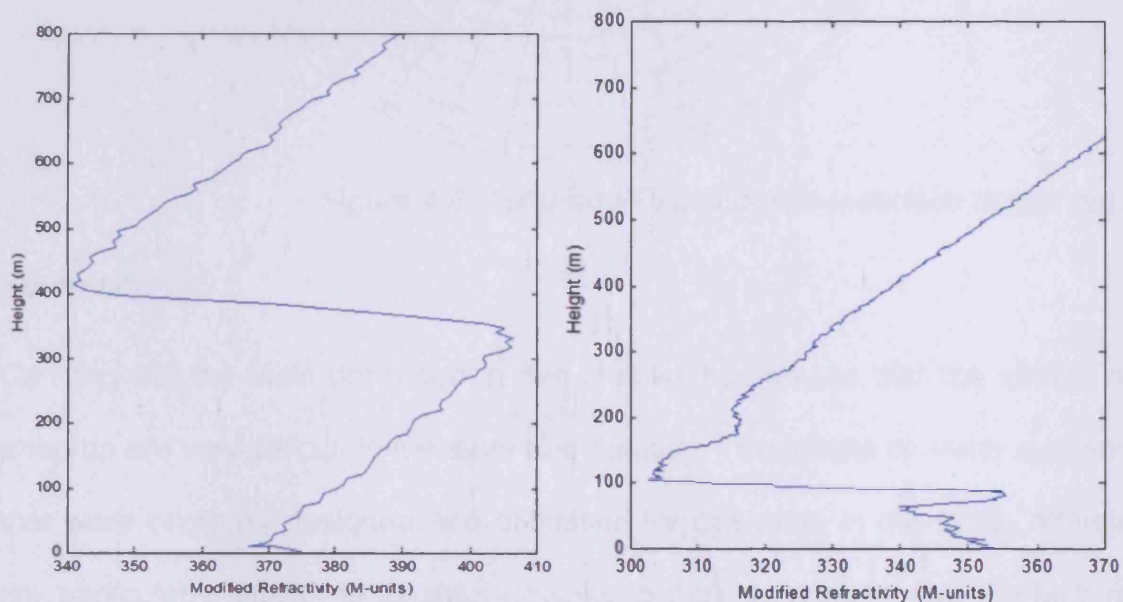
Figure 4-7 Strong ducts measured in the Middle East

Figure 4-8 shows a PPI map of the clutter returns from one radar scan (a few seconds worth of data) gathered around the time that the second duct in Figure 4-7 was measured. This plot shows radar returns out to 150 km (with range rings every 10 km, and azimuth rings every 10°). This data has been false coloured to show sea clutter in red and land clutter in blue and is analysed in detail in section 6.2.
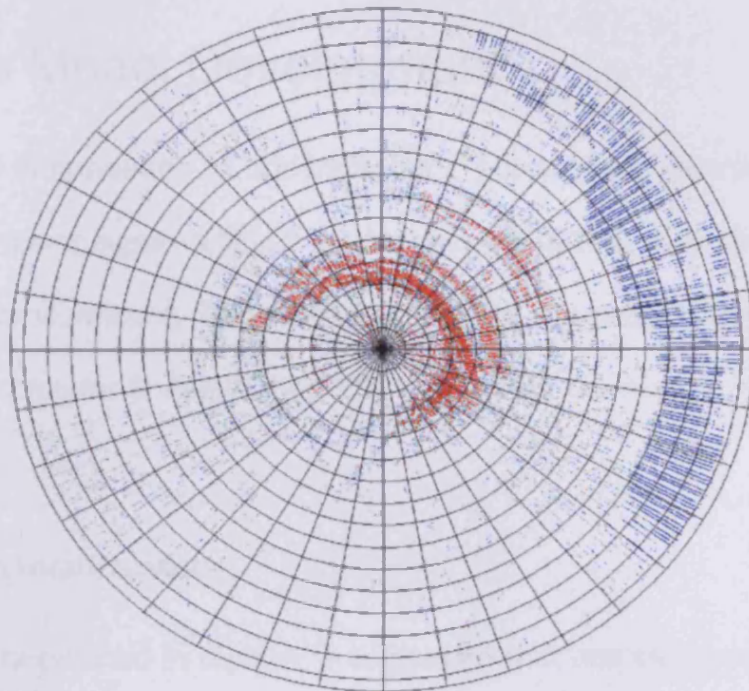
Figure 4-8 Cluttered PPI plot due to a surface based duct

4.8 Summary

Carrying out the trials described in this chapter has shown that the effects of anaprop are very difficult to measure and quantify. The effects on radar systems that were originally designed and optimised for operation in the North Atlantic are particularly difficult to ascertain thanks to their complexity and the lack of detailed data collection facilities.

The trials recorded many instances of radar data that were potentially influenced by anaprop phenomena. The meteorological data taken showed that ducting atmospheric conditions were present. To understand this data more thoroughly and capture the phenomenology for research and procurement purposes, a new model was needed. Its development is described in the next chapter.

5 Anaprop Model Development

A new model was needed to understand the phenomena recorded during the experimental campaigns outlined in the chapter 4 and their implications for future radar procurement. This chapter describes the model developed by the author whilst chapter 6 details how the model has been used to analyse the radar data.

5.1 Initial design requirements

The radar data outlined in chapter 4 suggested that non-standard atmospheric conditions, as measured by radiosonde, produced increased clutter which in turn lead to the various radar system effects. As discussed in chapter 3, no pre-existing PEM model can adequately simulate clutter power levels and system effects and so a new approach was needed that met the following three criteria:

- Firstly a new propagation model was needed that would be flexible enough and fast enough to allow a variety of research work to be carried out in a timely way. To model realistic scenarios, the propagation model must be able to model range dependent refractivity conditions over sea and land. The split-step PEM model fits these requirements.

- Secondly a new method was required for using the modelled propagation field to simulate the clutter returns in a radar receiver.

- Thirdly these two modules needed to be wrapped by a detailed but generic radar system simulation and data visualisation tool to allow realistic PPI views to be created for comparison with real radar data. This radar system model could then also be used for MOD procurement and research.

The entire system was named the Naval Electromagnetic Environment Simulation System or NEMESiS. The software project was developed within an ISO9001 quality framework which required various documents to be completed as the tool was developed that encouraged planned design, code reuse and algorithm verification. NEMESiS also needed to be applicable to wide range of other tasks outside the scope of this thesis and so needed to be versatile and easy to use. Matlab was chosen as the development language because it was easy to develop and test, supported multiple platforms (Windows, Linux and Unix), and could be rapidly integrated with existing research software.

Figure 5-1 shows a flow chart summary of the completed model with data flowing from top to bottom (the acronym AOA in the figure stands for angle of arrival). The inputs and outputs to the model are provided in Appendix D.
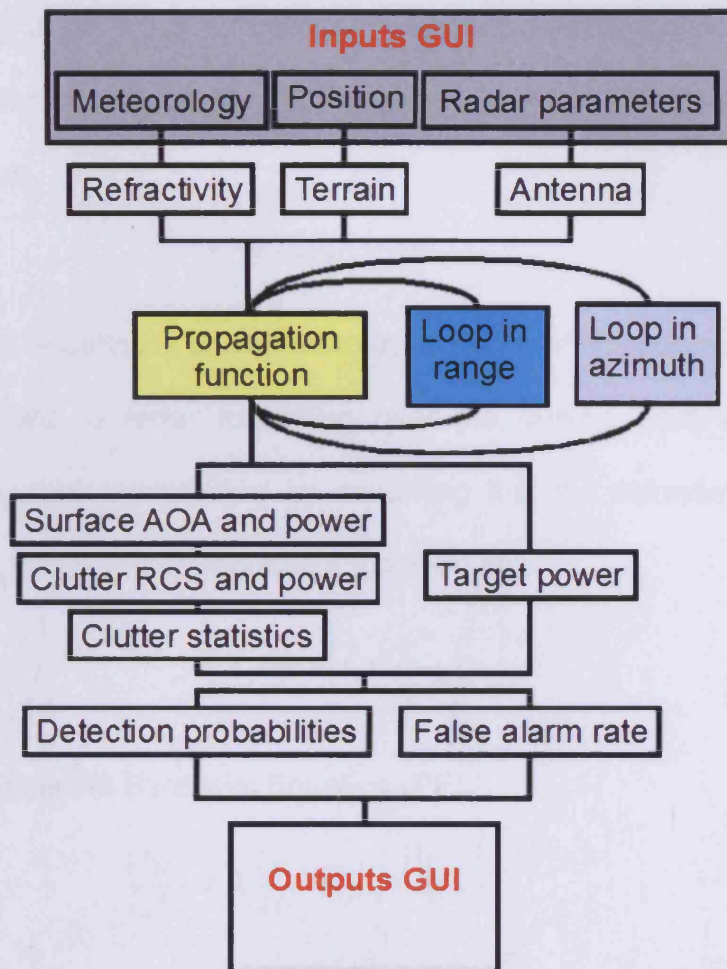
Figure 5-1 Summary of NEMESiS model design

5.2   Propagation model

A detailed propagation model was coded, initially based on a terrain following propagation algorithm [Barrios, 1994], and later modified to include rough surface modelling [Kuttler & Dockery, 1996]. The split-step parabolic equation model (PEM) approach was implemented to provide the best compromise between speed, accuracy, and flexibility.

The parabolic equation is derived from Maxwell's equations for electromagnetic propagation via the Helmholtz equation (shown in equation 5.1 where E is the

electric field, k is the wavenumber and n is the refractive index) that describes the propagation of electromagnetic waves through a medium with variable refractive index.

$$\nabla^2 E + k^2 n^2 E = 0 \qquad\qquad Equation\ 5.1$$

The Helmholtz equation is converted to the curvilinear co-ordinate system which is most relevant to radar modelling over the curved earth's surface. The equation produced is simplified by assuming that the refractive index varies slowly with range, x, and introduces a modified field u:

$$E(x,z) = u(x,z)\frac{e^{jkx}}{\sqrt{x}} \qquad\qquad Equation\ 5.2$$

and this produces the Parabolic Equation (PE):

$$\frac{\partial^2 u}{\partial z^2} + 2jk\frac{\partial u}{\partial x} + k^2\left(n^2 - 1\right)\cdot u = 0 \qquad\qquad Equation\ 5.3$$

where u is a modified electromagnetic field (with wavenumber k), and n is refractive index. Both u and n vary with altitude z and range along the ground x. This equation can be solved by Fourier transforming, integrating and applying boundary conditions to give a vertical wavefront solution at one range $u(x+\Delta x)$ based on the solution a small (small enough that horizontal changes in refractivity are negligible) range step back towards the origin, $u(x)$:

$$u(x+\Delta x,z) = e^{j\frac{k}{2}\left(n^2-1\right)\Delta x}\cdot \Im^{-1}\left[e^{-j\frac{2\pi^2 p^2}{k}\Delta x}\cdot \Im\left(u(x,z)\right)\right] \qquad\qquad Equation\ 5.4$$

where p is the Fourier variable (making a Fourier pair of z) and is equivalent to the vertical component of the wavenumber k propagating at an angle θ. So:

$$p = k\sin(\theta)$$ <div style="text-align: right">*Equation 5.5*</div>

Careful Fourier transformation of the radar gain pattern is used to create an initial vertical slice solution at range zero to meet the boundary conditions for propagation above a conducting Earth surface.

The solution for all ranges can then be calculated by iteratively stepping out in range in steps of length *Δx*. This process is described in more detail in Appendix A.

The two exponential terms in equation 5.4 act as non-linear Fourier shifts. A linear shift would merely move the waveform either up or down according to the Fourier shift theorem:

$$u(z + z_0) = \mathscr{F}^{-1}\{U(p) \cdot e^{-ipz_0}\}$$ <div style="text-align: right">*Equation 5.6*</div>

Therefore the *p²* in equation 5.4 exponent spreads the field non-linearly in altitude and the same spreading occurs for every step. The *n²-1* exponent (note that *n is a function of x and z*) refracts the wavefront in the angular domain in a potentially different way at every range step according to the scenario's refractivity. If the refractive index is zero (or a constant) then no refraction occurs and freespace propagation can be modelled which provided a useful test case for comparison with the radar equation.

5.2.1 Discretisation and run set-up

The continuous (in height) field equations from the theory above were mapped onto a discrete modelling grid covering the area of interest at a suitable accuracy.

Achieving this mapping to make robust software was not trivial but the flexibility of Matlab allowed various schemes to be trialled and then tested to ensure a that a robust and realistic solution (with a flat horizon and sensible continuous pattern curvature) was modelled.

The grid height step used was calculated at run-time from the maximum modelling angle required (which was a user input to the software; see appendix section D.1 for a list of user input parameters) because the altitude and modelling angle form a Fourier pair of variables. The approximations made in the PEM theory mean that the radar field can only be accurately modelled up to 10° above and below the horizontal. The effects of anaprop are usually only evident in the region of 1-2° around the horizontal and it was found that maximum modelling angles of between 5° and 7° produced a smooth accurate field and with low run-times. This leads to height steps of around one metre for a 3GHz transmit frequency. The size of the modelling grid in altitude was then defined by the maximum height of interest (defined by the user) divided by the height step.

Range step size can be much larger (up to 1500m) and so the model was usually set up to run with a few hundred range steps to produce a smoothly

sampled field. The refractivity and terrain profiles were then sampled to fit to the simulation grid.

The gain pattern of the radar antenna, *g(θ)*, was sampled onto the correct angular grid to give *g(p)* and then Fourier shift theory was used to shift the antenna in height to the antenna altitude, z_a.

$$u_1(0,z) = \mathscr{F}^{-1}\{g(p) \cdot e^{-ipz_a}\} \qquad \text{Equation 5.7}$$

This pattern was then Fourier shifted again to provide any elevation angle offset necessary to model antenna tilt, θ_a, by multiplying u_1 by $e^{-ik\sin\theta_a}$. The pattern was then reflected about the origin and subtracted from itself to create a voltage field consisting of a real antenna and its image which is the seed for the propagation loop.

$$u(0,z) = u_1(0,z) - u_1(0,-z) \qquad \text{Equation 5.8}$$

Note that this meant that the modelling grid and the refractivity grid (which was also reflected about the chosen origin) had to be doubled in size. This increase in the modelling domain has an impact on the speed of the FFTs used in the propagation loop (the time to compute an FFT scales with *N.log(N)*) and on memory usage.

5.2.2 Domain filtering

Another important problem for PEM models is domain truncation. As the model steps out in range, the propagating field being modelled carries on extending to the edges of the modelling range and then begins to alias back into the central

region of interest. This would cause unrealistic multipath. To counter this, the calculation grid was enlarged above and below the region of interest and an attenuation filter was applied. Any energy propagating into this region is then increasingly reduced in power as it propagates to the edge of the new grid. To do this the calculation grid was doubled in size again and a Hamming window was used as an attenuation filter. At the end of the simulation the filtered region is thrown away (along with the image region) to leave the required region of interest. This further increase in the size of the modelling domain again added a considerable processing overhead and so a range varying filter was designed which allowed smaller filtering regions to be used. Close to the antenna a strongly attenuating high order Hamming window was used because the propagation simulation initially includes some high angle components that can rapidly alias round the calculation domain. At longer ranges only the low angle components remain and so any escaping energy will spend longer in the filter region and so a lower order filter could be used. This allowed some of the longer range data in the filtered regions to be recovered for performance calculations.

5.2.3 Propagation loop

The propagation loop required the majority of processing power used by the model. Therefore it was designed to run as quickly as possible. Several programming strategies were used to achieve this in Matlab. Firstly all variables were preallocated to reduce hard drive access during memory swapping. As many variables as possible were pre-calculated outside the main loop. An

innovative system of refractivity field interpolation was used to reduce memory usage in the loop to provide as much space for the memory intensive propagation field. The Fast Fourier Transform (FFT) [Brigham, 1974 and Bracewell, 1996] and other types of vectorised coding were used within the main modelling loop to keep run times down.

These efforts led to a fast and efficient model that could model a region 1500 metres high and 200 km in range on a high resolution grid in around 30 seconds.

5.2.4 Terrain modelling

The basic PEM propagation loop creates a model over a smooth curved surface. Methods for including terrain all work by morphing the terrain back to a smooth surface and applying the same transformation to the propagation field. This allows the standard propagation method to be used. There are two ways to do this; an optimum technique that can be used for shallow land gradients [Barrios, 1994] and a simpler staircase method that is used when propagating over steep land profiles [Levy, 2000].

The optimum technique bends the rays, using a Fourier shift related to the terrain in the current propagation step, either upwards or downwards to account for the gradient change of the terrain. This adds a new term, $z.T''$ where T'' is the second differential of the terrain $T(x)$, into the n^2 exponent of equation 5.4 to give equation 5.9. The maximum amount of ray bending is limited by the height step used in the grid and so the maximum terrain angle that can be modelled is

around ten degrees. Reflections from the terrain are then handled in the same

way as the normal curved Earth surface model.

$$T'' = \frac{d^2 T}{dx^2}$$

$$u(x + \Delta x, z) = e^{jk\left\{\frac{1}{2}(n^2 - 1) + zT''\right\}\Delta x} \cdot \Im^{-1}\left[e^{-j\frac{2\pi^2 p^2}{k}\Delta x} \cdot \Im\left(u(x,z)\right)\right] \qquad \textit{Equation 5.9}$$

The simple technique treats the terrain as a series of steps. This staircase land

is modelled by deleting the bottom elements in the current propagation step as

if they had been absorbed by striking a cliff (as shown in Figure 5-10 steps (2)

and (3)). Conversely a section of zero field is added when the simulation passes

over a downward step in the land height (step (4) of Figure 5-10). To maintain

symmetry the same change has to be made in the image part of the

propagating wavefront.

u(x_n,z)

Real domain
z>0

Image domain
z<0

u(x_{n+1},z)

u(x_{n+2},z)

u(x_{n+3},z)

(1) Propagation loop approaches terrain step after n steps forward. u_n is a vector of field strengths

(2) At step n+1 current slice is in front of terrain. Centre is cut out (red elements) and zeroes are added to top and bottom (blue elements)

(3) Top and bottom sections are reconnected to remove the region absorbed by the terrain

(4) Zeroes (blue elements) added to centre after terrain to simulate empty region containing no energy. Ends are chopped off (red elements)

Figure 5-2 Staircase terrain modelling method

This method effectively creates a series of knife edge diffraction points and doesn't completely fit the boundary conditions at an upward slope, which leads to some high angle reflections.

These methods were combined and implemented in NEMESiS as part of the main propagation routine. When the propagation loop reaches a change in terrain the angle of the change is assessed and if it is below a critical value (calculated from the simulation grid set up) then the angle shift method is used. When above this limit the staircase method is used. To reduce calculation time this hybrid method was carefully vectorised.

5.2.5 Propagation results

Figure 5-3 shows an example of the output of the model in a simplified environment with labels highlighting the major features of the propagation slice. The plot shows pattern propagation factor, denoted by a colour scale, as a function of range and height.
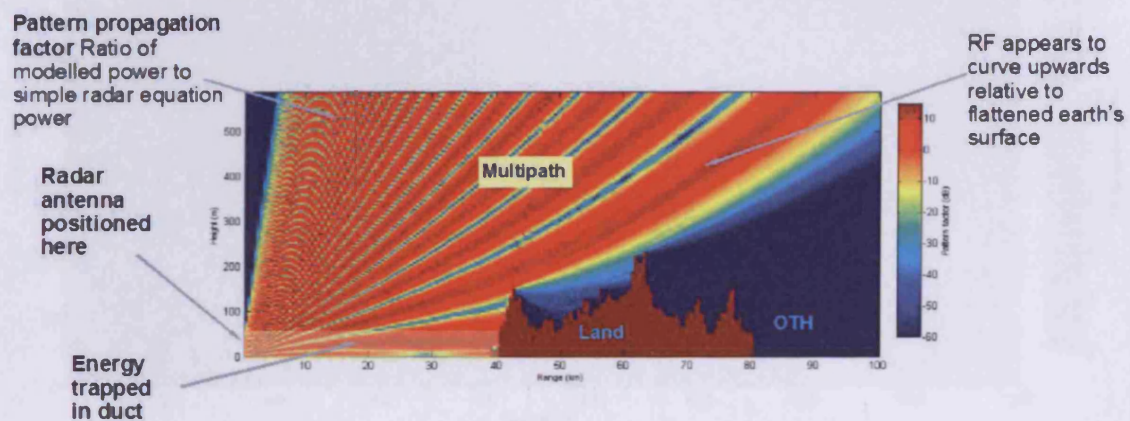
Figure 5-3 Example NEMESiS plot

The plot is dominated by the multipath interference region in which standard atmosphere propagation dominates. Close to the radar, a duct has trapped energy near to the sea surface. This energy runs into a landmass, denoted by the dark red region, which leads to reflections at high angle and visible diffraction behind peaks into shadow regions. At longer range, over the horizon (OTH), the plot is dark blue denoting that no energy has propagated into the region. It should be noted that in a pulsed radar system only a thin vertical slice of this energy exists at any one time as the pulse propagates out from the radar, so the plot shows the envelope of the pulse propagation during one whole receive period.

Another example is given in the following graph which represents the radar coverage in a ducting atmosphere that was measured by a radiosonde launched from the HMS RICHMOND in the Red Sea (the modified refractivity profile is shown in the right hand plot of Figure 4-7).
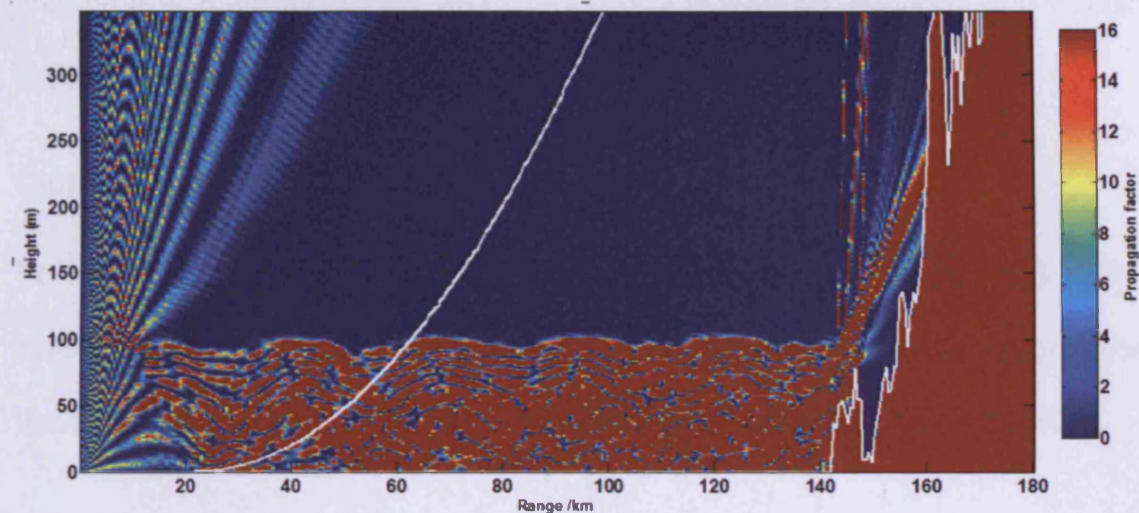
Figure 5-4 shows a ducting radar coverage plot, with propagation factor again proportional to the colour scale on the right of the main graph. The radar horizon, the normal lower limit of radar coverage in a standard atmosphere case, is shown by the white line. This line curves upwards because the x-axis represents a spherical earth surface. Land is marked by the red area bordered by a white line on the right hand of the plot. Energy has been more strongly trapped next to the sea surface than in Figure 5-3 because the modified refractivity gradient at the top of the duct was more severe. This has led to propagation well over the radar horizon, and a complex interference pattern is visible within the duct. Normal multipath lobes are visible above the duct.

The results above and continuous testing by visual comparison with results from other models [Branson, 1996] show that the propagation module successfully modelled the effects of refraction, diffraction, terrain, shadowing and reflection. This is a great step forward from simple radar models in which all these phenomena must be added using different approximate methods and 'magic' numbers.

5.3   Clutter modelling

To model surface clutter returns from a range gate requires the RCS of the clutter dominating the range gate and the incident energy at the range gate. Various clutter algorithms have been coded into NEMESiS to calculate RCS.

The GIT algorithm [Horst et al, 1978] has been used in NEMESiS to define the mean radar cross section (RCS) for sea clutter (using a similar method to Dockery [Dockery, 1988 and Dockery, 1990]). For probability of detection and clutter simulations the K-distribution statistical variation was used as defined in NECAPS.

The algorithms described in NECAPS were also used for defining land clutter to allow comparison with other radar models that use NECAPS. The model defines land clutter RCS according to land type and the statistical variation is described using the Weibull distribution with a spikiness dependent on range gate size. The NECAPS model is not flexible enough for detailed environmental scenarios and so the land clutter model described by Billingsley [Billingsley,

2002], which is based on 40 years experimental data gathering and analysis, has also been implemented and is used for the majority of research work.

These models require incident grazing angle to be calculated and so, to counter the problems described in section 3.6, a new technique has been implemented that can derive the incident energy and grazing angle.

5.3.1 NEMESiS surface propagation estimation

The approach used to estimate grazing angle and surface power in NEMESiS exploits the symmetry about the surface to remove the reflections.

At the reflection surface all the wave components pointing upwards must be reflections. Therefore the reflections can be removed by decomposing the wavefront, $u(z)$, using a Fourier transform to give $U(p)$, the wave components of u as a function of the Fourier variable p (which is equal to $k.sin\theta$). All the upwards components, one half of $U(p)$, were then set to zero. This is mathematically equivalent to multiplying $U(p)$ by the Heaviside function, $H(p)$, which is zero for negative values:

$$u'(z) = \mathscr{F}^{-1}\{H(p) \cdot \mathscr{F}\{u(z)\}\}$$

Equation 5.10

Inverse transforming the result returns a modified wavefront, $u'(z)$, with the upward travelling part removed. At most heights within this wavefront this process will produce nonsense because components could be travelling in the upwards direction for reasons not related to reflection. However, close to the surface the wavefront will be made up by the incident energy only. The process

is summarised in Figure 5-5 where the upward propagating waves in *u(z)* have been removed to give *u'(z)*.
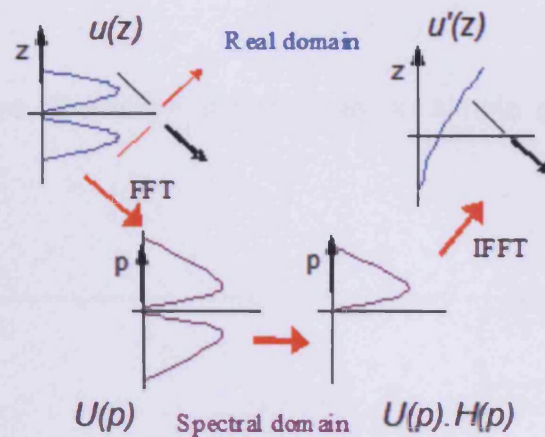
Figure 5-5 Summary of the NEMESiS surface propagation estimation technique

The surface propagation factor, $F_s{}^4$, is then just the propagation factor in the modified wavefront bin at zero height and the angle of arrival, Φ, can be calculated from the phase, $\phi(X)$, difference of the wavefront in the grid points either side of zero height ($+\delta z$ and $-\delta z$):

$$F_s^4 = u'(0)^4 \qquad\qquad\text{Equation 5.11}$$

$$\Phi = \frac{1}{k}\{\phi(u'(\delta z)) - \phi(u'(-\delta z))\} \qquad\qquad\text{Equation 5.12}$$

After the surface effects have been calculated the modified wavefront is then discarded and the original wavefront is used to continue the forward propagation loop.

5.3.2 Testing

The NEMESiS surface propagation estimation has been tested against radar equation models for simple environments. Free space propagation was

modelled in NEMESiS by setting the refractivity to zero and the results accurately matched the R^{-4} surface power fall-off predicted by the radar equation.

The angle estimation also matched correctly to simple geometrical theory as shown in Figure 5-6.
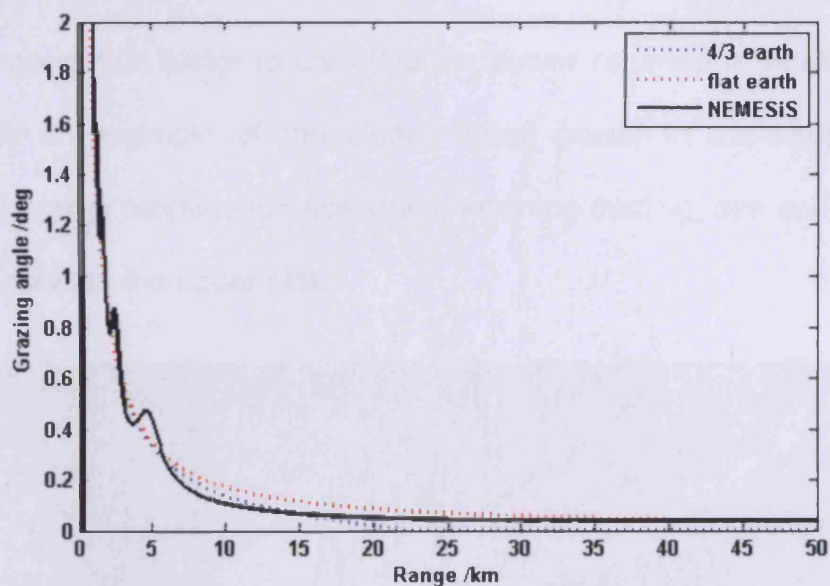
Figure 5-6 Comparison of NEMESiS grazing angle calculation (unbroken black line) with simple geometry approaches based on different assumptions (broken lines)

Note that this plot shows that this new algorithm still gives a small amount of fade (at around 4 km) but the resultant clutter power proved to be smooth enough for accurate consistent radar modelling.

In anaprop cases, there are no standard models to compare with but the clutter levels modelled using this new method appeared to match qualitatively by eye to the propagation fields that produced them (for example examine Figure 5-7

which shows a correlation between surface features and the clutter power at the radar).

5.3.3 Clutter generation summary

After the coverage pattern had been generated, further processing produced the incident angle and propagation factor at the earth's surface. The angle was used to calculate the mean clutter RCS which was then combined with the surface propagation factor to calculate the power returned from clutter. Figure 5-7 shows an example of the clutter return power in the lower line plot, calculated from a propagation scenario containing ducting, sea and land clutter which is shown in the upper plot.
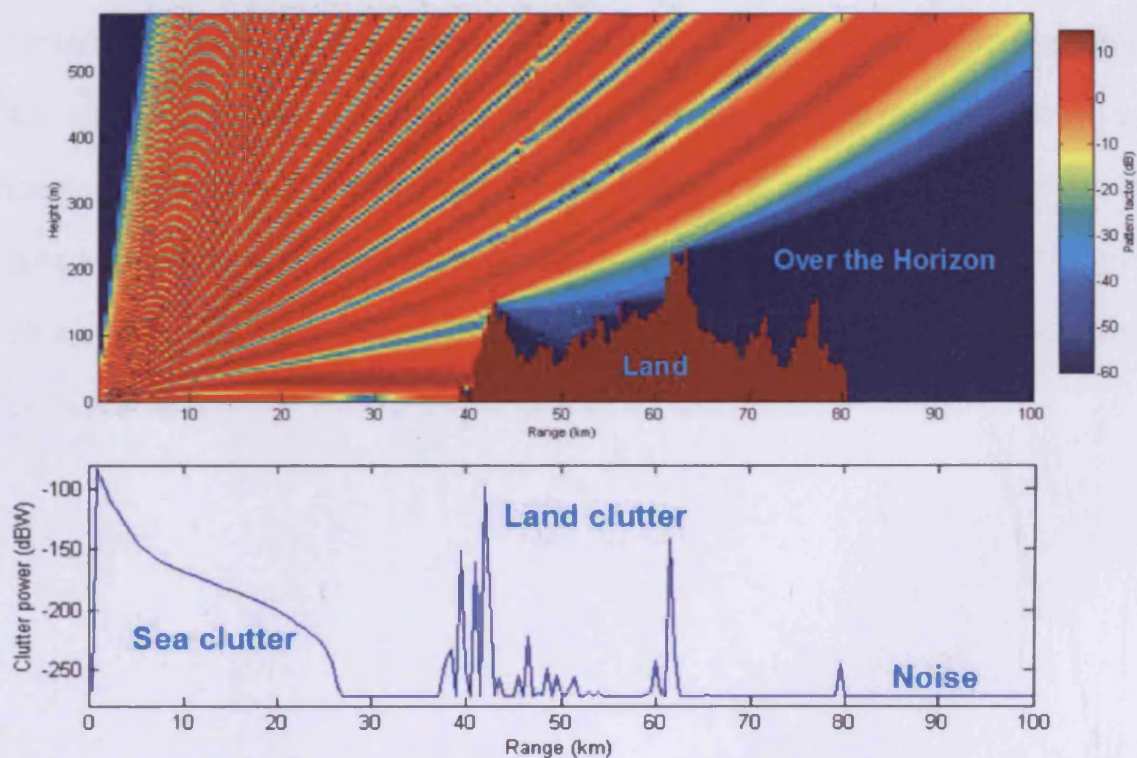
Figure 5-7 Clutter output shown with propagation model

The calculated clutter power then becomes the basis for the analysis of the effects of complex radar environments on radar signal processing, detection, and tracking strategies.

5.4　3D NEMESiS

The core NEMESiS propagation loop produced a 2D slice of propagation. This slice can be displayed on a detailed plot that provides a lot of information to a scientist. However most people are more familiar with a PPI view of radar data and the PPI can show a range of phenomena simultaneously in an accessible way. PPI plots are also easier to visually compare with radar trials data for rapid qualitative comparison.

NEMESiS was therefore adapted to model whole littoral scenarios incorporating full azimuthal clutter variation in anaprop conditions. This was achieved by looping round the 2D model many times to produce many thin cake slices of propagation that were built up to create a 3D propagation factor grid. This grid defines a curved earth 'cylinder' spread out over the earth's surface and centred on the radar.
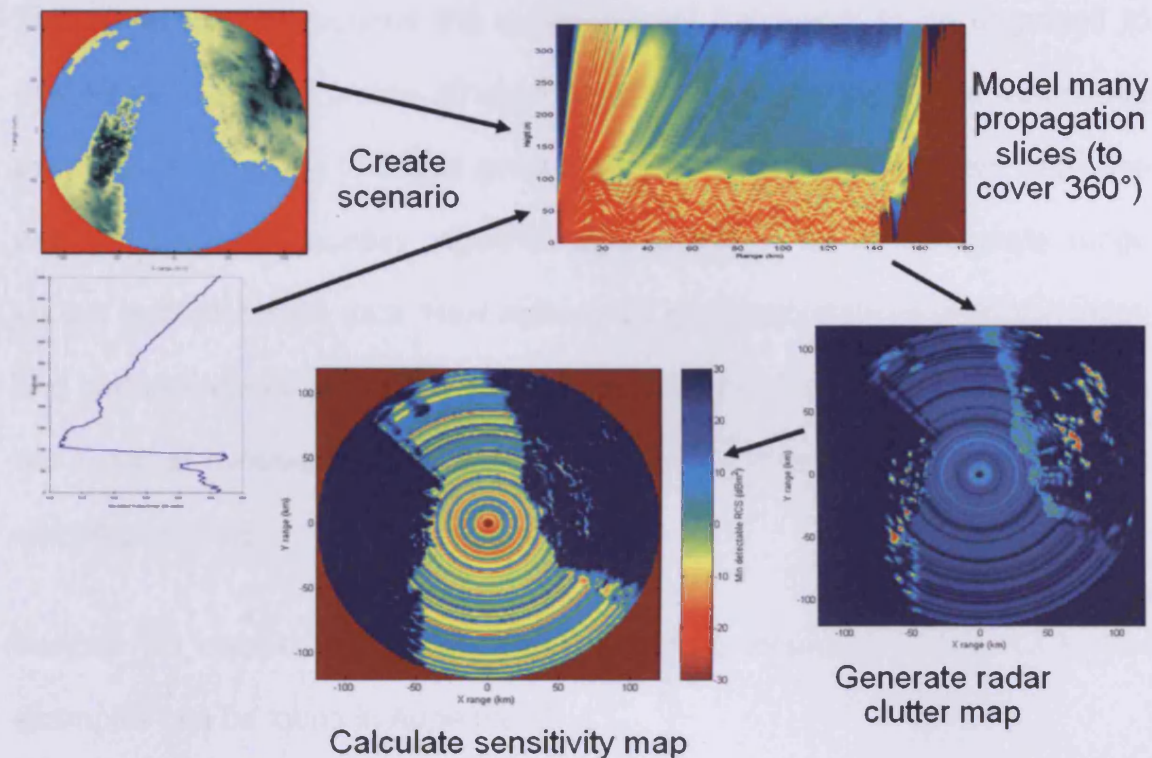
Figure 5-8 Summary of NEMESiS 3D

The 1D clutter returns calculated from each slice were stacked up to give clutter power versus range and azimuth. Target returns could be calculated for any part of the 3D propagation field (range, azimuth and height), but usually a single user selectable height slice was used to create probability of detection for a given target positioned at any range and azimuth around the radar. The 2D range/azimuth data were plotted on PPI plots to allow a large amount of model outputs to be analysed visually at once. The whole 3D modelling process starting from environmental inputs, producing 2D propagation slices to build a 3D grid, allowing the creation of 2D PPI plots of radar outputs is shown as a flow diagram in Figure 5-8.

The 3D simulation required the environmental framework to be upgraded to interpolate in 3D and create 3D input data. For example, the model was coded to use Euler rotations to create great circles for searching the terrain database and the Vincenty geodesy algorithm was employed to give accurate range versus azimuth terrain data. New techniques, especially the use of vectorisation and software speed profiling, were implemented to keep the run times down to the order of minutes and make efficient use of computer memory to prevent software crashes.

Various 3D outputs are shown throughout this document and some further examples can be found in Appendix C.

5.5   Radar model wrapper

Many propagation models only create the raw propagation and clutter data but can't show their effects on real world systems. One advantage of the PEM approach is that all the information needed to define the radar performance is calculated at once. This information can then be used like a look up table to simulate realistic scenarios involving complex radar systems and detailed target movements. To take advantage of this, a radar model wrapper was added to NEMESiS that combined elements of traditional radar performance models with the capability to define multiple processing regions for each radar that could emulate the effects of the environment on Doppler radar and pulse compression.

5.5.1 Burst effects

One of the most important MTI and Doppler waveform effects simulated was multiple time around returns. To do this each waveform was modelled out to a range defined by the number of pulses multiplied by the maximum unambiguous range of the waveform (as defined by the PRF of the waveform). The output data was then post processed by folding in range by iteratively adding the clutter from longer ranges into the unambiguous range (clutter statistical parameters were also folded using a sum weighted towards the strongest clutter sources). Any large changes in clutter level (greater than a fixed threshold) caused by this folding process were modelled to reduce clutter cancellation effectiveness. As discussed in section 2.8.5, folded in clutter leads to a broad Doppler response that breaks through MTI and Doppler filters. A simple model was used that applied a constant reduction in clutter cancellation for affected cells. The effects of multiple time around returns caused by anaprop were then visible in the outputs from the model.

5.5.2 Clutter detection thresholds

It was also vital to get the performance predictions correct because they might be used operationally as the basis for a change in tactics or a change of radar mode. Many traditional model thresholding methods are known to overestimate radar performance because of simplifications made to implement the complex statistical calculations required (see also section 2.8.2). A new implementation of statistical threshold code, developed by UCL, was added to NEMESiS to ensure accurate performance prediction in mixed noise and clutter

environments. This algorithm generated a threshold to noise ratio (T_0) as a function of the clutter to noise ratio (CNR), the number of incoherent integrations (n_I), the spikiness (α for Weibull and v for K), and the constant false alarm rate ($CFAR$) required.

$$T_0 = TNR(CNR, CFAR, n_I, \alpha)$$
<div align="right">*Equation 5.13*</div>

The algorithm was based on hundreds of hours of number crunching to create a look up table covering the regions of the interest for radar modelling. The table was stored as a series of surfaces described by polynomial coefficients to reduce storage space, reduce look up time and facilitate interpolation between the simulated grid points. NEMESiS was coded to calculate the required input parameters for the threshold algorithm and extract a threshold for each range cell in the simulation. The threshold was then used to build probability of detection maps for the target required by the user.

5.5.3 False alarm rate modelling

This threshold code was also used to create a new radar performance output which aimed to show possible false alarm rates in a radar system. If the assumption is made that a radar system has been designed to use a constant TNR in its CFAR processing then the CFAR will begin to fail in regions of spiky clutter. The threshold algorithm can be inverted to estimate the actual false alarm rate generated in a given scenario. An example of the inversion to give the false alarm rate from a CFAR set up to work in noise for different clutter powers (CNR) and spikiness (v) is shown in Figure 5-9. High false alarm rates (red areas) are shown for spiky clutter with high a CNR.
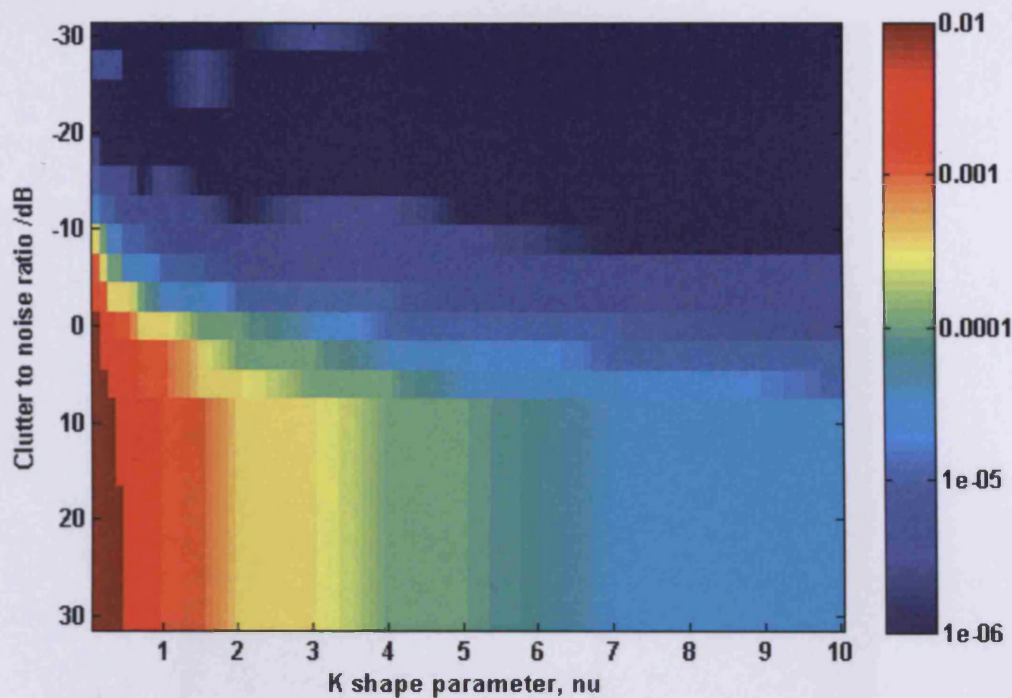
Figure 5-9 Single pulse clutter false alarm rate for a radar system using a standard noise threshold inverted from the UCL threshold algorithm

5.5.4 Range dependent multiple waveform definitions

Many aspects of radar performance are radar system specific and aren't limited just by the fundamental physics of a scenario. For example, surveillance radar will use different waveforms to look at different ranges. Often high pulse repetition frequency (PRF), short range, Doppler bursts are used close to the radar whereas low PRF single pulses might be used for longer ranges. These regions will have different levels of clutter cancellation and are susceptible to different clutter effects.
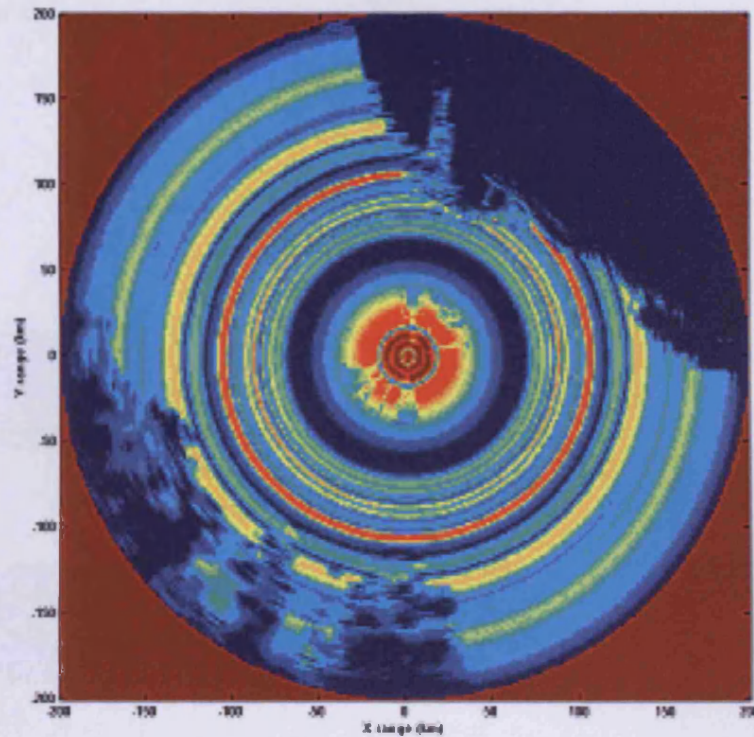
Figure 5-10 PPI view of probability of detection in a littoral scenario showing the effects of the range and azimuth dependent processing model

NEMESiS functionality was modified to allow range-azimuth sectors to be defined in which different pulse compression, PRF, and processing gains would be applied by the radar model wrapper. This functionality is demonstrated by Figure 5-10, which shows that in this scenario the performance close to the radar is improved by a short range waveform which provides good clutter processing but the improvement is strongly azimuth dependent due to multiple time around effects caused by the high PRF. At longer ranges the azimuth dependent effects are reduced but range dependent effects of anaprop clutter are visible.

5.6   User interface
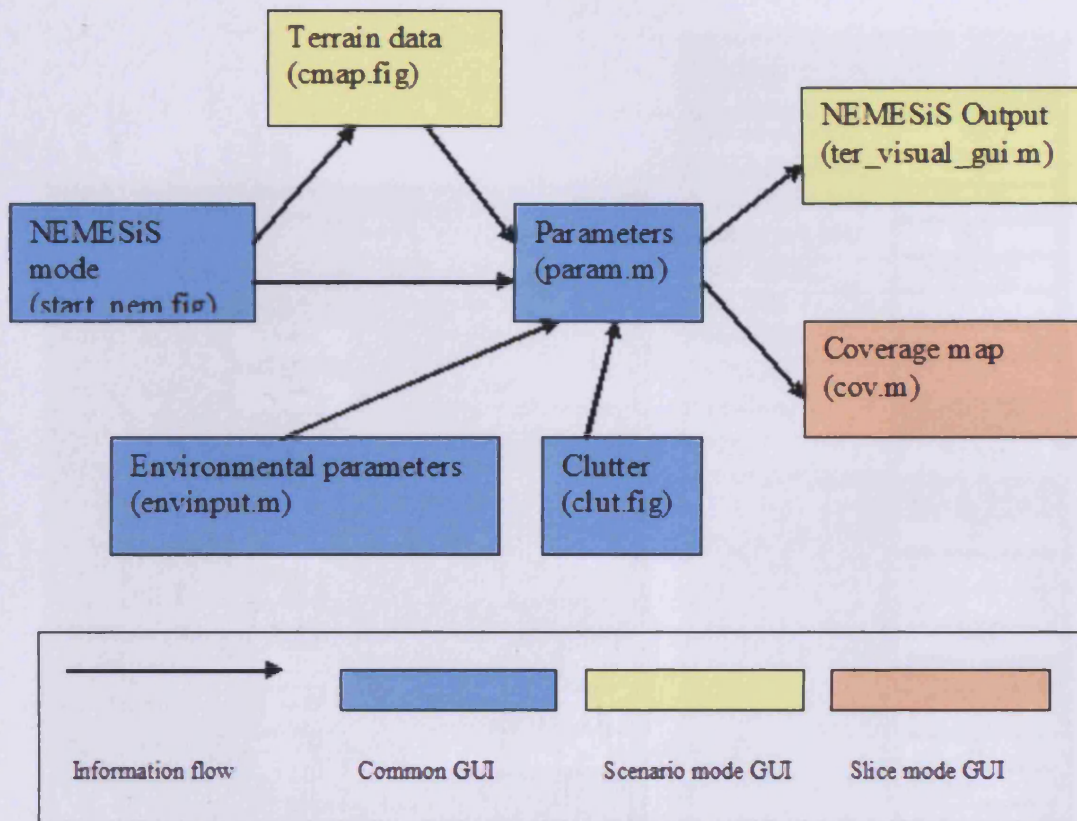
Figure 5-11 A number of GUIs control the use of NEMESiS

To make NEMESiS simple to use, a series of graphical user interfaces (GUIs), shown in Figure 5-11, were designed to allow the user to create scenarios rapidly, run the propagation program, and then interactively examine the results (two of the input GUIs are shown in Figure 5-12).

Firstly, an initial GUI allowed the user to define the type of modelling. If a simple slice or 2D model was required then a pre-calculated text terrain file was read in. If scenario or 3D modelling was specified, user inputs were used to define the geographical region to be modelled. The appropriate terrain data was then extracted from Digital Terrain Elevation Database (DTED) files in azimuthal

slices using a great circle rapid grid search algorithm developed specially for NEMESiS.
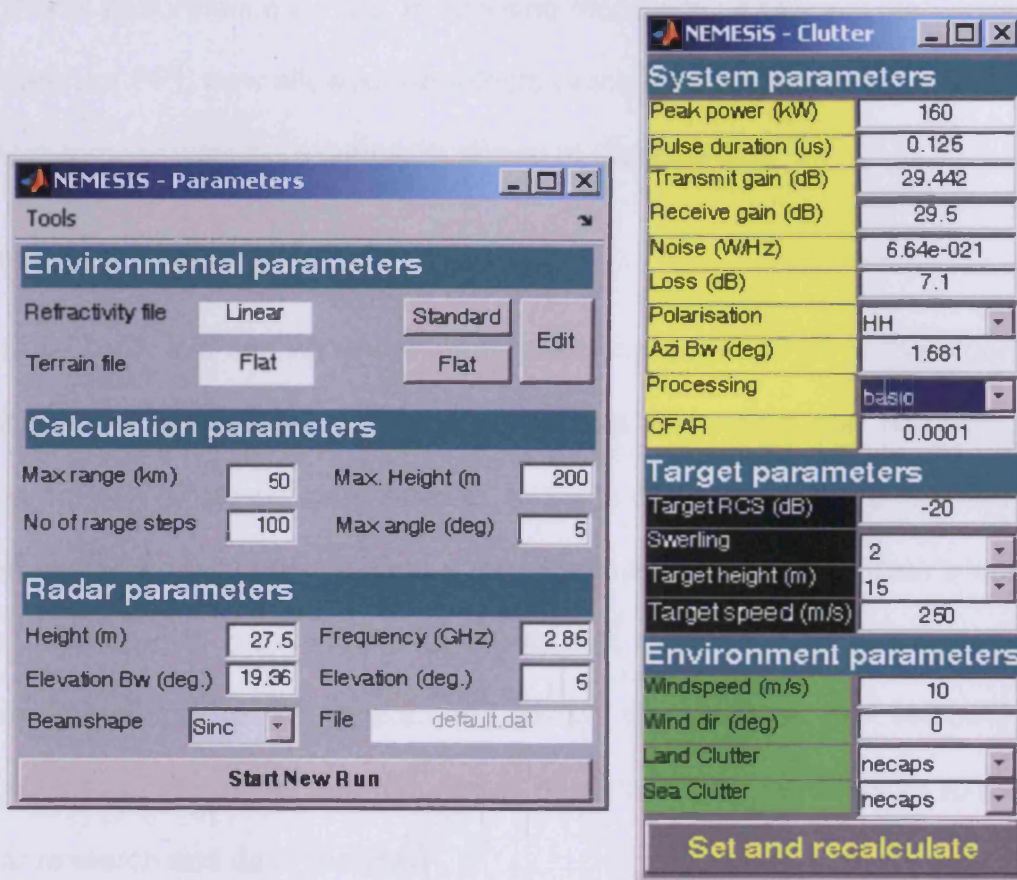
Figure 5-12 Input GUIs for NEMESiS

2D or 3D Refractivity data was then read in from a user defined file. The propagation loop was then run once for slice mode or, when in scenario mode, many times, using each terrain slice in the defined 3D refractivity environment, to produce 3D propagation data and 2D clutter parametrisation. Another GUI was coded to allow the user to define further scenario parameters that took the raw model output data and instantly produced a variety of radar performance outputs in different target and weather conditions without having to rerun the propagation model. In slice mode the output GUI showed a range vs height 2D

slice of propagation outputs (shown in many figures in this document such as Figure 5-4) which could be interrogated using the mouse cursor to produce traditional performance curves. In scenario mode a 2D traditional plan positional indicator, or PPI, view allowed the effects of the environment to be visualised in a more familiar way (an example is shown in Figure 5-23).

5.7 Results

The results in this section show many plots that combine all of the algorithms described in this chapter to demonstrate that the model can create a wide variety of scenarios and radar outputs. In some of these cases the outputs have been used to validate the model by visual comparison with real data which has been facilitated by creating simulated data sets for matching to the real data. In other cases the results presented merely demonstrate the flexibility and capabilities of the model and the variety of outputs that can be used to support radar research and data analysis.

5.7.1 Radar wrapper simple comparison

The basic performance of the model was assessed by comparison with a spreadsheet radar equation model of the power levels returned for a given target in the switch matrix of an operational RN radar. NEMESiS was run using a 'flat earth' constant refractivity profile to match with the spreadsheet model. Figure 5-13 shows that NEMESiS follows the correct roll off with range. The multipath peaks are 11-12dBs above freespace propagation modelled in the spreadsheet, this corresponds to a factor of 16 that one would expect due to

multipath (4 propagation paths between the radar and the target and so 2^4 times as much power would be received).
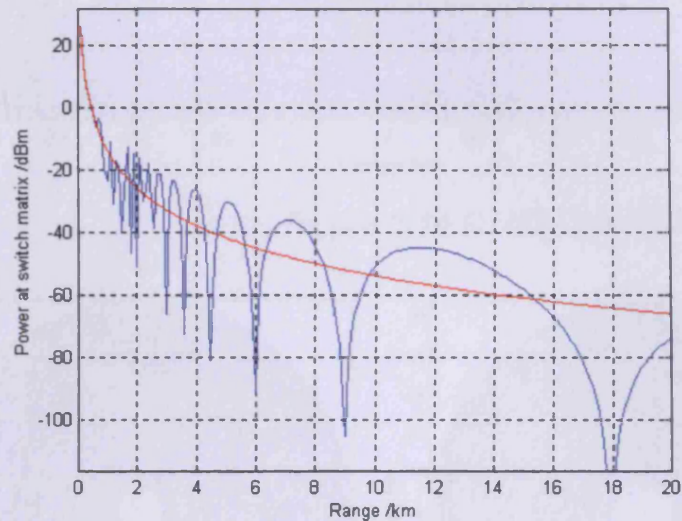
Figure 5-13 Comparison of received power (at the switch matrix which is an important measurement point in certain radar systems) for NEMESiS (blue line) and a radar equation based model (red line)

5.7.2 Portland example

Figure 5-14, Figure 5-15 and Figure 5-16 show an example scenario which uses DTED data of Portland Bill (Figure 5-14) along with a 20 metre evaporation duct profile to model radar performance for a shipborne radar used in the radar trials in chapter 4. The modelled clutter RCS shown as a PPI in Figure 5-15 matches to the trials data but a direct visual comparison is much more effective using the simulated data as shown in Figure 5-16 (further analysis of this scenario is described in section 6.1).
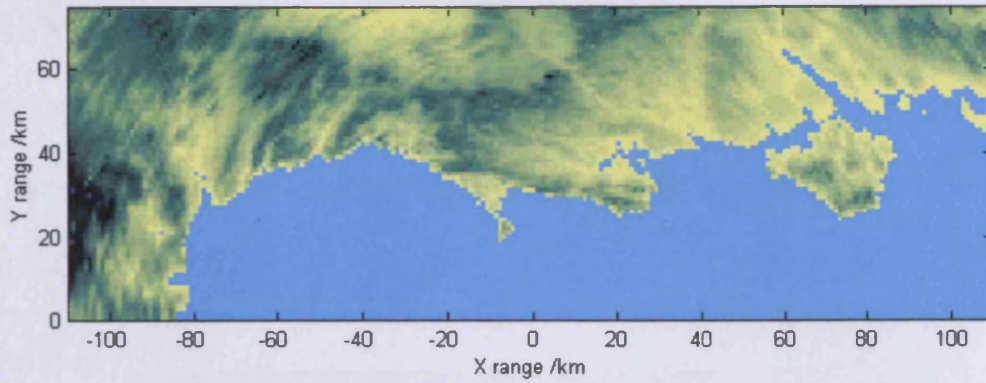
Figure 5-14 DTED Data showing Portland Bill
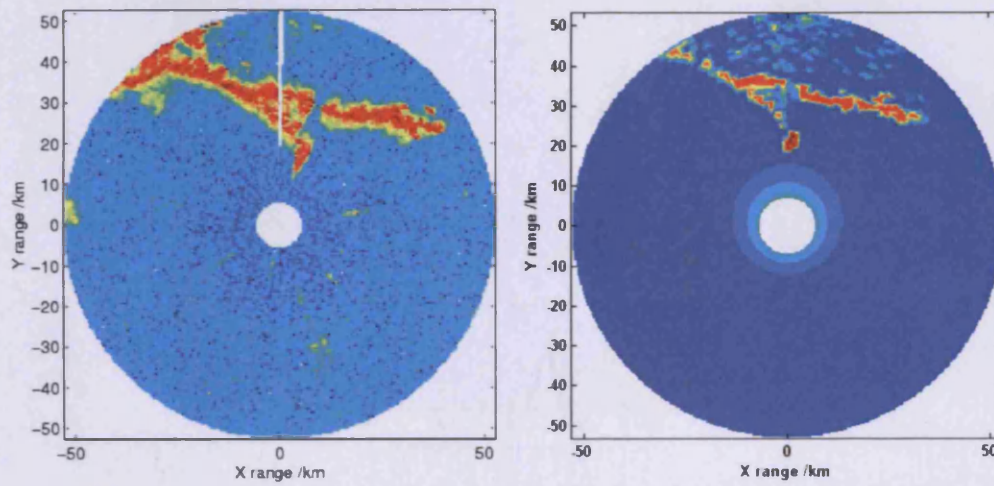
Figure 5-15 Comparison of recorded PPI scan (left) with modelled mean
clutter RCS (right)
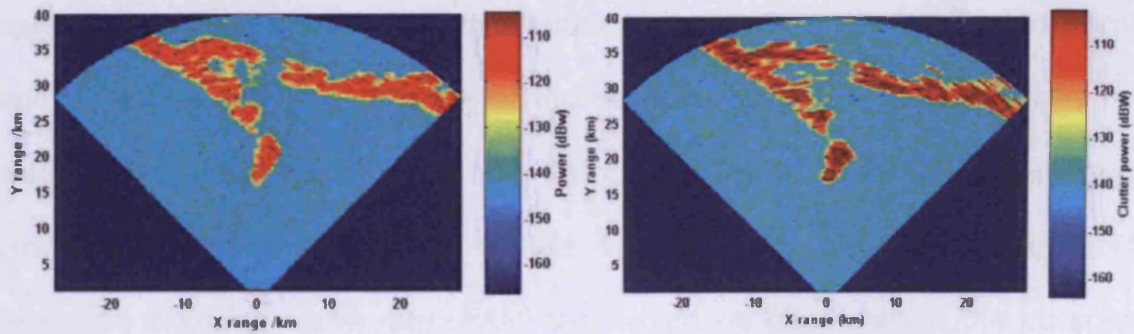
Figure 5-16 Comparison of recorded data (left) with simulated data that
includes statistical variations (right)

5.7.3 False alarm rate

NEMESiS's false alarm rate model was discussed in section 5.5.3. The model was assessed using a littoral scenario created in the Straits of Hormuz as shown in Figure 5-17.
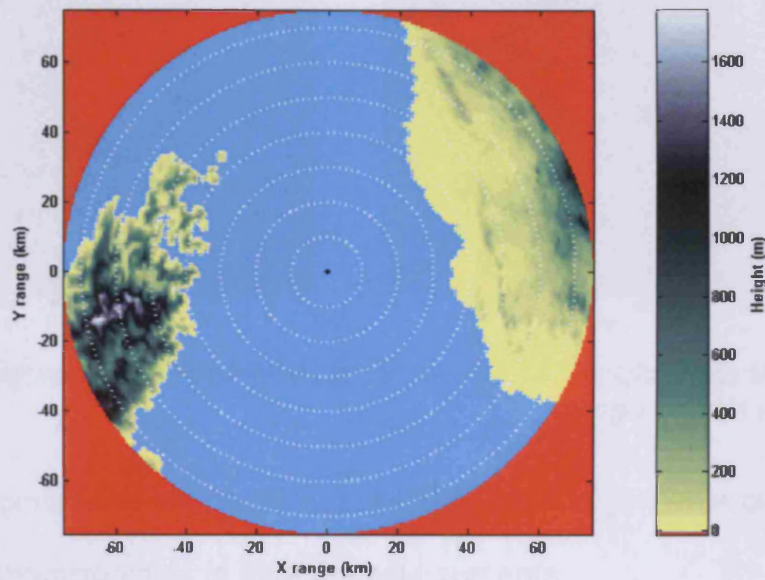
Figure 5-17 Straits of Hormuz littoral scenario

A standard atmosphere was assumed and a radar system was modelled that used an interleaved two waveform system with a short range MTI (out to 30km) and a long range NR. The radar system was assumed to use a threshold that would give a CFAR of 10^{-6} when detecting targets in system noise only. However when the NECAPS models for spikiness were used NEMESiS modelled the false alarm rate (FAR) that would be generated in this complex scenario as shown in Figure 5-18. In the left hand plot the orange disc around the ship indicates a high level of false alarms due to sea clutter. In the right hand plot the FAR is reduced by the clutter processing although the effects of

second time around returns to the west and east of the ship are visible. These green coloured regions would have a slightly higher than optimal FAR. In both plots the FAR rate is high over land due to spiky clutter effects.
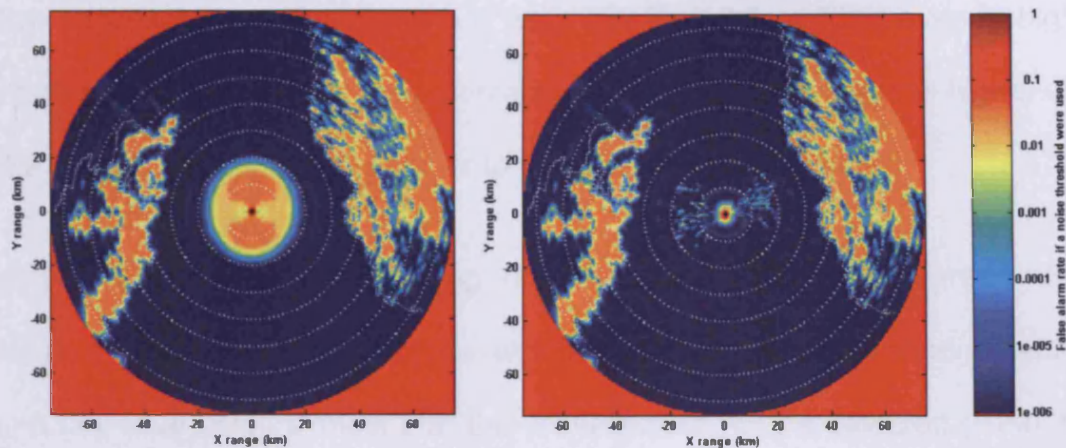
Figure 5-18 FAR for NR (left) and NR/MTI (right) note the ambiguous range effects in the MTI plot

These FAR plots have also been successfully used to generate plot streams for testing tracking algorithms in different environments.

5.8 Coastal vessel tracking radar results

One the applications of NEMESiS is for coastal radar positioning. To examine this kind of scenario NEMESiS was used to analyse a variety of commercial navigation radar. Easy to understand plan position indicator (PPI) views of where given objects (of a specified size and height) would be detectable by the radar system were created. These plots showed areas were coverage is limited (by range and terrain shadowing) and so could be used to assess how the radar might be repositioned to best advantage.

5.8.1 Radar performance outputs

The most useful metric for assessing radar performance is probability of detection (P_d). When using a real radar's PPI display the human eye can often follow successive target plots with a fairly low P_d (~0.5 or 50%) even in highly cluttered conditions, however automatic tracking systems require higher P_ds (>0.9 or 90%) and much less clutter to track targets successfully.

The NEMESiS scenario modelling results below show P_d PPI maps. Red colours indicate areas where you would expect to achieve good detection (P_d>0.75). Blue colours show that the vessel would not be detected (P_d<0.25). This would be either due to sea clutter, terrain obscuration, or a fundamental lack of radar performance.

5.8.2 Scenario

All results were modelled with a wind speed of 5ms^{-1} (sea state 2). Two targets were modelled; a 10m^2 RCS at a height of 3 metres above sea level, and a 1m^2 RCS at a height of one metre above sea level. Values assumed for the modelling were a CFAR level of 10^{-6}, a noise level of -195dBW/Hz and the number of incoherently integrated pulses was 8.

Two radars were compared. The main antenna used was an Easat[9] antenna which used a transmitter with a peak power of 35kW; the frequency used for the plots was 9250MHz and an antenna gain of 44.5dBi. The second antenna used was a low gain navigation antenna which transmitted at a lower peak power of

---

[9]Easat is a radar system company that specialises in high gain antennas for coastal surveillance

25kW, a frequency of 9375MHz and an antenna gain of 33dBi and a different beam shape with higher sidelobes than the EASAT antenna. All antenna heights are given above mean sea level (zero metres). A nominal value of 1dB was used for system losses. The radar systems were positioned on the top of Portsdown Hill on the Portsdown Technology Park site.

5.8.3 Modelling results

The plot below shows P_d over the sea (performance over land isn't relevant for a maritime navigation radar). The land height has also been included to provide more information about the scenario and help when comparing to other PPI views of different performance parameters.

Combined plot showing probability of detection for a 10 m² target and terrain height (m)
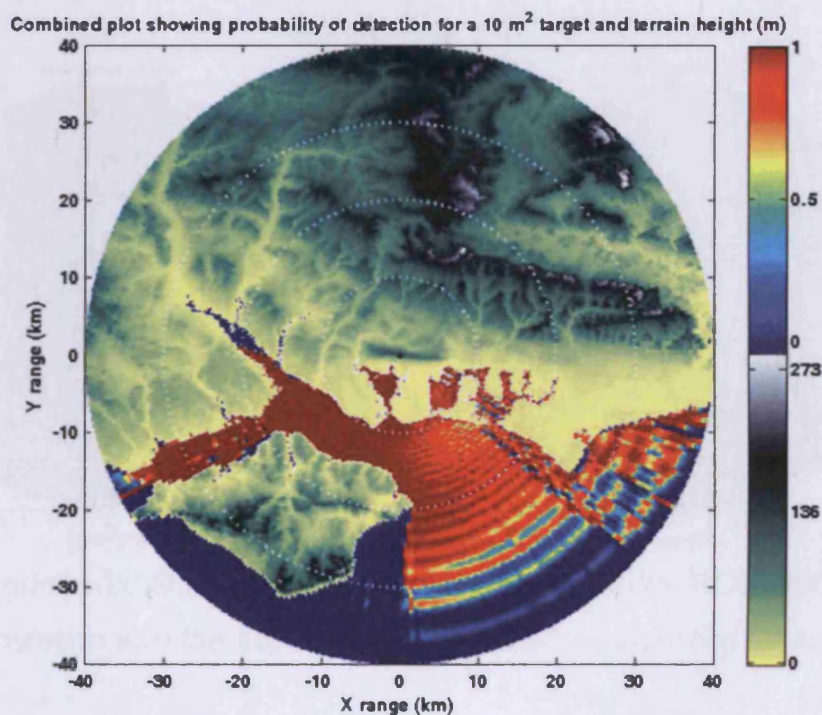
Figure 5-19 Probability of detection (P_d) plot (with land overlay)

Figure 5-19 shows excellent detection (red coloured regions) of a ship with an RCS of 10m² (equivalent to a medium sized fishing boat) in the Solent, with gaps at longer ranges due to multipath effects. Coverage is patchier to the east of Selsey Bill suggesting a second radar would be needed to provide good detection in this region.

The plots below (Figure 5-20) show simulations of the clutter power, against a background of system noise, that would be seen by the radar. In the right hand plot NEMESiS has used clutter models to describe the statistics of the clutter and then used the clutter distributions to apply appropriate variation to the generated scene. The land coastline is marked with a white line and range rings are marked at 10 km intervals.
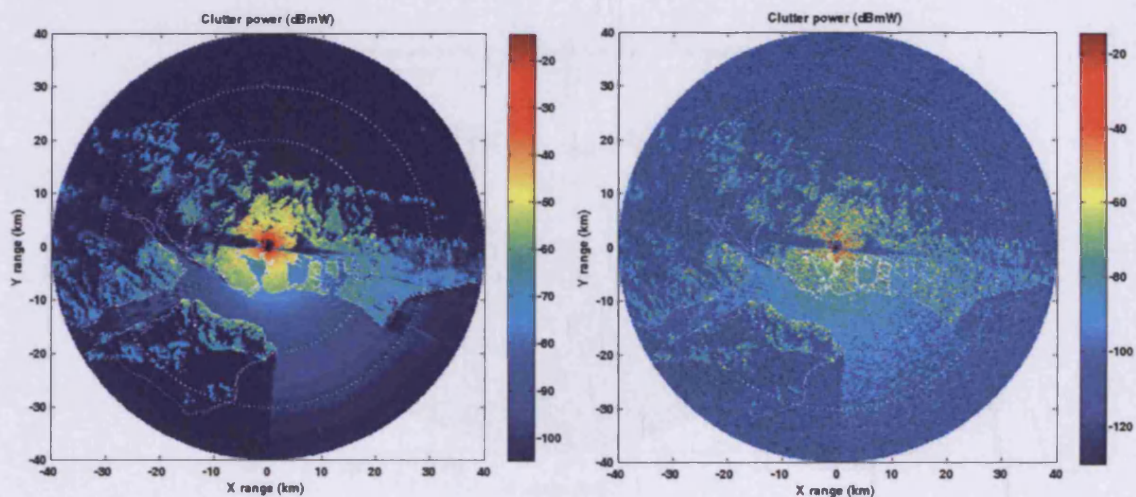
Figure 5-20 Simulated PPIs showing mean clutter RCS (left) and radar simulation with the appropriate non-Gaussian statistics for land and sea clutter (right)

The plot below (Figure 5-21) shows a zoomed in region of the clutter simulation with a terrain overlay.

Combined plot showing clutter power (dBmW) and terrain height (m)
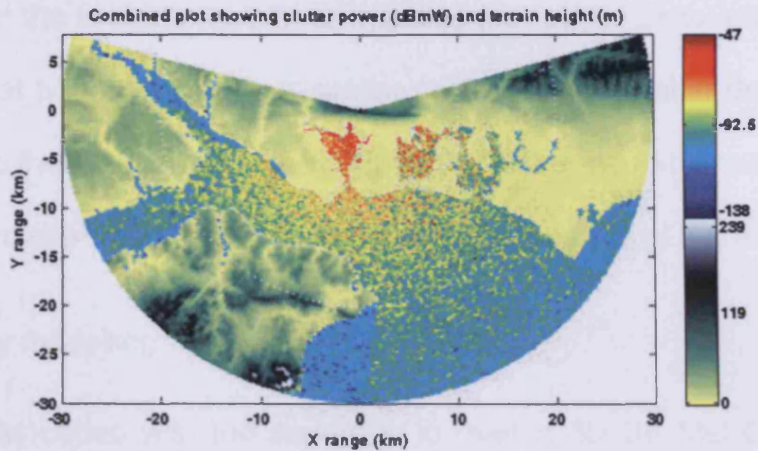
Figure 5-21 Zoomed in simulated sea clutter with terrain overlay

Figure 5-22 shows P_d (in dB) for a small craft with an RCS of $1m^2$ (equivalent to a RIB or a jet ski). The P_d is different to Figure 5-19 because of the smaller target extent in height and the reduced RCS, which leads to reduction in P_d in the 12-15 km range band as shown by the blue ring.

Combined plot showing probability of detection for a 1 m^2 target and terrain height (m)
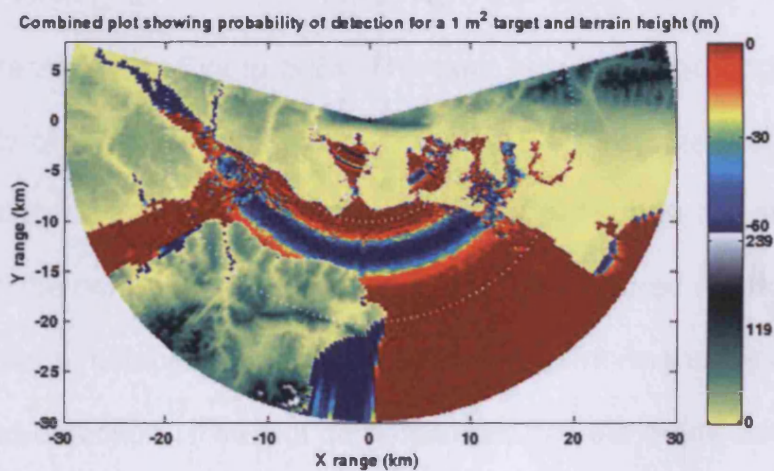
Figure 5-22 Zoomed in P_d plot (P_d shown in dB) with terrain overlay

The results show the capabilities of the NEMESiS model to create detailed simulations radar systems and shows how complex performance data can be presented in a simplified form by using a familiar PPI plot format. NEMESiS was

able to model the two different radar systems (not all the plots are shown here) and show that both systems had similar performance for ship detection in the Solent due to the geography of the region (the higher performance radar turned out to only provide limited extra benefit due to the position of the Isle of Wight).

5.8.4 3D refractivity modelling

NEMESiS was coded with the capability to read in 3D UK Met Office forecast model data. An example set of 3D meteorological data was provided by the UK Met Office from their high resolution forecast model[10] of the Persian Gulf region. The forecast data was thought to contain significant ducting features which are common in that area. This data was converted into modified refractivity and resampled to create a radar model for a ship radar in the Persian Gulf, 20 miles SE of Basra, looking for extremely small RCS low flying targets. The results of this model are shown in Figure 5-23. The dark blue areas at longer ranges of the probability of detection plot shown in Figure 5-23 indicate that there would be no detection performance over the land that surrounds the ship from the west, through the north, and round to the East. The coloured areas surrounding the ship show a complex pattern of detection performance (red colouring indicates good detection). The plot demonstrates that the model can handle the simulation of a very complicated refractivity scenario and that the PPI plot can give an excellent impression of the radar performance. There is no set of radar data to compare with the modelled results for this case but the model indicates

---

[10]The high resolution model is used by the UK Met Office to provide high quality forecasts for important operational areas

the highly range and azimuth dependent nature of radar performance in a realistic 3D scenario.
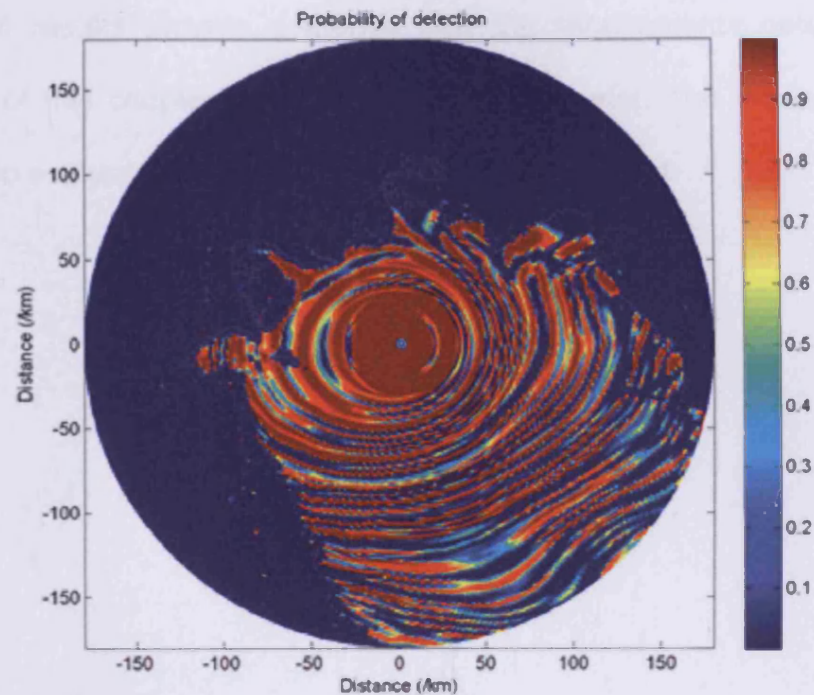
Figure 5-23 Probability of detection for a ship radar stationed SE of Basra

5.9   Conclusions

The results show a variety of outputs from an easy to use mature radar model. Unfortunately it would be prohibitively expensive to collect a fully instrumented set of radar data to quantitatively validate such a complicated model and so quantitative validation has only been possible against other models. Less convincing qualitative validation against real data has been possible and the simulated model results visually matched to real data providing some confidence in the accuracy of the model. Further validation evidence has been

provided by the analysis in chapters 6 and 7 which also match the model to observed phenomena.

The model results provide evidence that the requirements detailed at the beginning of this chapter have been successfully met. The model is used in chapter 6 to analyse the radar data described in chapter 4.

6 Analysis of Trials Data

This chapter examines the trials data described in chapter 4 using the NEMESiS model wherever possible. This analysis highlights various significant anaprop phenomena and their effects on military radar systems.

6.1 Portland Bill evaporation duct
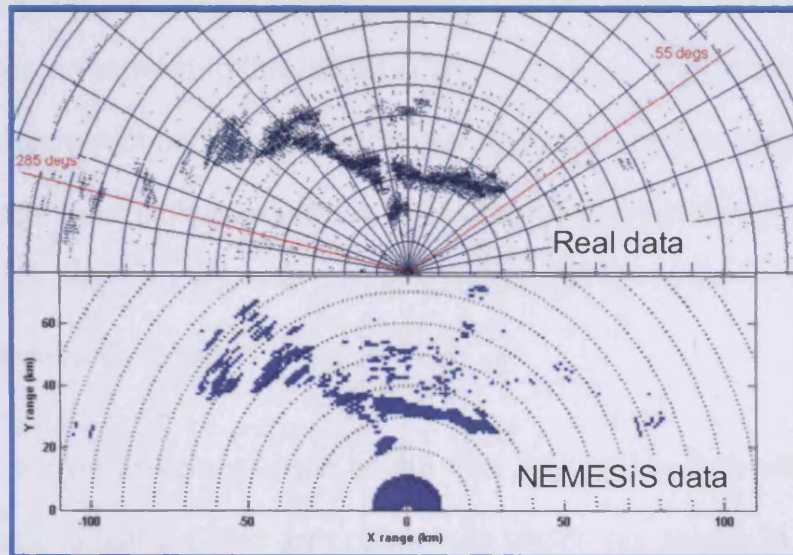
Figure 6-1 Clutter levels in a standard atmosphere
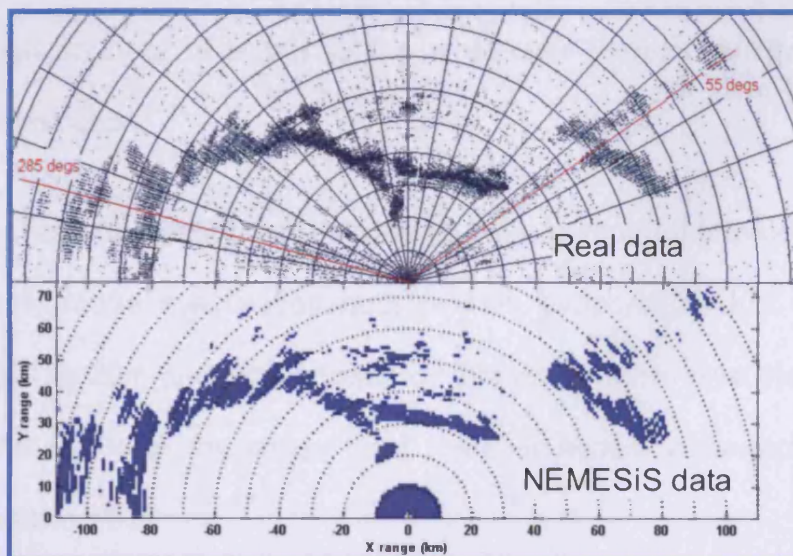
Figure 6-2 Higher clutter levels due to evaporation duct

Figure 6-1 & Figure 6-2 show PPI plots (with range rings spaced at 10 km and azimuth spokes every 10°) that compare thresholded trials data (top of both figures) and NEMESiS modelling plots of thresholded returned power (bottom of figures) for a radar on board a ship situated south of Portland Bill. Land clutter returns from Portland and the south coast of England are shown in dark blue. The two sets of real data were taken only one day apart from similar radar positions and yet the second set shows much more of the coastline all the way from Exmoor in the west to the Isle of Wight in the east. It was theorised that a low evaporation duct might have increased the radar horizon range and led to the increased land clutter levels. To test this theory NEMESiS was used to model the scenario (using the terrain data shown in Figure 5-14) with two different refractivity profiles.

Figure 6-1 shows the comparison of the first day's trials data with NEMESiS modelled results using a standard refractivity profile (as shown in Figure 2-7). Visually the size and position of the land clutter in the two PPI displays matches well although an area of clutter to the west over Exmoor isn't visible in the NEMESiS simulation.

Figure 6-2 shows the second day's data (on top) compared to modelled results with a twenty metre evaporation duct (a 15m evaporation duct is shown in Figure 2-7). The 20m duct was chosen by trial and error to give the best match between the trial and the model and there is almost a perfect correlation between the two PPIs.

The quality of the matches between the real and simulated data supported the evaporation duct hypothesis and allowed the size of the duct to be estimated.

6.2   Surface based duct
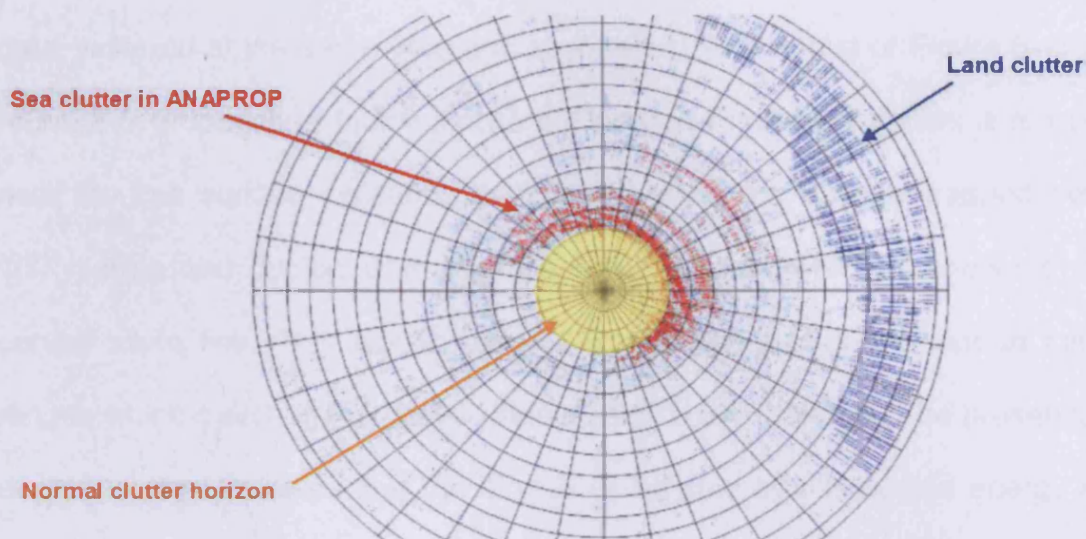
Figure 6-3 Cluttered PPI plot due to a surface based duct

NEMESiS was also used to analyse the anomalous clutter returns shown in Figure 6-3 which were visible during strongly ducting conditions whilst sailing in the Red Sea. The radar data recorded showed areas of increased sea clutter, shown in red, well over the normal radar horizon, indicated by the yellow disc, and very high levels of land clutter, highlighted in blue, from very long ranges leading to a highly confusing situation for the radar system to process. To maintain low false alarm rates in such difficult conditions, local detection thresholds would have been automatically raised, and this led to blank areas appearing on operator PPI displays where no false alarms were visible. False alarms should be visible in raw radar video output and although unwelcome they serve to indicate that the radar is operating with maximum sensitivity. Therefore the blank regions actually implied that there was likely to have been a

loss of detection sensitivity in the radar system that was being caused by the anaprop conditions.

NEMESiS was used to model this situation using radiosonde derived refractivity data gathered at the same time and is shown in the left plot of Figure 6-4. The NEMESiS propagation factor plot to the right of Figure 6-4 shows a red area near the sea surface indicating that energy would be strongly trapped below 100 metres and ducted well past the radar horizon, which is shown by the curved white line. This would suggest higher levels of sea clutter at longer ranges which matches the clutter effects seen in the real data. The presence of ducted energy indicates that the land is illuminated by this ducted energy and so would give strong land clutter returns which again matches the phenomena in the recorded data. The NEMESiS simulation also shows 'focussing' of energy (shown by a greater concentration of red) onto the sea surface at around the 30, 55, and 80 km range which would have led to the rings of sea clutter returns around the ship visible in Figure 6-3.
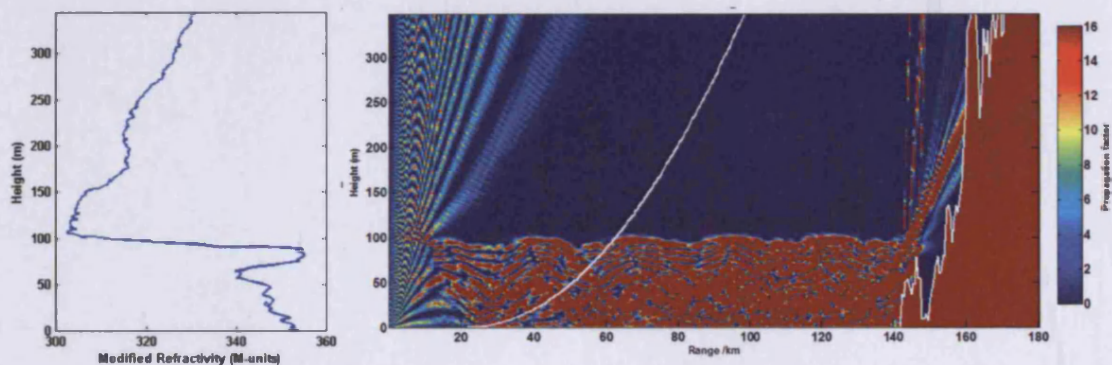
Figure 6-4 NEMESiS model (right) of radar propagation in a strong duct (M-profile shown at left)

Figure 6-5 shows a comparison of a single azimuth slice of the real PPI data from Figure 6-3 (through the region of enhanced sea cutter) with a slice of sea clutter simulated by an early version of NEMESiS. The data being compared is clutter return power as a function of range. Although the correlation between the two plots is not one to one, the comparison shows that the ranges and intensity of the major groupings of predicted sea clutter returns visually matched the observed data.
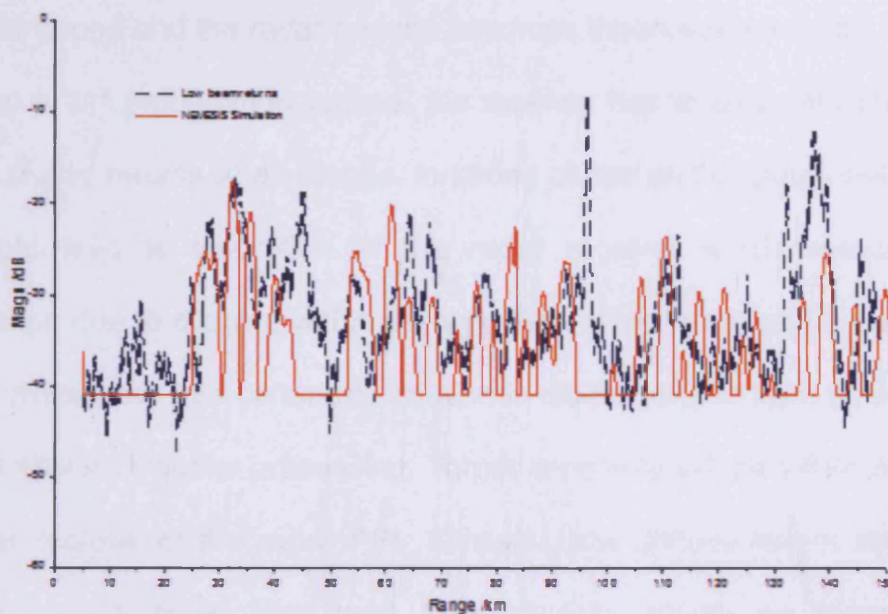
Figure 6-5 Comparison of radar clutter returns with NEMESiS simulated clutter

The NEMESiS results have helped to confirm that the refractivity profile measured during this trial which suggested anaprop conditions does indeed account for the clutter phenomena visible in the radar data gathered at the same time.

6.3 Radar horizon and saturation

The results and modelling detailed in sections 6.1 and 6.2 both examine one of the most important effects of anaprop which is to change the range to the radar horizon, which for a shipborne antenna at a height of 30 metres is around 23 kilometres in standard atmospheric conditions. In super-refracting conditions, the horizon range is increased giving surface clutter at increased ranges and enhanced low altitude target detection. In a deep evaporation duct, radio waves become trapped and the radar horizon becomes theoretically infinite. Due to the switch to a $1/r^2$ propagation regime, the receiver has to deal with much larger surface clutter returns at all ranges. In strong clutter and ducting environments, this could lead to saturation of the radar receiver which reduces clutter cancellation due to clipping within the amplifiers used in the radar system. This clipping masks the true coherent variation in clutter returns from pulse to pulse which is vital for Doppler processing. Target sensitivity will therefore be reduced in clutter regions of the radar PPI. Similarly, low altitude target strength will increase, which could also lead to saturation effects on target velocity estimation. Pulse compression efficiency will also be reduced because clipped returns don't match the transmitted pulse shape so well leading to reduced compression gain and loss of SNR. Another type of saturation effect, interference between radar receiver channels, is described in the next section.

6.4 Ambiguous range and clutter folding

6.4.1 Receiver channel breakthrough

Figure 6-6 shows a section of a PPI from another set of data from the Red Sea. As usual the azimuth spokes are every 10° and the range rings are every 10 km centred at the radar which is just off the top right of the zoomed section. The important clutter returns have been highlighted in red using a graphics package to make them more obvious. The land clutter region (the red area at the far left of the picture) at 150km range is repeated in three places at closer ranges to the radar (the repetitions are visible at around 100, 80, and 55 km range).
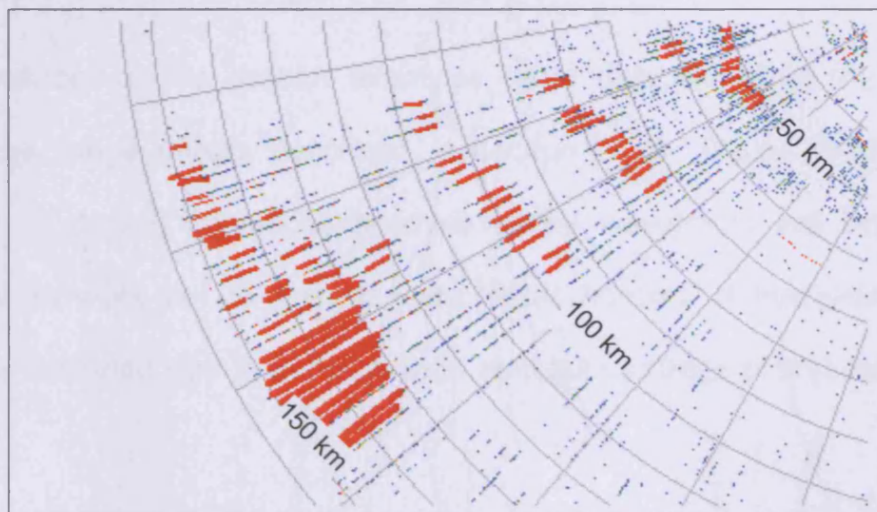
Figure 6-6 Clutter folding causes the close in repetition of signals

Figure 6-6 shows evidence of clutter folding. The presence of a strong duct has caused the land clutter returns from 150 km away, which would normally be below the radar horizon, to saturate the radar receiver. In this case the repeated clutter signature is caused by the interference between two of the radar system's waveforms. The pulses of the short range high PRF waveform are

transmitted about 30 km apart. The maximum range for this waveform is therefore 30 km. However, the returns from these pulses are so strong that they have broken through into the receive period of the next waveform which has a much longer range and lower PRF. The spurious interference returns show up as a repeating copy of the land clutter.

This effect is slightly different from the one described in section 2.8.5 as in this case the clutter is far enough away (beyond $R_{max}.n_p$ see section 2.8.5) that the performance of the short range MTI waveform has not been affected.

6.4.2 Burst waveform clutter folding

The remainder of this section examines radar data exhibiting the standard ambiguous range effects described in section 2.8.5. These affects will be common in ducting conditions because clutter waveforms are usually only designed to work out to the standard radar horizon. If the radar horizon becomes extended due to anaprop then ambiguous range effects are likely to occur.

Run 0240 Beam 1 Ch. 1 normal radar
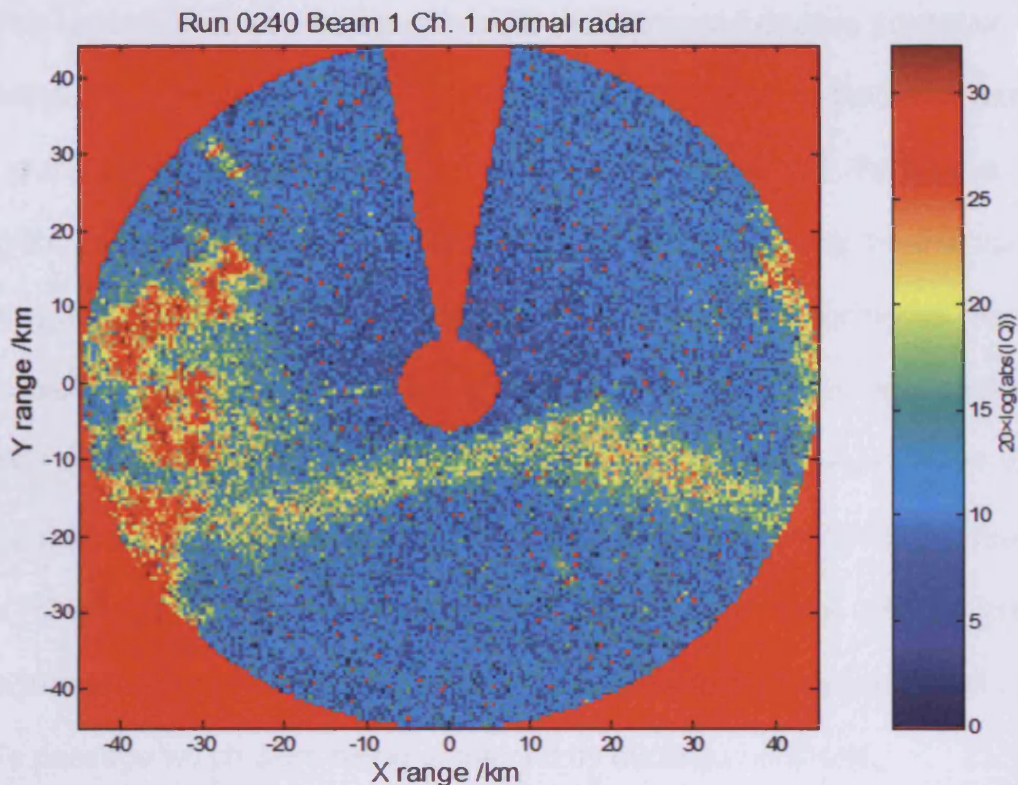
Figure 6-7 Data from the Middle East showing a feature caused by anaprop conditions

During HMS Richmond's passage towards the Persian Gulf an interesting data set, shown on the PPI in Figure 6-7, was recorded. The figure shows the clutter power recorded from the radar according to the colour scale on the right of the plot. An area of clutter, shown by the arc of yellow and orange returns on the plot, showed up over the sea to the South of the ship in the late evening, when ducting conditions were found to be most common, between two areas of land clutter, the intense regions of red clutter to the east (just visible) and the west. The phenomenon followed the ship for tens of nautical miles. There was no immediate explanation for this data although anaprop effects were suspected. NEMESiS was used during the trial to show that this was a possibility.

Further analysis involved using a number of terrain and ducting scenarios with 3D NEMESiS to create a video of a simulated passage along the same path as that of the ship. A frame from the video is shown in Figure 6-8. Suitable ducting conditions were chosen from a range of profiles recorded during the trial that led to modelled results that visually matched the radar effects (compare the right hand plot of Figure 6-8 the 4th plot in Figure 6-9). The model also showed a shaped area of clutter that followed the ship to the east and west similar to the one visible in the real data. Examination of the model results confirmed that the trials phenomena were probably caused by second time around (range ambiguous) returns from the steep rocky coastlines to the east and west of the ship's passage which were being enhanced by ducting conditions.
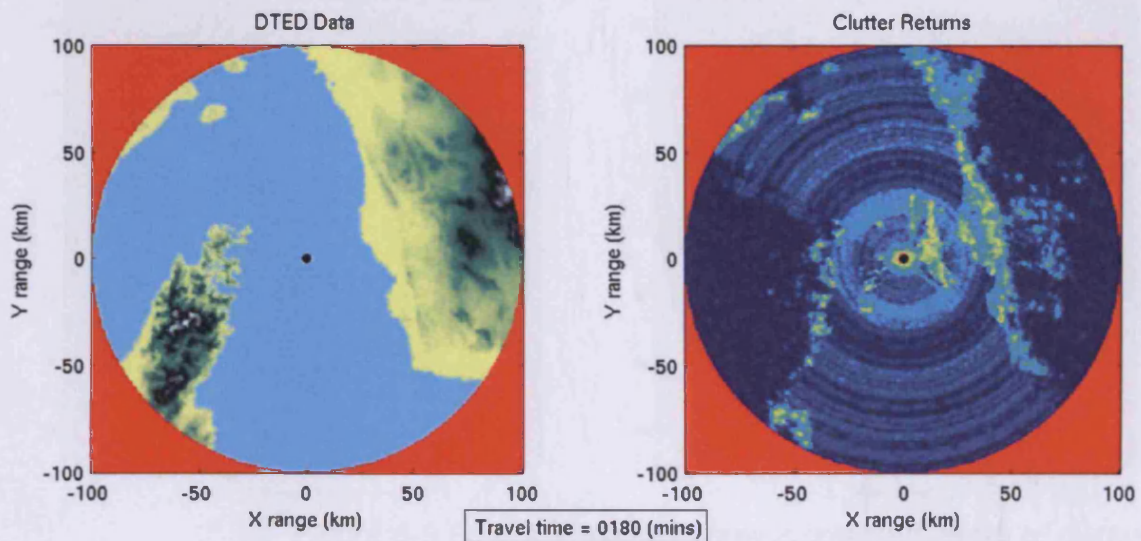
Figure 6-8 Model of passage through the Straits of Hormuz

1.1.1 Exploitation of clutter folding

Once anaprop had been established as the cause of this clutter it could actually be exploited to create a long range clutter map using four short range pulses of

an MTI waveform. The data from each of the pulses are shown in Figure 6-9 starting in the top left with the data from pulse one and progressing right then down to pulse four's data.
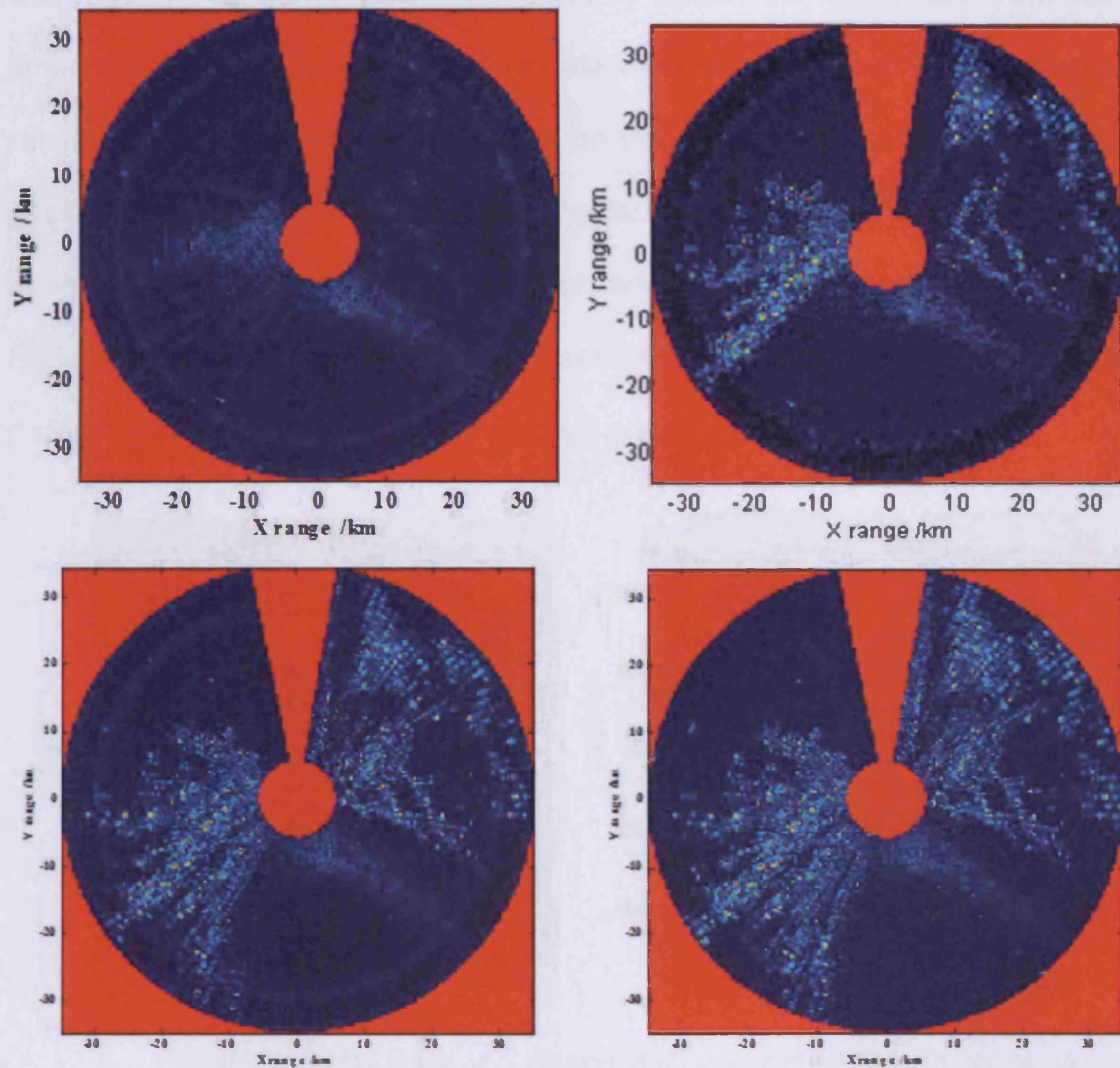
Figure 6-9 Four MTI pulses show increasing levels of clutter

The first pulse data shown in the top left plot represents the short range clutter in a PPI format. Some sea clutter is visible to the west and south-east of the ship shown by the light blue areas. The following pulse in the top right plot contains the same clutter as the first pulse but also clutter from the first range

ambiguity as described in section 2.8.5. By subtracting the data in the first pulse from the second pulse the short range clutter from the unambiguous range is removed to leave the clutter in the first ambiguity (R_{max} to $2.R_{max}$). This process was repeated for all the pulses to iteratively extract the clutter data from each ambiguity. The resulting four sets of data were mapped on to the appropriate range and plotted on a PPI as shown on the left of Figure 6-10. The circular gaps in the map are caused by the the lack of data during the transmission period of each pulse. Visual comparison with the clutter returns from the low PRF waveform used for long range detection (right hand of Figure 6-10) makes it clear that this unwrapping technique can create a good long range map.
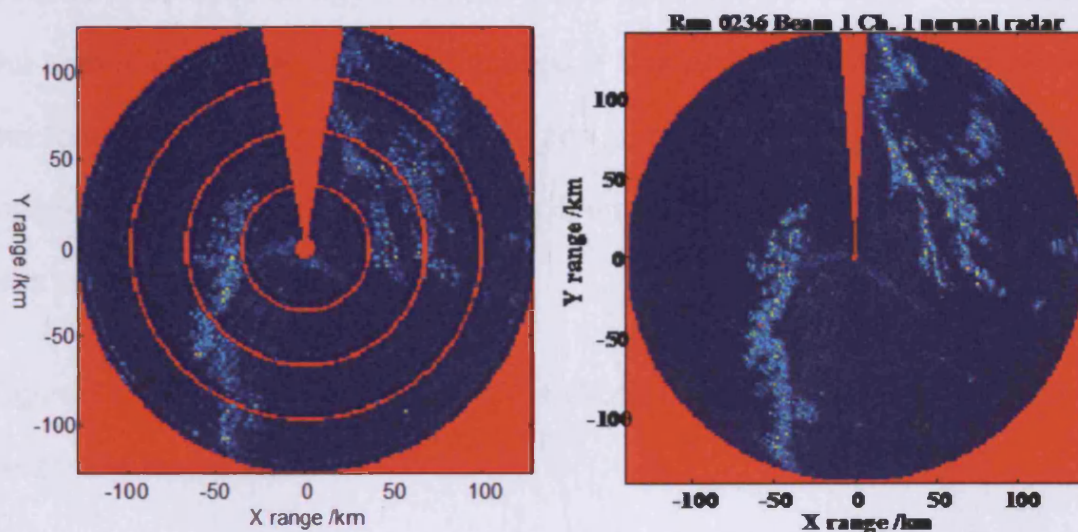
Figure 6-10 Unfolded MTI pulses (left) compared to long range clutter output

This analysis suggests that if a radar could detect the presence of anaprop conditions then it could automatically increase the number of guard pulses to maintain sensitivity. As these guard pulses are usually discarded this would reduce the collected data available for surveillance and still might affect radar

performance. However long range detection could be carried out using the guard pulses. This could allow a flexible radar system to reduce the number of long receive period waveforms and so create more time for short pulse MTI or Doppler waveforms to regain any lost performance.

6.5 Coverage holes

Two of the effects of ducting will lead to a loss of detectability for medium altitude targets. 'Medium' altitude means high enough to be above a duct but low enough to be below the standard radar horizon. Firstly increased surface clutter will make clutter cancellation more difficult within the radar system. Secondly, because energy is trapped in the duct, and the energy released from the antenna must be conserved, there is a loss of energy in the area between the top of the duct and about one degree of elevation from the horizontal. An incoming target could use this radar coverage hole to avoid detection until it was too late to engage it.

Figure 6-11 shows a coverage plot of a strong ducting scenario and a potential radar hole is indicated.
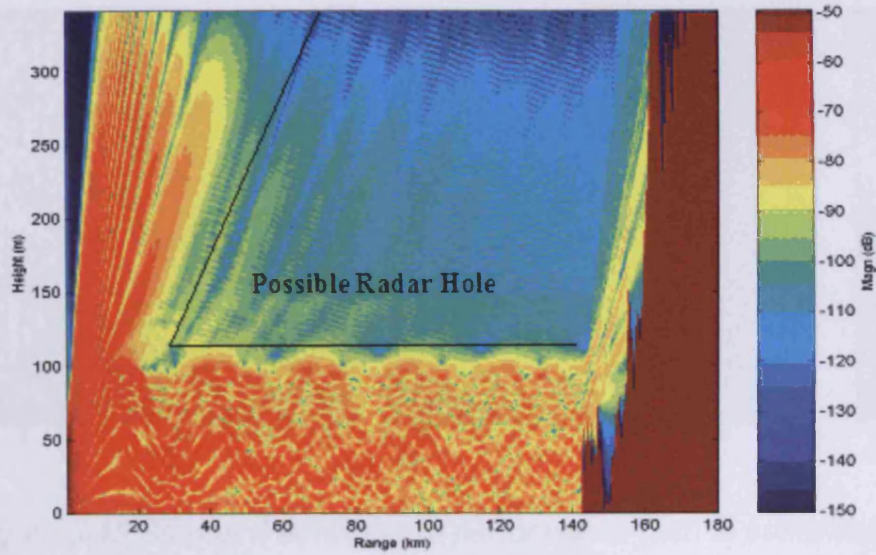
Figure 6-11 Coverage plot showing the radar hole above a strong duct
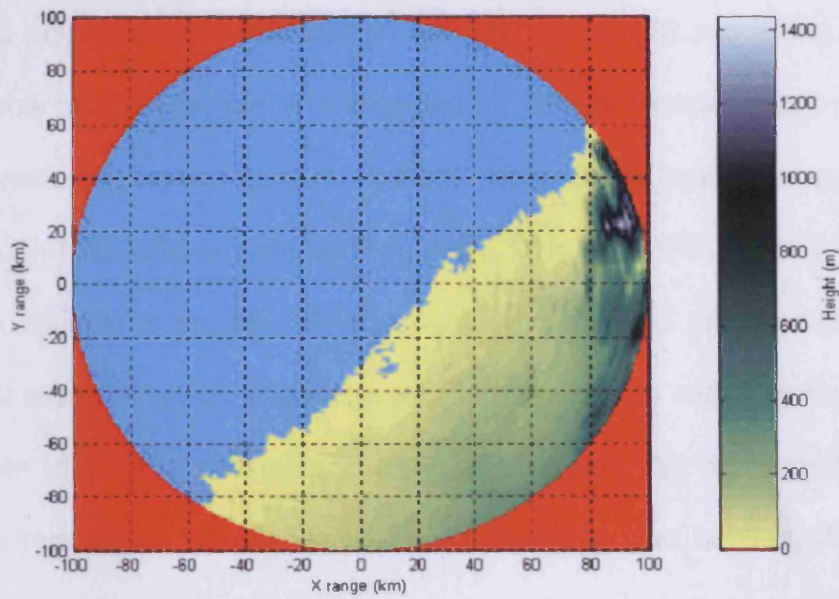
Figure 6-12 Radar hole scenario
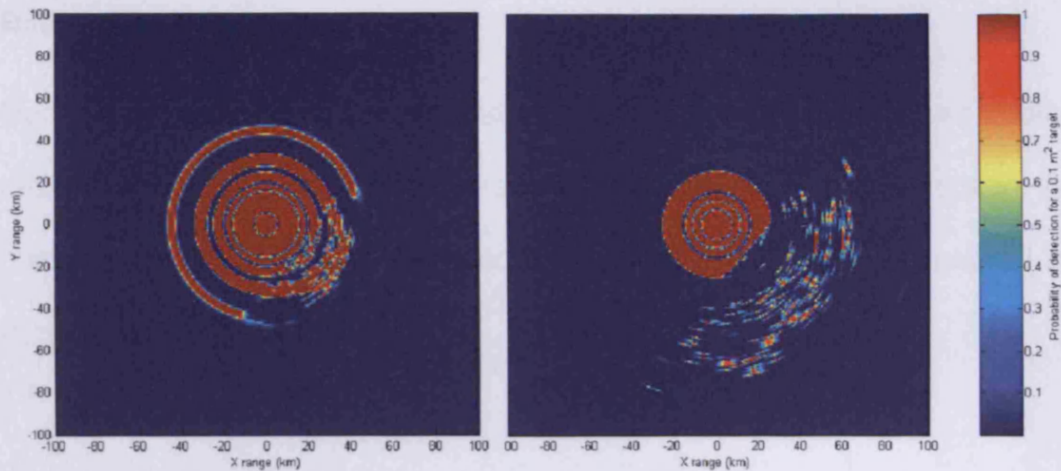
Figure 6-13 Standard atmosphere performance (left) is better than ducting performance in a radar hole (right)

Combining environmental information with 3D NEMESiS modelling has been used to show how performance is changed for targets exploiting this radar hole. In the scenario shown in Figure 6-12 there are areas of land and sea visible to the radar. The NEMESiS plots in Figure 6-13 show P_d PPI plots for standard refractivity conditions on the left and ducting conditions on the right. The P_d plots show areas in which a target would be detected in red. The target height was chosen to be just above the duct used to create the right hand plot. The size of the red region around the radar is reduced in size between the left and the right plot which indicates that performance is reduced especially over the areas of land clutter. If this kind of picture were available in real-time on a ship then measures could be taken to reduce the risk of an attacker using these conditions to their advantage.

6.6 Radar skip

During the ship trials a known surface contact (another RN ship) was spotted on radar at around 95 nautical miles away, well beyond the radar horizon. As the distance reduced the radar contact disappeared and only reappeared at the normal radar horizon.
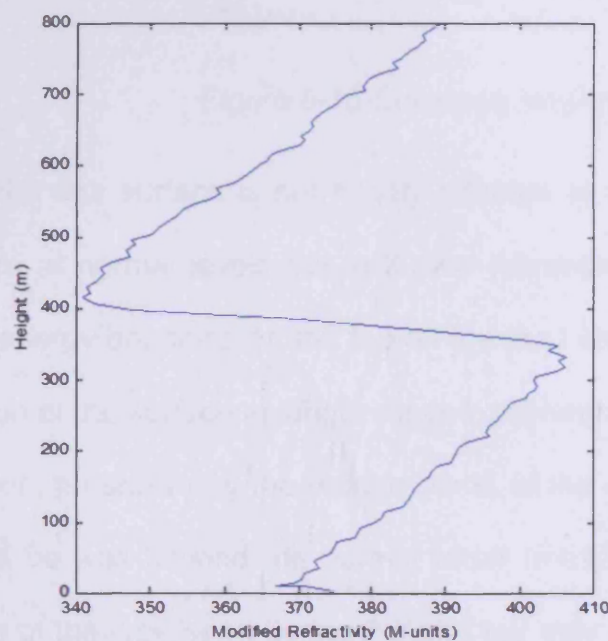
Figure 6-14 Modified refractivity profile showing surface based duct

NEMESiS analysis using a duct profile taken at the time, as shown in Figure 6-14, clearly demonstrates the radar skip phenomenon. A strong ducting layer at altitudes of around 100-400 metres leads to a highly discontinuous surface coverage characterised by the following coverage map (Figure 6-15).
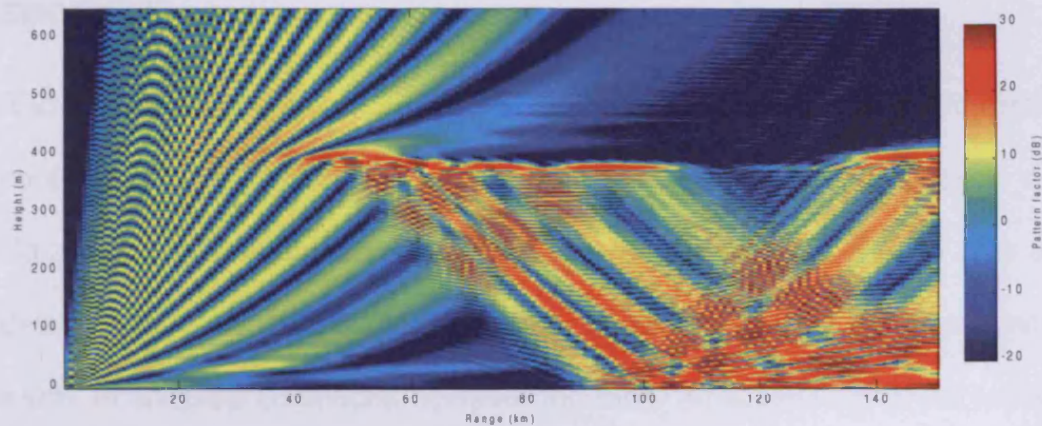
Figure 6-15 Coverage map showing skip effects

The coverage of the sea surface is not hugely affected at close range as the multipath lobes are at normal levels out to 30 km (compare to Figure 2-3 for example) but the energy bouncing off the top off the duct creates another area of good propagation at the surface at longer ranges, between 90km and the end of the plot at 150km, as shown by the orange areas of the coverage plot. This propagation would be well beyond the normal radar horizon and would allow surface detections of the type seen during the trial but may therefore also lead to ambiguous clutter effects close in to the radar.

During radar trials this skip phenomenon was found to confuse both CFAR and tracking algorithms as well as causing a greater workload for radar operators unprepared for anaprop conditions. Despite this, experienced RN personnel used this phenomenon during the trials to detect known surface targets at ranges which would normally be well over the radar horizon.

6.7 EMCON effects

Another application for NEMESiS modelling is electromagnetic emissions control (EMCON). EMCON is an important consideration for ships in a battle situation. The low antenna height of ship-borne systems means that surface detection by unfriendly ESM systems is usually limited by the curvature of the earth. In anaprop conditions however the radar emissions can be detected over a far wider area. Strong ducting of radio energy towards land (such as shown in Figure 6-4) can also lead to detection from inside areas that would usually be shadowed by local terrain. These effects could be used to launch future Anti-Radiation Missiles (ARMs) from longer ranges and help them to attack a ship more efficiently. The effectiveness of ship launched decoys against such attacks will also be significantly altered by the presence of ducting conditions.

Propagation models like NEMESiS are essential to understand how vulnerable platforms with radio and radar system are to detection and ARM attack. If this type of modelling were available in theatre then tactical measures could be taken to reduce the ARM threat if the local situation required.

6.8 Conclusions

Results produced by the NEMESiS littoral modelling approach outlined in chapter 5 have been visually compared to real data and shown to match qualitatively. This has given the confidence in the model to allow the analysis of phenomena recorded during radar trials in important operational theatres. Modelled results have been used as evidence to support various hypotheses

concerning the effects of ducting and their presence during a particular trial data collection. The variety of outputs and display methods available to the model has allowed the complicated radar performance effects of anaprop combined with a real scenario to be assessed.

It should also be noted that the effects of anaprop are not always detrimental to the performance of the radar system. NEMESiS modelling confirms this. Target returns are generally enhanced in super-refracting conditions and so smaller targets will be detectable as long as the system is flexible enough to cope with the increased clutter levels as well. The increased clutter may also provide some solutions to the problems it is causing as it could be used to derive information about the local environment. This information would allow an assessment of the current radar performance to be modelled and even allow the radar system to adapt to the conditions and ensure that good performance is maintained. Such a system is prototyped in the next chapter.

7 Environment Inversion

7.1 Introduction

The work in the previous chapters has shown that atmospheric refractivity can have an important impact on radar performance. Propagation models can predict these effects if there is enough information about the atmosphere to input into the model. Unfortunately, low-level evaporation ducts are difficult to directly measure from a ship platform. Normally a refractivity profile is measured using a radiosonde balloon launched from the ship. This method cannot usually collect the refractivity data for the first 20-50 metres in height above the sea surface due to the height of the launch, the local effects of the ship such as engine exhaust and the time taken for the radiosonde to sense the launch and start to send data. Low-level altitude evaporation ducts would almost certainly be missed. A ship will only usually launch two radiosondes per day and so conditions could change dramatically between launches. A method for assessing the low altitude refractivity in almost real-time would therefore add to the rapid environment assessment (REA) capability available on the ship.

Comparison of NEMESiS simulations with the trials data from HMS Gloucester, described in section 6.1, showed that a noticeable change in land clutter strength could be explained by the presence of an evaporation duct. This suggested that NEMESiS could be used as part of an inversion algorithm which would extract information on the local refractivity conditions from the radar clutter backscatter.

7.2   Method

The aim was to create an environmentally aware radar system, ENVAR, that could analyse real radar data (gathered in the trials described in Chapter 4), compare that data to simulated clutter data from NEMESiS, and use the comparison to estimate the duct height.

Initially the research concentrated on the evaporation duct phenomenon as it is a common maritime phenomena which has a simple theoretical description that is defined by a single parameter, the duct height (as shown in Figure 7-1).

Figure 7-1 Example of a refractivity profile of an evaporation duct

A prototype of an operational ENVAR system was designed around NEMESiS as shown by the flow diagram Figure 7-2. This system was then created using Matlab and recorded radar data was used to demonstrate that real-time radar

performance information could be produced for threat assessment and tactical decision making.
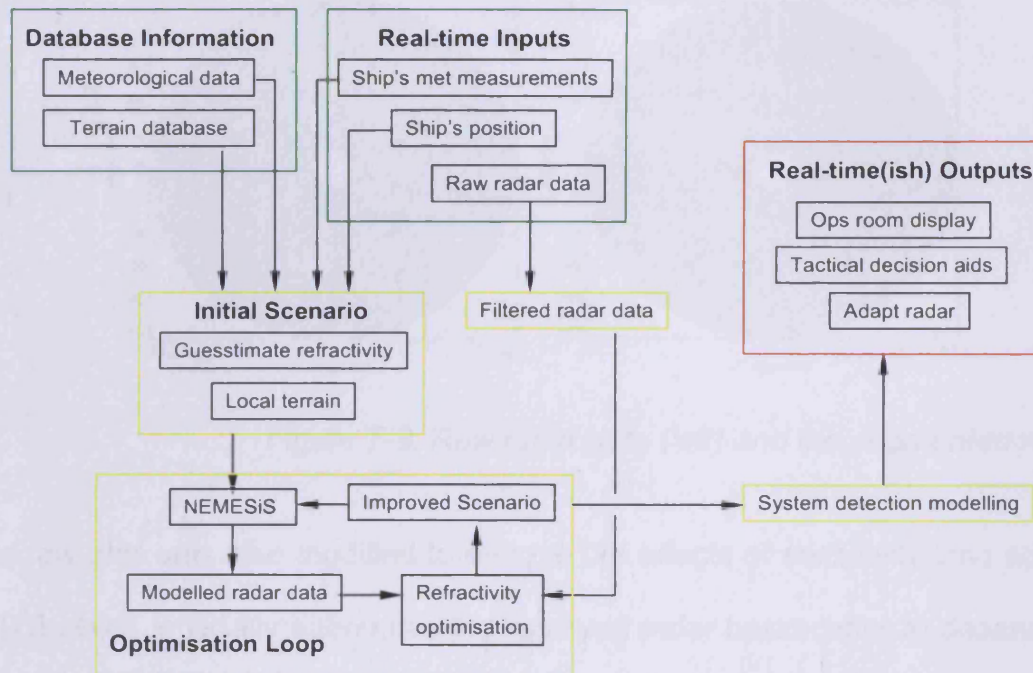
Figure 7-2 Environmental assessment system design

7.2.1 Raw data filtering

Sea clutter returns were chosen for the comparison because other types of clutter were found to be too site specific. Land clutter returns are heavily influenced by man made features and so cannot be predicted accurately from grid point terrain databases. Sea clutter is a function of wind strength and direction and so could be modelled for comparison with real data. Therefore the raw radar data needed to be filtered in order to exclude land clutter and other targets. This data was excluded by segmenting the radar data using terrain database information and amplitude filtering of the clutter radar returns, as

shown in Figure 7-3 by an example of a PPI view of some real data and the segmentation mask used to mask out unwanted clutter data.
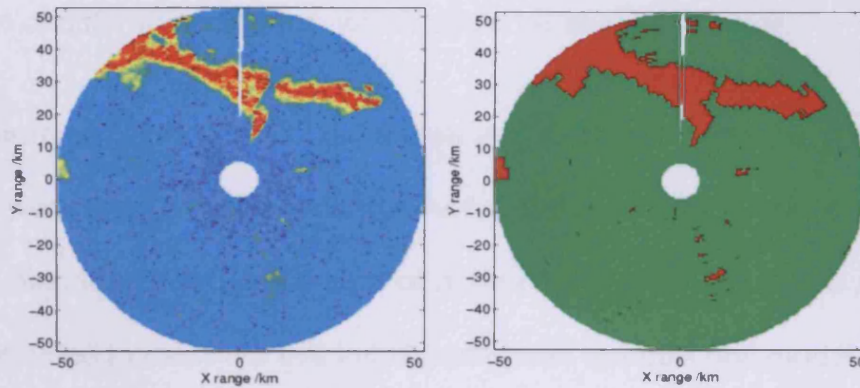
Figure 7-3: Raw radar data (left) and the segmented result

The raw data was also modified to remove the effects of sensitivity time control (STC) which artificially attenuates the received radar backscatter to desensitise the radar so that the likelihood of receiver saturation from clutter near to the radar is reduced. The effect of receiver noise in combination with this STC meant that the inversion technique was found to be limited to stronger winds which have high enough sea clutter levels to exceed this STC attenuation.

Once the filtering algorithm had provided raw sea clutter data, the data was smoothed by averaging over an azimuth sector.

7.2.2 Meteorological data

In an operational system, two types of inputs would be available on the ship's data highway; encyclopaedia data (historical meteorological data and terrain data) and real-time data measured on-board the ship (current meteorological conditions, ship's position and radar data). For the implementation of the

prototype system, this information was read in from plain text and Matlab data files. With the aid of radar data collected on ship trials, this allowed the simulation of different scenarios, which could be studied in detail.

Bulk meteorological data, such as the sea and air temperature, air pressure and humidity, were used to estimate a start value for duct height in order to give the inversion algorithm the best chance of achieving a good result in a short time. The model used to calculate this initial profile was the bulk flux model for the air-sea boundary layer developed by the Tropical Ocean Global Atmosphere (TOGA) programme and the Coupled Ocean Atmosphere Experiment (COARE) [Fairall et al, 1996]. Using the TOGA COARE model, the inversion algorithm took the full set of routine meteorological measurements that were made on board ship and calculated an estimate for the duct height [Babin, 1997].

As a backup to this process, or if the meteorological measurements were incomplete, then statistical duct height information was taken from the Ducting Climatology Summary (DCS) [SPAWAR, 1992], a global database of ducting conditions as recorded by 922 radiosonde stations over 15 years. The nearest station was calculated using the ship's GPS measurements. Then the average duct height for the region for the appropriate time of year was extracted from the database.

This estimated duct height was turned into a refractivity profile for use in NEMESiS by using the Hitney model [Paulus, 1990] of the evaporation duct which was given by the equation:

$$M(z) = M_0 + 0.13z - 0.13\delta \ln\left(\frac{z + z_0}{z_0}\right)$$

Equation 7.1

where M_0 was the value of the modified refractivity at the sea surface, δ (in metres) was the evaporation duct height and z_0 (in metres) was the aerodynamic roughness parameter (usually set to 1.5×10^{-4} metres). M_0 was set to 415 in the ENVAR prototype. The actual value for M_0 had no affect on the simulation because it is the gradient of the refractivity profile that affects radar propagation not the absolute values.

The Hitney model was also used to produce new refractivity profiles during the optimisation process when the trial evaporation duct height is being adjusted.

7.2.3 Sea state and wind speed estimation

If the wind speed at the time that the radar data was taken was available, then this was used as an input parameter for the optimisation loop.

If the wind speed for a set of data was unknown then a comparison of the first ten data points was made in order to obtain a good match at close range. This is because the greatest variation in radar signal strength for varying wind speeds is found close to the radar. The effects of ducting on clutter are also minimised close to the radar. Figure 7-4 shows simulated clutter profiles for a range of wind speeds (corresponding to average wind speed for each sea state). By comparison with the real radar profile (two examples of which are

shown in the figure) it was possible to estimate the wind speed from the sea clutter returns.
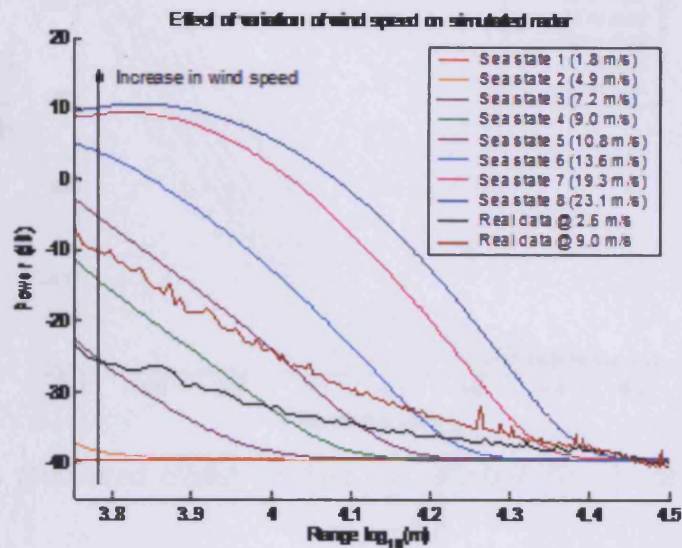
Figure 7-4 Simulated and real radar data for varying wind speeds

7.2.4 Optimisation loop

In the optimisation phase, NEMESiS was used to produce a series of clutter versus range profiles (an example is shown in Figure 7-5) on a coarse grid of duct heights for the estimated sea state with a realistic noise floor added to the data.
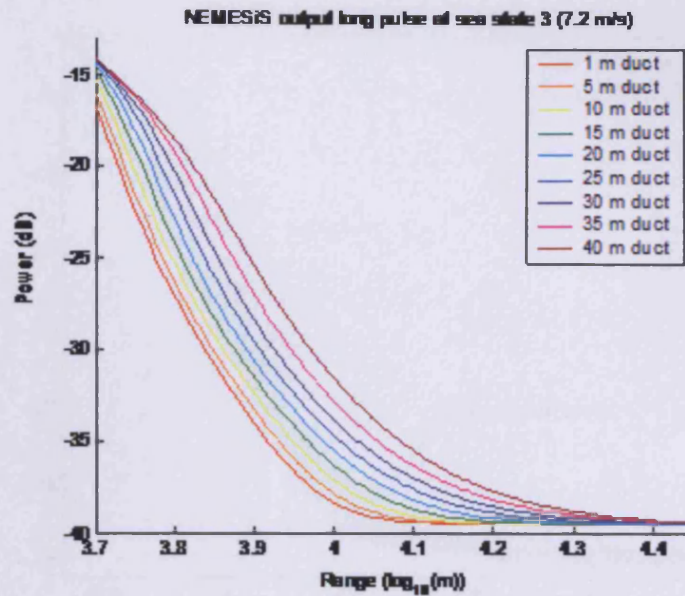
Figure 7-5 Simulated clutter profiles for different duct heights at a fixed wind speed

The best fit between the real and modelled data was then calculated using an area difference method shown in Figure 7-6. This process was repeated between two best fits using a finer grid to produce a duct height estimate to the nearest metre.

Comparison of real and simulated radar data
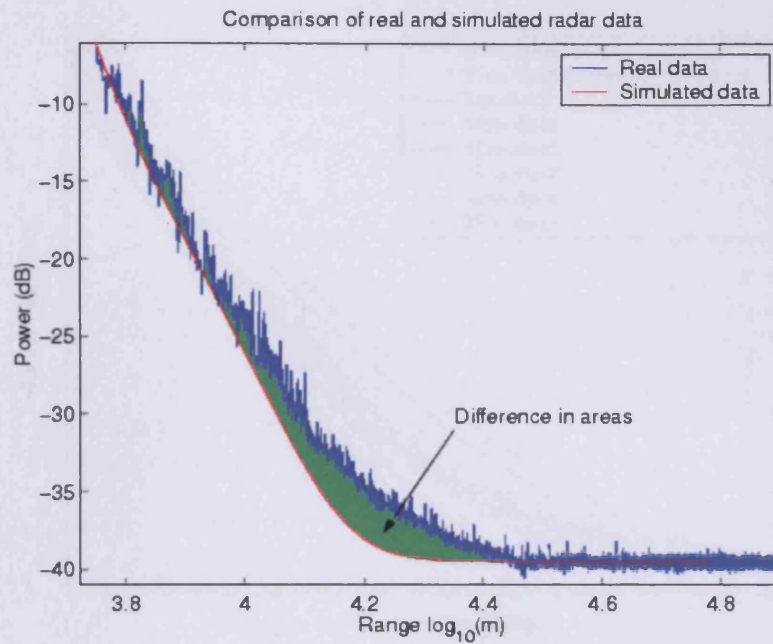
Figure 7-6 Illustration of the difference between the real and simulated radar data

Figure 7-7 shows NEMESiS results for a number of duct heights overlaying the

one set of real radar data. The optimisation loop rapidly chose a duct height of

21 metres in this case.
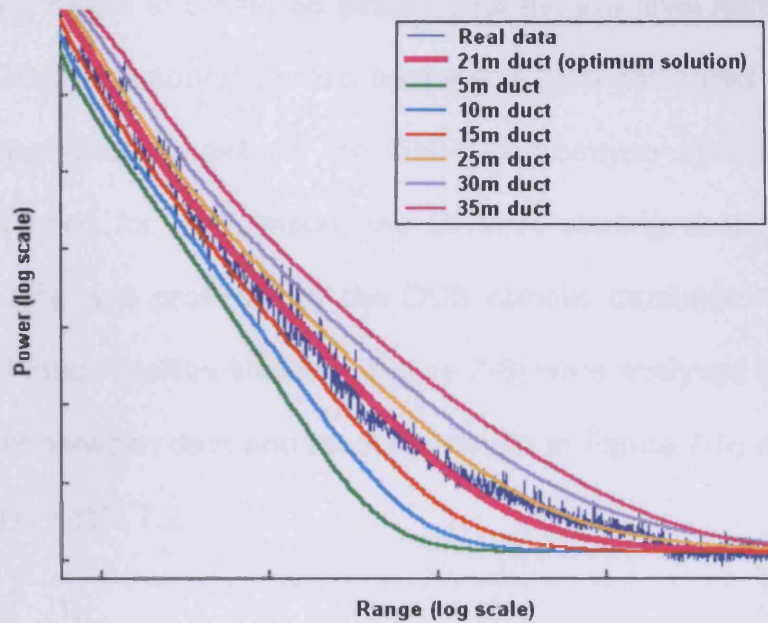
Figure 7-7 Comparison of radar data with NEMESiS simulated data for various duct heights

7.3 Testing

Due to the problems of measuring the evaporation duct with a radiosonde, there was no low-level truth refractivity data to test the algorithm directly. This made it difficult to verify the results from the analysed radar data.

No meteorological data were taken during the HMS Gloucester trial so only the ENVAR duct heights could be calculated to show that the algorithm was working efficiently. Much of the radar data gathered during this trial exhibited a strange receiver noise problem which prevented ENVAR from working properly. Two runs were successfully analysed and the results are tabulated in Table 7.1.

Fortunately, detailed meteorological records were recorded during the HMS Illustrious ship trial. These records were used as inputs to the TOGA-COARE

boundary layer model to create an estimate for the low-level refractivity profile. The TOGA-COARE evaporation duct height was then compared with the result from the optimisation routine in the ENVAR prototype system. As TOGA-COARE was used for comparison, the ENVAR starting duct height for the optimisation loop was provided by the DCS climatic database. Six runs (with clutter versus range profiles shown in Figure 7-8) were analysed (an example of an optimum fit between data and model is shown in Figure 7-9) and the results are recorded in Table 7.2.

7.4   Results

This section shows the results of the analysis of the two trials using ENVAR.

HMS Gloucester trial run No.	ENVAR duct height (m)	Estimated wind speed (m/s)
0057	32	9.0
0058	31	8.4

Table 7.1 Results from HMS Gloucester trial runs
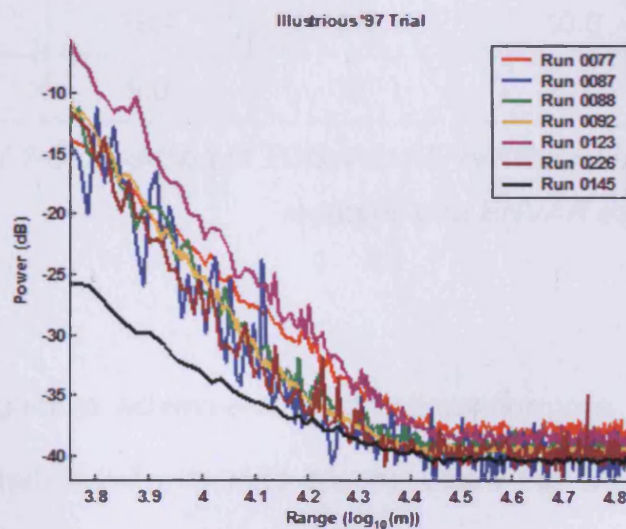
Figure 7-8 Comparison of analysed Illustrious '97 trial runs
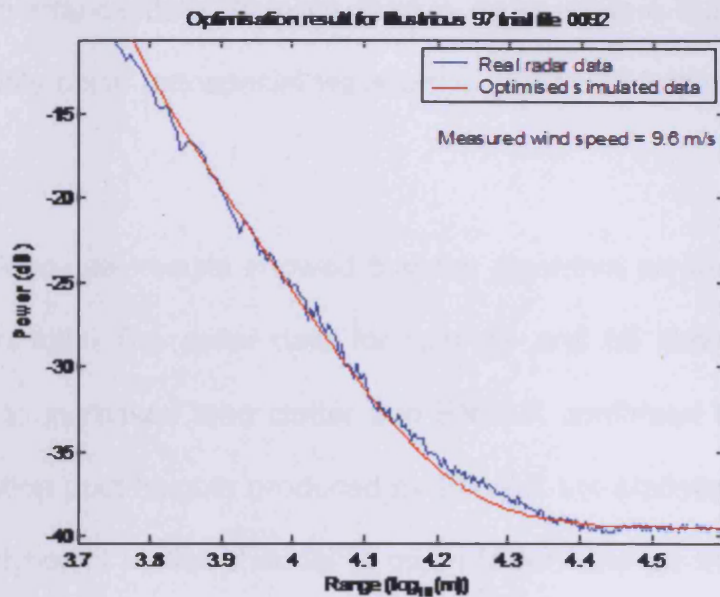
Figure 7-9 Example of an optimised fit of simulated data to real T996 trial data

HMS Illustrious trial run No.	TOGA duct height (m)	ENVAR duct height (m)	Recorded wind speed (m/s)	Estimated wind speed (m/s)
0077	17.2	47	11.3	8.2
0087	13.8	30	7.7	8.8
0088	13.3	31	9.3	8.9
0092	13.0	31	9.6	8.9
0123	18.4	35	10.3	9.5
0226	9.0	27	8.7	8.9

Table 7.2 Comparison of TOGA and ENVAR duct height estimates and recorded and ENVAR estimated wind speed

7.5   Analysis

The ENVAR algorithm achieved a rapid optimisation to a duct height for sea states greater than 3 (~7 m/s wind speed). Below this wind speed there was insufficient sea clutter to noise ratio to optimise the duct height from the

gathered surveillance data. A more flexible radar system than the one used during the trials could use special waveforms to provide better results at lower sea states.

The HMS Gloucester results showed that the algorithm worked and produced reasonable results. The radar data for runs 57 and 58 showed evidence of ducting due to increased land clutter and ENVAR confirmed that assumption. The evaporation duct heights produced by ENVAR are statistically unlikely, the average duct height in the channel is much lower, and so the estimates are probably too high.

The Illustrious TOGA-COARE results show that evaporation ducts were commonly present in the South China Sea. The ENVAR estimate of the evaporation duct height is consistently greater than the TOGA-COARE estimate. The trend shown by ENVAR does seem to match with TOGA-COARE. Where TOGA-COARE has indicated a higher duct than average, the ENVAR estimate is also higher.

There are several reasons why the ENVAR output might overestimate the duct heights. Firstly the clutter model that was used in NEMESiS may be underestimating the level of clutter returns and so a much larger duct is output to match the data in the radar. Also the clutter model might not match the circumstances of the trial very well. Sea clutter models are fits to experimental data in fully developed deep ocean sea conditions. For example many of the data sets were collected in fairly confined waters and so the sea conditions may

not have been the same height as would be expected from deep ocean wave theory. However, it is likely that one of the data sets would have matched if this were the reason whereas the differences seem to be systematic rather than random. A more advanced clutter model with more free parameters may have produced better results but would also take longer to reach an optimal value. The radar system design may have caused the error because despite having an excellent knowledge of the radar system design the duct heights produced were found to be sensitive to the STC law correction and the noise source modelling applied by ENVAR.

The ENVAR system has been designed in a fairly theoretical way and shows that the concept should work. If an ENVAR system were installed on a ship then the system could be trained and the clutter model could be tuned during sea trials to match to the radar system and give consistently better duct height results.

7.6 Real-time radar performance

Once the duct height had been estimated, the performance of the radar system against specific targets was calculated for the local scenario using NEMESiS to produce real-time pictures to assist with tactical decision making. For example, in certain atmospheric conditions decreased radar performance against threats coming from over the land might require the ship to be moved to maintain acceptable levels of defence. In other cases the operating mode of the radar might be changed to maintain levels of performance (for example using the

method for increasing the number of guard pulses and reducing the long range waveforms described in section 6.4.2)

7.7 Conclusions

Clutter profile inversion using DTED, NEMESiS, TOGA COARE, and DCS could be a candidate REA technique for shipborne radar operating in evaporation duct conditions. A prototype software system (summarised in Figure 7-10) has been completed that can estimate evaporation duct height and sea state from real data gathered in a variety of locations. The system developed shows how the improved clutter model developed for NEMESiS can provide another degree of freedom (clutter strength) for solving the atmospheric inversion problem although more optimisation would be needed to reach a more accurate solution.

Combining REA from radar backscatter with a good littoral radar model would give ship's personnel a real-time insight into their radar's performance. An operational system could be linked to future radar systems or retrofitted to existing systems to improve their flexibility.

In the future, linking REA information into a next generation flexible radar system, with adaptable waveforms and signal processing, would create an environmentally aware radar capable of working optimally in all types of refractivity and littoral conditions.
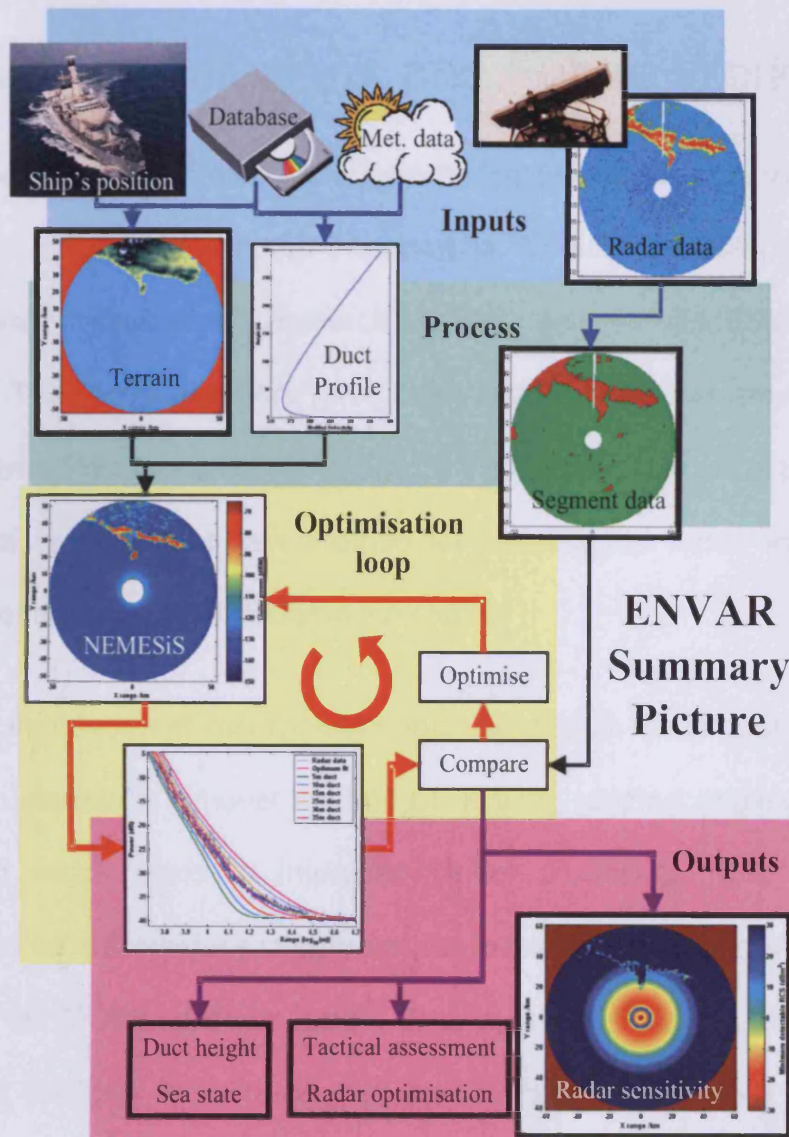
Figure 7-10 Schematic system design

8 Summary, Conclusions and Future Work

Several new sets of trials data were collected in different regions of the world to demonstrate a variety of anaprop phenomena. To fully understand this data an efficient new propagation research model called NEMESiS has been developed. The model and data have been used to demonstrate the important radar system effects caused by anaprop. The model has also been used to demonstrate an important new method for sensing the radar environment to assist with effective tactical decision making.

The major improvement incorporated into NEMESiS in comparison to other propagation models is a novel method of deriving grazing angles and surface propagation which leads to improved clutter modelling. This has allowed NEMESiS to be successfully integrated into existing radar performance models to upgrade the MOD's ability to model radar systems. This has led to improved assessment methods to be developed that support procurement of new naval systems such as SAMPSON, ARTIST, and MMR.

This thesis has examined the effects of the radar environment on shipborne radar systems using the NEMESiS model and real data collected from operational military radar on deployment in the English Channel, the Red Sea, and the Persian Gulf. Analysis of the trials data has confirmed that the detrimental anaprop effects on radar are:

- Radar coverage becomes skewed near the horizon
- Radar coverage is lost along some angles

- Unexpectedly high clutter backscatter

- Clutter is seen at unusually long ranges

- Emission control is compromised

- Hourly variation of signal and clutter

These basic physical phenomena lead to the following system issues for surveillance radar operation:

- System is unable to cope with high clutter signal strength

- Saturation and clipping within the receive chain

- Range ambiguous clutter folding

- Failure of clutter processing

- Effects are invisible to radar operators

- False alarms

All of these phenomena can now be modelled using NEMESiS.

The new clutter model in NEMESiS has also allowed a novel method of atmospheric refractivity measurement to be developed. The prototype system created from this idea has successfully predicted evaporation duct height trends for radar data gathered during trials.

The NEMESiS model should be continuously updated to take advantage of improving PC speeds to simulate more realistic radar clutter output to continue to enhance our understanding of the effect of anaprop on the radar system. Beyond the scope of the work reported in this thesis, NEMESiS has recently been used to generate realistic false alarms and target plots in real-time to test radar tracker algorithms. NEMESiS has also been used to inject almost real-

time baseband data containing noise, clutter and targets into a real radar system to test signal processing algorithms. These simulation capabilities should be improved to create a suite of low cost, repeatable radar tests for radar procurement and testing.

Further work is required to look at whether propagation effects can be mitigated or even be used to gain new information about how well a radar system is operating. The refractivity assessment prototype developed during this work should be tested in an operational system to prove its efficacy. Ways in which this information could be integrated into tactical decision making aids also requires further investigation.

NEMESiS should be integrated into the procurement process for the sensitive radar systems of the future as they will have to cope even more effectively with environmental phenomena. This will ensure that these systems will be able to perform well in theatres all around the world to support changing operational needs.

9 Bibliography

Ayasli, S. 'SEKE: A computer model for low altitude radar propagation over irregular terrain', *IEEE Transactions on Antennas and Propagation*, 34(8), Aug 1986 , Page(s): 1013 - 1023

Babin, S.M. et al 'A New Model of the Oceanic Evaporation Duct', *J Applied Meteorology*, 36, Mar 1997 , Page(s): 193-204

Barrios, A.E. 'A Terrain Parabolic Equation Model for Propagation in the Troposphere', *IEEE Trans. Ant. & Prop.*, VOL. 42, NO 1, 1994

Barton, D. *Radar Systems Analysis* , Artech House, 1988

Billingsley, J.B. *Low angle land clutter*, William Andrew Publishing, 2002

Blake, L.V. *Radar Range-Performance Analysis*, Lexington Books, 1980

Bracewell R.N. *The Fourier Transform and Its Applications, Second Edition*, McGraw-Hill, 1986

Branson, J. *Comparison of Naval Radar Propagation Models*, DERA, Unpublished MOD report, 1996

Branson, J. *Naval Environment, Clutter, Attenuation and Propagation Specification*, QinetiQ, Unpublished MOD report, 2006

Brigham, E.O. *The Fast Fourier Transform*, Prentice-Hall, 1974

Clark, Maj. G. C. 'Deflating British Radar Myths of World War II', Air Command and Staff College, March 1997

Craig, K.H. Levy, M.F. 'Parabolic equation modelling of the effects of multipath and ducting on radar systems', *IEE Proc. F*, 138(2), April 1991, Page(s): 153-162

Devereux, W.E. Van Egmond, J. 'Effects of ducting on radar operation in the Persian Gulf', *Proceedings of the 1989 IEEE National Radar Conference*, Mar 1989

Dockery, G. D. and Kuttler, J. R. 'An Improved Impedance-Boundary Algorithm for Fourier Split-Step Solutions of the Parabolic Wave Equation', *IEEE Trans. on Ant. & Prop.*, 44 (12), 1996

Dockery, G.D. 'Modelling Electromagnetic Wave Propagation the Troposphere Using Parabolic Equation', *IEEE Trans. Ants and Prop*, VOL. 36, NO 10, 1988

Dockery, G.D. 'Method for modeling sea surface clutter in complicated propagation environments', *IEE Proceedings*, PART F, 137, 1990

Domb, C. & Pryce M. H. L. 'The calculation of field strengths over a spherical earth', *JIEE*, 94, 1947, Page(s): 325-339

Fairall, C.W. et al 'Bulk parameterization of air-sea fluxes for Tropical Ocean Global Atmosphere Coupled Ocean Atmosphere Response Experiment', *J Geophys Res-Oceans*, 101:(C2) , Feb 1996, Page(s): 3747-3764

Gerstoft, P. Gingras, D. F. Rogers, L. T. Hodgkiss, W. S. 'Estimation of Radio Refractivity Structure Using Matched-Field Array Processing', *IEEE Trans. Ant & Prop*, Mar 2000

Hardin, R. H. and Tappert, F. D. 'Applications of the split-step Fourier method to the numerical solution of nonlinear and variable coefficient wave equations', *SIAM Review*, 15, 1973

Horst, M. M., Dyer, F. B., and Tuley, M. T. 'Radar Sea Clutter Model', *1978 Int. IEEE AP/S URSI Symp*, URSI DIGEST, 1978, Page(s): 6-10

IEE Mtg, 1998 'IEE EUREL Meeting on Radar and Sonar Signal Processing', , July 1998

Kerr, D.E. *Propagation of short radio waves*, Dover, 1965

Leontovich, M. A. & Fock, V. A. 'Solution of the Problem of Propagation of Electromagnetic Waves Along the Earth's Surface by Method of Parabolic Equations', *J. Phys USSR*, VOL. 16, NO. 7, 1946

Levy, M.F. *Parabolic Equation Methods for Electromagnetic Wave Propagation*, IEE, 2000

Lin, C.C. & Reilly, J.P. 'Application of Propagation Models to Terrain Clutter and Target Masking Viewed by a Shipboard Radar', *Proc. Em Prop. Workshop*, 1995, 1995

Mabogunje, A. & Branson, J. *DLQ trials report*, DERA, Unpublished report for MOD, 1997

Marcum, J.I. 'A statistical theory of target detection by pulsed radar', *IRE Trans. Information Theory*, IT-6, 1960, Page(s): 59-268

METOC 'The effects of the environment on radio and radar wave propagation', *Naval Oceanography and Meteorology*, MEMORANDUM NO1/94, Sept 1994

Moon, J.R. & Moon, J. *Land clutter analysis and synthesis*, JM9001, Unpublished MOD report, Jan 1996

National Audit Office *Accepting equipment off-contract and into service*, National Audit Office, Report by the Comptroller and Auditor General, 2000

Patterson, W. L. Hattan, C. P. Hitney, H. V. Paulus, R. A. & Anderson, K. D. *IREPS (Integrated Refractive Effects Prediction System) 3.0. (User's Manual)*, , Software user manual, 1987

Paulus, R.A. 'Evaporation Duct Effects on Sea Clutter', *IEEE Trans Ant & Prop*, VOL. 38, NO 11, 1990

Pierson, W. J. *The theory and applications of ocean wave measuring systems at and below the sea surface, on the land, from aircraft and from spacecraft*, NASA, NASA Contract Rep. CR-2646, NI6-17775, 1976

Pryce, M. H. L. 'The diffraction of radio waves by the curvature of the earth', *Adv. Phys.*, 2(5), 1953, Page(s): 67-95

Reilly, J.P. Lin, C.C. & Rudie, S.A. 'Land Clutter and Shadowing with Consideration of Propagation in Coastal Waters', *Proc RADAR '92 Conf*, IEE CONF. PUBL. NO 365, Oct 1992

Rogers, L.T 'Demonstration of an efficient boundary layer parameterization for unbiased propagation estimation', *Radio Science*, 33(6), Nov. 1998, Page(s): 1599-1608

Rogers, L.T & Wagner, L.J. 'The Effects of Grazing-angle Dependency on Evaporation Duct Heights Inferred from Radar Sea Clutter', *RTO MP-60*, Apr. 2000

Sayama, S. & Sekine, M. 'Advances in Radar Systems. Weibull Distribution and K-Distribution of Sea Clutter Observed by X-Band Radar and Analyzed by AIC', *IEICE Trans Commun (Inst Electron Inf Commun Eng)*, VOL. E83-B(9), 2000, Page(s): 1978-1982

Skolnik, M. I. *Introduction To Radar Systems*, McGraw-Hill, 1986

Skolnik, M.I. *Radar Handbook*, McGraw-Hill, 1970

Slade, S. Analysis of the Battle of Dong Hoi, 1996, http://www.navweaps.com/index_tech/tech-025.htm, viewed on 16/01/2008

SPAWAR Ducting Climatology Study (DCS), 1992, http://areps.spawar.navy.mil/, viewed on 20/04/2008

Tough, R.J.A. Ward, K.D. and Shepherd P.W. 'Electromagnetic Modelling of Radar Sea Spikes', *1st EMRS DTC Technical Conference*, EMRS DTC, 2004

Walker D. 'Doppler modelling of radar sea clutter', *IEE Proceedings - Radar, Sonar and Navigation*, 148, 2001, Page(s): 73-80

Ward, K. D. Tough, R. J. A. & Watts, S. *Sea clutter: Scattering, the K distribution and radar performance*, IET, 2006

Ward, K. D. Tough, R. J. A. Shepherd, P. W. 'Modelling sea clutter: correlation, resolution and non-Gaussian statistics', Radar 97, 1997, Page(s): 95-99

Watts, S. et al. 'The specification and measurement of radar performance', Radar 2002, Oct. 2002, Page(s): 542 - 546

Wu, C. 'Low altitude near-the-horizon propagation: A comparison between RPO and M-layer', Naval Postgraduate School, Monterey, CA, 1993

Yeoh, L 'An analysis of MLAYER: A multilayer tropospheric propagation program', Naval Postgraduate School, Monterey, CA, 1990

A   The Split-Step Parabolic Equation Algorithm

This section presents more of the theory behind the modelling methods used during this thesis. Much of the layout, equations, and diagrams are based on a QinetiQ memorandum report by James Basset (who worked with the author on methods for using propagation models in ship RCS measurement).

A.1   The parabolic equation

Consider the cylindrical co-ordinate system shown in Figure A-1. The electromagnetic wave propagates along the positive x-axis (the paraxial direction) and the radar is located on the z-axis above a perfectly flat, reflecting sea.
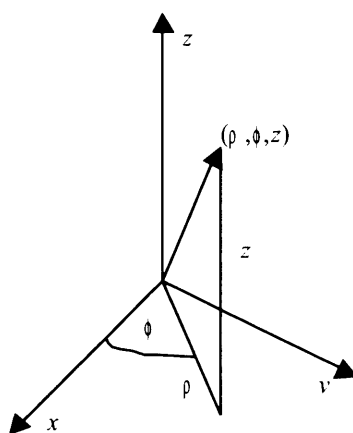
Figure A-1 Cylindrical co-ordinate system.

If the refractive index of the atmosphere is n and the wave number in free-space is k, the incident electric field obeys the Helmholtz equation (derived from Maxwell's equations):

$$\nabla^2 E + k^2 n^2 E = 0 \qquad\qquad Equation\ A.1$$

Assuming radial symmetry about the z-axis, the del-squared term is given by:

$$\nabla^2 E = \frac{1}{x}\frac{\partial}{\partial x}\left(x\frac{\partial E}{\partial x}\right) + \frac{\partial^2 E}{\partial z^2} \qquad\qquad \text{Equation A.2}$$

The refractive index will vary with range (x), height (z) and azimuth angle. In an atmosphere for which the refractive index varies slowly with both range and height, rapid variations in phase can be removed by defining an intermediate function $u(x,z)$:

$$E(x,z) = u(x,z)\frac{e^{jkx}}{\sqrt{x}} \qquad\qquad \text{Equation A.3}$$

Substituting this envelope function leads to a second order differential equation. The slow variation in refractive index along the x-axis (equivalent to range along the earth's surface) implies that this envelope function will also vary slowly meaning that:

$$\left|\frac{\partial^2 u}{\partial x^2}\right| << 2k\left|\frac{\partial u}{\partial x}\right| \qquad\qquad \text{Equation A.4}$$

This is the parabolic assumption. Dropping the 2nd differential in x term gives the parabolic wave equation:

$$\frac{\partial^2 u(x,z)}{\partial z^2} + 2jk\frac{\partial u(x,z)}{\partial x} + k^2\left(n^2 - 1\right)u(x,z) = 0 \qquad\qquad \text{Equation A.5}$$

The above expression can be solved numerically by finite element analysis although a computationally faster solution can be obtained by applying a Fourier transform to the equation.

For a radar, the intermediate function's solution, $u(x,z)$, depends upon the shape of the antenna radiation pattern $U(x,p)$. $u(x,z)$ and $U(x,p)$ form a Fourier transform pair and are related by:

$$U(x,p) = \Im(u(x,z)) = \int_{-\infty}^{+\infty} u(x,z)e^{-j2\pi pz}dz$$

$$u(x,z) = \Im^{-1}(U(x,p)) = \int_{-\infty}^{+\infty} U(x,p)e^{j2\pi pz}dp$$

Equation A.6

Applying the Fourier transform to equation A.5 and differentiating under the integral reduces it to a first order differential equation:

$$-4\pi^2 p^2 \cdot U(x,p) + 2jk\frac{\partial U(x,p)}{\partial x} + k^2(n^2 - 1) \cdot U(x,p) = 0$$

$$\therefore \frac{\partial U}{\partial x} = \left(j\frac{k^2(n^2-1)}{2} - j\frac{2\pi^2 p^2}{k} \right) \cdot U$$

Equation A.7

which may be solved as long as the refractive index is assumed to be constant across the region that U is being solved for. (Note that the differentiation under the integral step is only rigorous if u fulfils certain criteria. However more comprehensive methods give the same solution.)

A.2 Solution in free-space

For free space propagation a uniform atmosphere is assumed with the refractive index taken to be equal to unity at all ranges and altitudes. The solution is then:

$$u_{fs}(x,z) = \Im^{-1}\left[e^{-j\frac{2\pi^2 p^2}{k}x} \cdot \Im(u_{fs}(0,z)) \right]$$

Equation A.8

This expression is often used to model far-field radiation patterns using near-field measurements of antenna voltage.

A.3 Split-step Fourier transform

If we assume that the refractive index is constant with range over small range steps then the intermediate function u at range $x+\Delta x$ for all heights z, where Δx is small, can then be given in terms of $u(x,z)$ by:

$$u(x+\Delta x,z) = e^{j\frac{k}{2}(n^2-1)\Delta x}\,\Im^{-1}\left[e^{-j\frac{2\pi^2 p^2}{k}\Delta x}\,\Im\left(u(x,z)\right)\right] \qquad \text{\textit{Equation A.9}}$$

This is the split step solution to the parabolic wave equation and allows propagation problems to be solved by a marching technique. The initial electric field distribution is defined at the left boundary of the region through which the electromagnetic wave propagates. This distribution depends upon the shape of the source antenna radiation pattern. Two phase screens modify the electric field distribution at each range step as indicated in Figure A-2. One phase screen spreads the energy in height as it propagates outwards from the source. The second screen alters the wavefront's angular distribution to reflect the effects of the refractive index profile of the atmosphere. The range increment between each pair of phase screens is Δx.
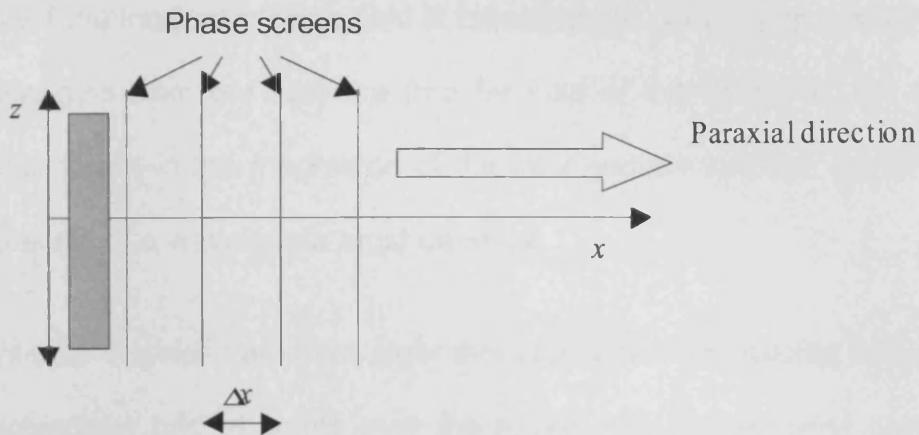
Figure A-2 Phase screens for the split-step Fourier transform solution.

The intermediate function $u(x,z)$ is assumed to be sufficiently well behaved that its Fourier transform $U(x,p)$ with respect to z (height) exists. This condition will be true for all electric field distributions that apply to real atmospheric structures [Dockery, 1988]. The Fourier variable p is vertical wavenumber and is equal to $k.\sin\theta$ where θ is the angle of elevation as shown in Figure A-3.
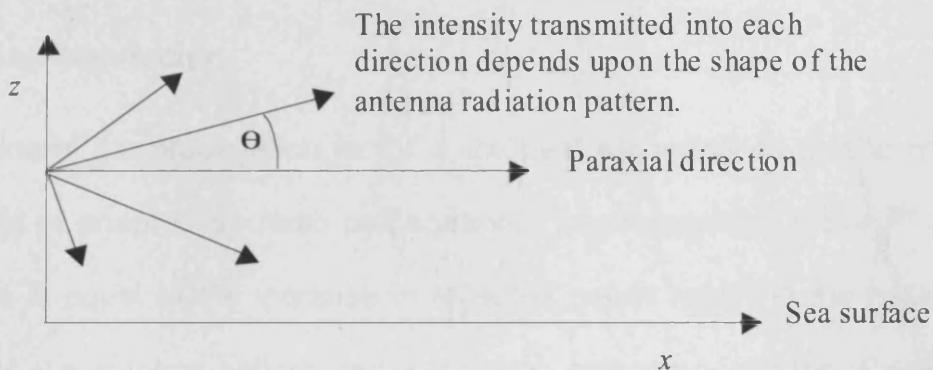
Figure A-3 Fourier variable p and angle of elevation above the horizon.

The solution for the intermediate function can therefore be marched forwards from the source antenna towards the target. Both the forward and inverse Fourier transforms can be calculated efficiently using a Fast Fourier Transform (FFT) algorithm [Brigham, 1974 and Bracewell, 1996]. The parabolic equation is

valid only if the incident electric field is calculated at points lying a large number of wavelengths from the antenna (the far field of the antenna). As assumed earlier, variations in the magnitude of the intermediate function *u* with range *x* over the scale of a wavelength must be small.

The split-step Fourier transform algorithm calculates the electric field strength on a rectangular grid of points over the region from the antenna outwards to where the marching loop is terminated. The maximum height and propagation angle used in the calculations define how many calculations are needed. An absorbing layer has to be applied so that the beam does not reach the upper boundary (which in principle ought to be at infinity). The number of points in the Fast Fourier transform depends upon the angular width of the antenna radiation pattern and the height increment along the z-axis.

A.4 Propagation factor

In general the propagation factor is the best parameter to plot to analyse the effects of anaprop on radio propagation. The propagation factor F^4 at a given range is equal to the increase in reflected power reaching the radar antenna due to the antenna pattern and/or anaprop compared with the situation for the identical scenario in free-space. In terms of the intermediate function (u) that is output from PE models:

$$F^4(x,z) = \left| \frac{E(x,z)}{E_{fs}(x,z)} \right|^4 = \frac{|u(x,z)|^4}{x^2 \cdot \lambda^2} \qquad \text{Equation A.10}$$

A.5   Refractive index profile

The refractive index of a well-mixed atmosphere depends upon its temperature, pressure and humidity. In a standard atmosphere at sea level, the value of the refractive index is equal to 1.000315 [Dockery, 1988]. To make use of simpler numbers, often the refractivity N is used instead where:

$$N = (n - 1) \cdot 10^6 \qquad\qquad \textit{Equation A.11}$$

The refractivity will decrease at about 0.04 N-units per metre in a standard atmosphere due to the rapid fall in humidity with altitude close to the sea surface. For a uniform atmosphere, the rays will follow roughly straight-line paths (there is a slight downwards curvature due to the refractivity variation with height). Because the surface of the Earth is curved, the altitude of a ray launched horizontally will tend to increase with range. Relative to an observer on the ground such a ray will appear to bend upwards (a process known as subrefraction) as shown in Figure A-4.
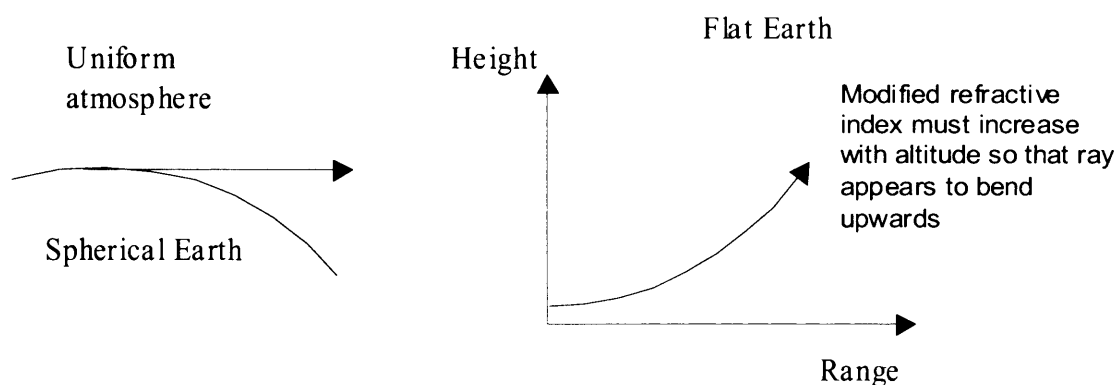
Figure A-4 Relationship between a spherical Earth and the modified refractive index.

Since only the relative phase of each electromagnetic wave matters, a flat Earth and a modified refractive index profile that increases in value with height can be used to model radar propagation over the sea surface. Assuming the radius of the Earth is a, the modified refractive index is then given by:

$$m(x,z) = n(x,z) + \frac{z}{a}$$

The radius of curvature of the Earth is approximately 6300 kilometres. Trapping occurs when the gradient of the modified refractive index is negative so that all rays tend to be bent towards the sea surface. Subrefraction occurs when the gradient of the modified refractive index is positive. When the modified refractivity is equal to zero, the ray will appear to maintain a constant height above the sea surface. In free-space (vacuum), the modified refractivity is equal to zero in all directions. The shape of the refractive index profile can be different at each range step provided the parabolic assumption of slow overall variation compared with the radar wavelength is not violated.

A.6 Effect of the antenna gain pattern

To be able to calculate the value of the intermediate function at each range increment, its starting value at zero range $u(0,z)$ must be defined. This depends upon the inverse Fourier transform of the antenna gain pattern, $g(\phi)$.

For calculations to estimate propagation factor factors, the intermediate function at zero range must account for the image antenna beneath the sea surface. This antenna interferes with the main beam to produce peaks and nulls in the

radar cross-section of the target. The image antenna is located at an apparent depth equal to height of the main antenna above the sea surface. Both of these antennas must be exactly out of phase with each other so that there is a null in the radar cross-section response at zero height and infinite range. It therefore follows that at zero range:

$$u(0,z) = \Im^{-1}[2j \cdot \sin(2\pi p h_r) \cdot g(p\lambda)]$$
Equation A.13

where h_r is the height of the antenna and the radiation pattern has been transformed to be a function of the Fourier variable p.

An important advantage of the split-step Fourier transform algorithm is that the effect of the shape of the antenna radiation pattern and the reflection off the sea surface is automatically included when the intermediate function is defined at zero range.

A.7   Testing PE results

The propagation factors estimated using the parabolic equation method can be tested by comparison with predictions using a simple multipath technique. This model attributes multipath interference to the effect of propagation along an indirect ray that undergoes specular reflection at the sea surface as indicated by the diagram in Figure A-5. It assumes that the distance between the radar and the target is short so that the curvature of the Earth can be ignored and that the atmospheric refractive index is uniform in all directions.
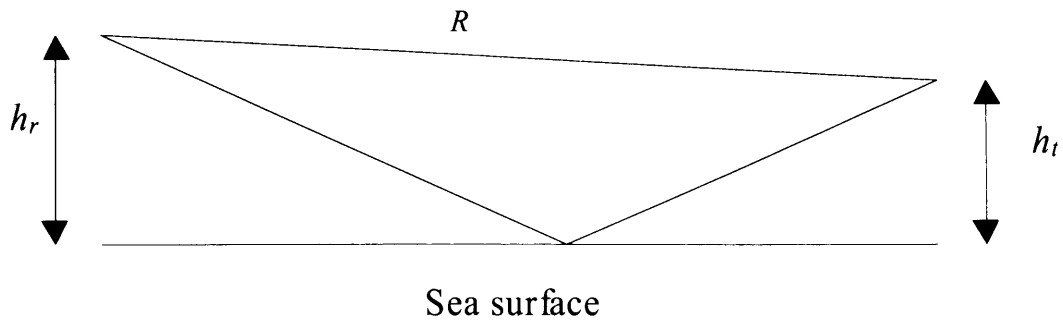
Figure A-5 Ray tracing geometry for comparative calculations of propagation factor for a uniform atmosphere and a flat Earth.

Assume a target at height h_t above the sea surface and a radar antenna with an isotropic radiation pattern. The propagation factor F^4 at range R given perfect reflection of the indirect ray at the sea surface is:

$$F^4 = 16\sin^4\left(\frac{2\pi h_r h_t}{\lambda R}\right)$$

Equation A.14

The maximum theoretical propagation factor is 12dB. This corresponds to a four-fold increase in the reflected electric field strength at the radar antenna.

This simple model can be compared to results produced by a parabolic equation model assuming constant refractivity field and an isotropic antenna. The results showed a perfect match.

More complicated testing can be carried out by comparison with standard cases produced from exact solutions or by other propagation models.

B Radar Coverage in Evaporation Ducts

This section demonstrates how increasing evaporation duct height leads to the onset of trapping using NEMESiS modelling.

B.1 Propagation factor coverage diagrams for 3.0 GHz

The following diagrams show the effect of evaporation ducting on the low angle radiation pattern of a radar antenna.
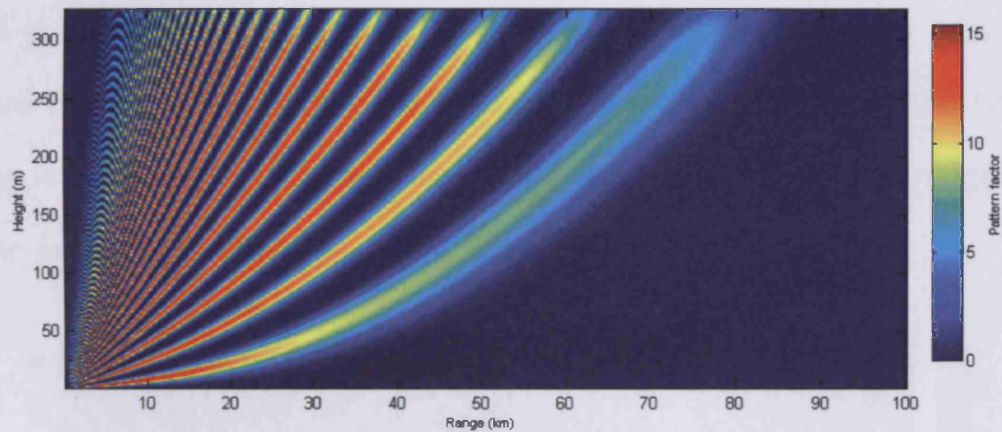
Figure B-1 Standard atmosphere (at 3.0 GHz)

In a 'standard' atmosphere, the coverage diagram Figure B-1 shows multipath lobing due to the interference of the energy from the antenna with its reflection from the sea surface. The interference pattern appears to curve upwards due to the transformation of the curved earth surface to lie along the x-axis (range axis). The surface clutter levels in this situation would fall off rapidly with range.
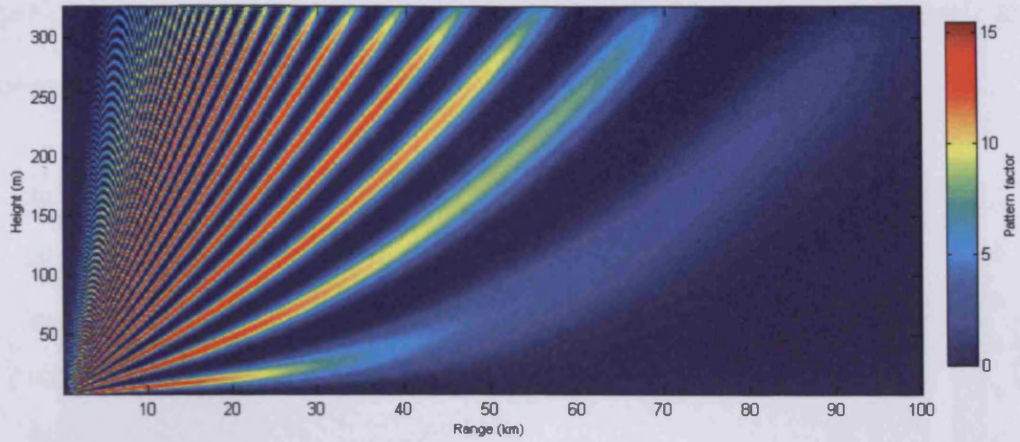
Figure B-2 15m Evaporation duct (at 3.0 GHz)

With a medium height evaporation duct the interference pattern (shown in Figure B-2) is shifted so that the upwards curvature is reduced. The horizon range is increased and clutter levels would be stronger at medium ranges and would extend beyond the normal radar horizon.
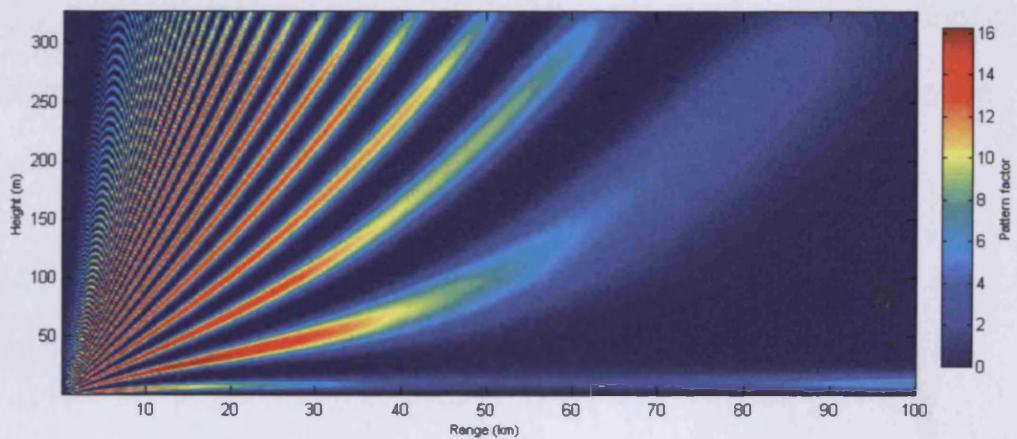
Figure B-3 34m Evaporation duct (at 3.0 GHz)

Figure B-3 shows the coverage for an evaporation duct of a similar height to the antenna height. Energy has become trapped in a waveguide along the surface of the earth. The horizon range is now infinite and detection close to the surface is possible at much longer range. Surface clutter will also be detectable at

longer ranges, possibly in regions which wouldn't normally need to be processed to remove clutter.
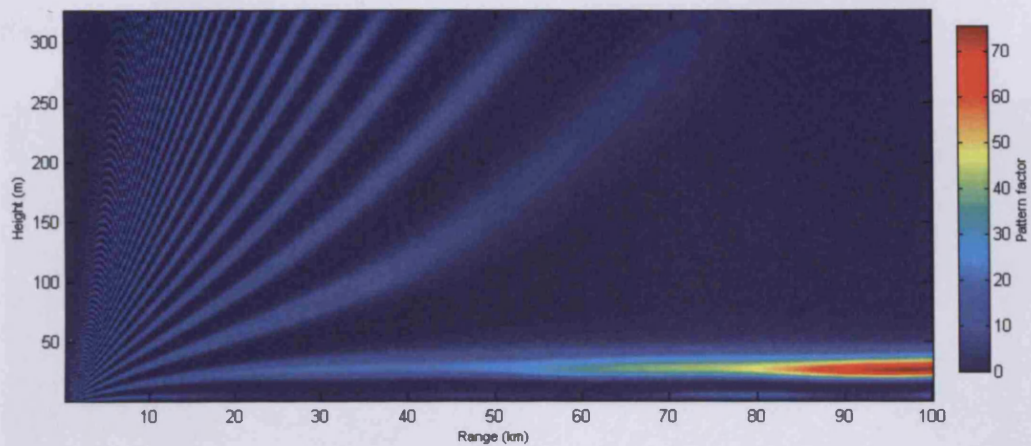
Figure B-4 50m Evaporation duct (at 3.0 GHz)

Figure B-4 shows how an even higher evaporation duct traps more energy and a new interference pattern begins to form inside the duct. At long ranges, large pattern factors build up as the assumption of spherical propagation breaks down as cylindrical propagation is the dominant mechanism. Stronger long range clutter returns are likely to affect target detection.

C   Further NEMESiS 3D Examples

This section presents further results from NEMESiS 3D and shows other studies that can be carried out using this model.
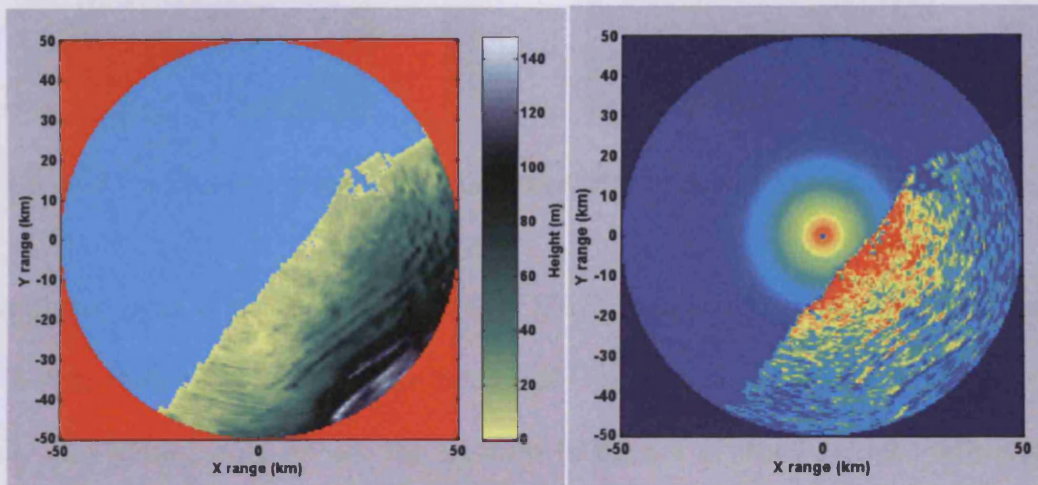
Figure C-1 A scenario and the clutter map produced for an MFR surveillance radar
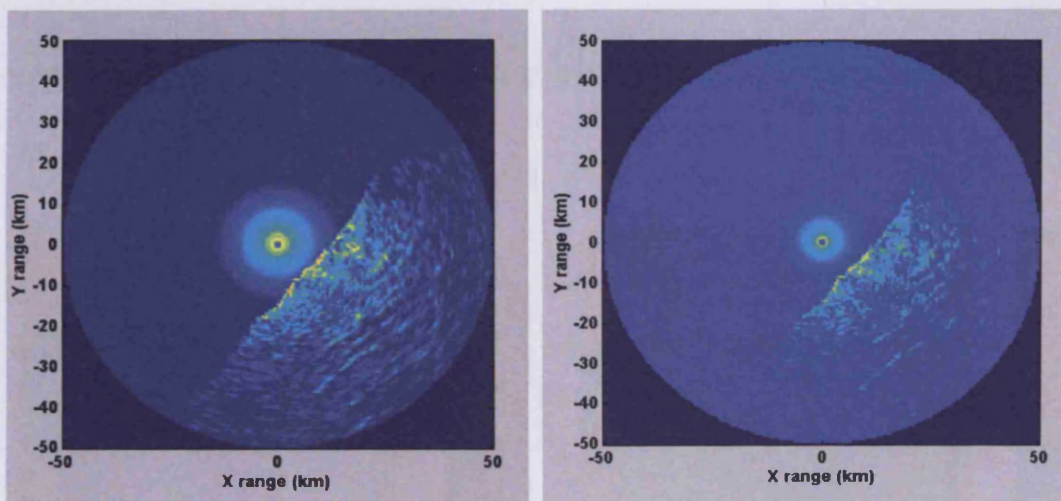
Figure C-2 Clutter maps for 2 short-range radar systems

The above plots (Figure C-1 and Figure C-2) show the simulated clutter return power generated for 3 radar systems with decreasing power-aperture products. NEMESiS predicts that land clutter will be a significant problem for the MFR surveillance radar.
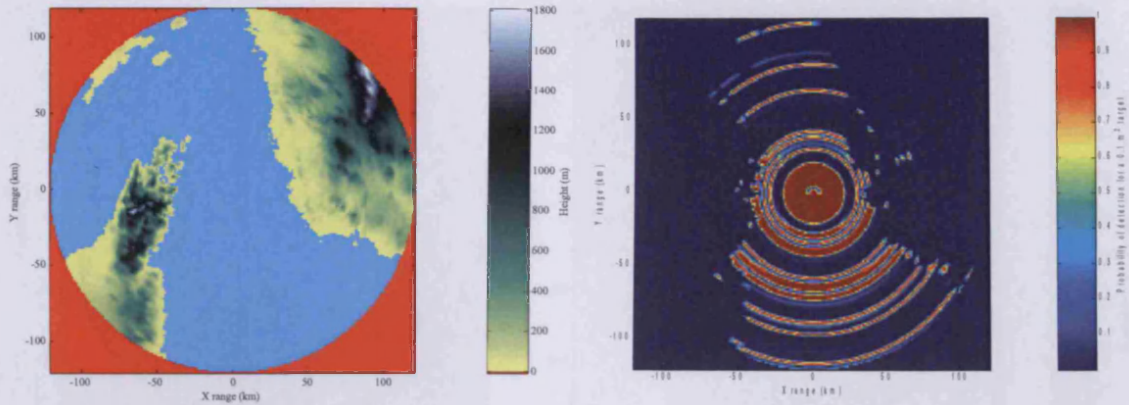
Figure C-3 A scenario and its associated probability of detection map for a surveillance radar system

The above plots (Figure C-3) show a NEMESiS simulation of radar performance for a ship radar approaching the Straits of Hormuz, the entrance to the Persian Gulf. The strong duct allows the system to detect a small target intermittently out to much larger ranges than would normally be possible.

Figure C-4 shows another scenario and the clutter power backscattered to the radar.
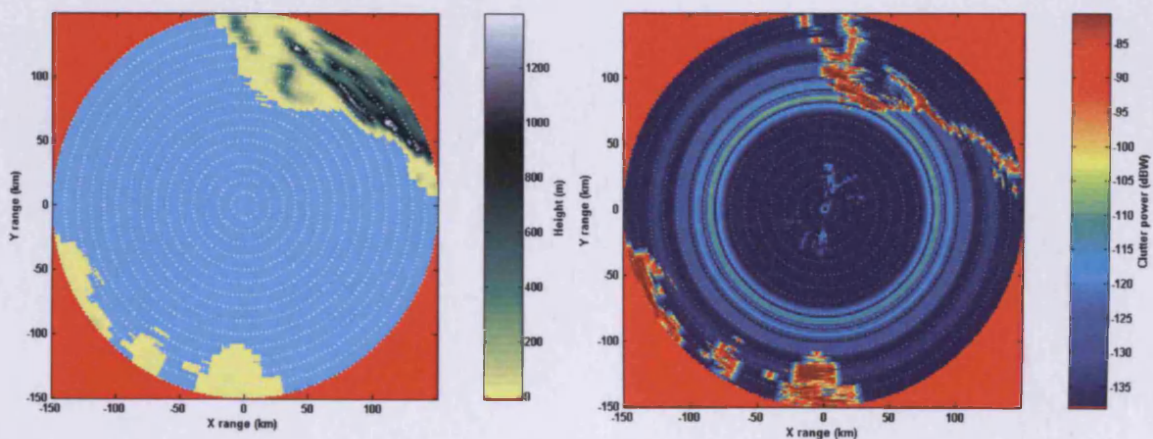
Figure C-4 anaprop Straits of Hormuz Scenario (left) and clutter model (right)

The plots in Figure C-5 compare target probability of detection for the above scenario for two small targets at different heights.
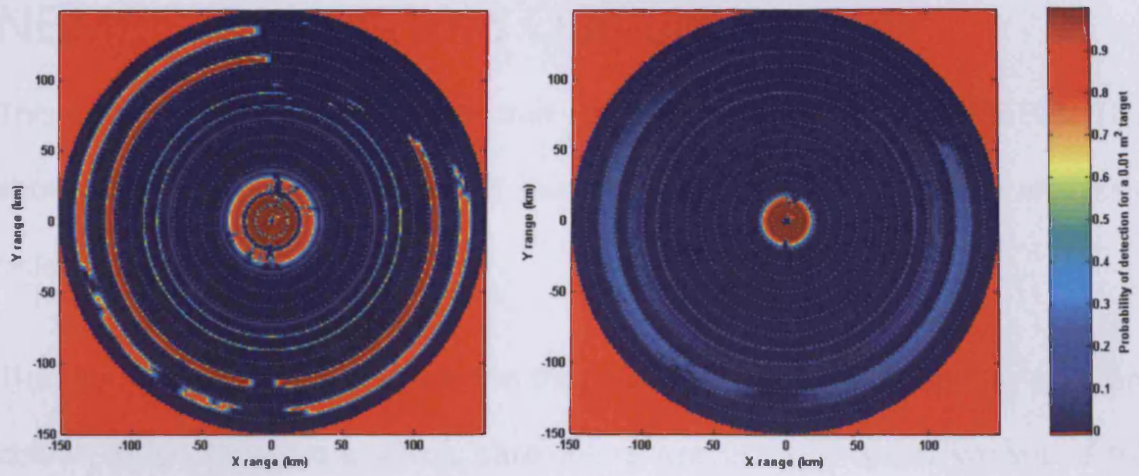
Figure C-5 Probability of detection for an ultra-small RCS target at an altitude of 50m (right) and 5m (left)

D NEMESiS Inputs and Outputs

This section lists the parameters that can be analysed using NEMESiS. This shows the flexibility (and some of the limitations) of the model for analysing radar systems.

The inputs and outputs are listed in the tables below. The parameter cells are colour coded to indicate which parameters are used in which variant of the NEMESiS model.

- Red cells indicate parameters only used in the 2D model.

- Light beige cells indicate parameters used only in the 3D model.

- Orange cells indicate parameters used in both the 2D and 3D models.

D.1 Inputs

Antenna position - Allows terrain data to be extracted from databases	Latitude (°)
	Longitude (°)
Calculation range – Define the size of the region to be modelled in 3D modelling	Maximum range (km)
	Azimuth resolution (°)
	Centre azimuth (°)
	Minimum azimuth (°)
	Maximum azimuth (°)
Environmental parameters –	Refractivity file

Define the environmental background for the scenario	**Terrain file**
	Terrain database (DTED, SRTM[11])
	3D Refractivity database
Calculation parameters – Define the detail level of the propagation modelling 2D slices	Maximum range (km)
	Number of range steps
	Maximum height (m)
	Maximum angle (°)
Radar parameters – Define the radar parameters necessary to calculate the propagation field for each 2D slice	Antenna height (m)
	Elevation beam width (°)
	Antenna pattern ('Sinc', etc)
	Antenna pattern file (filename)
	Elevation (°)
	Frequency (GHz)
System parameters – Defines the radar parameters needed to calculate the radar performance metrics once the propagation modelling is completed	Peak power (KW)
	Pulse duration (micro sec)
	Transmit gain (dB)
	Receive gain (dB)
	Noise (W/Hz)

[11]Digital Terrain Elevation Database, Shuttle Radar Tomography Mission

	Loss (dB)	
	Polarisation (VV or HH)	
	Azimuth Beam width (°)	
	Cancellation (dB)	
	CFAR	
Waveform parameters	Minimum range (m)	
	Maximum range (m)	
	Minimum azimuth (°)	
	Maximum azimuth (°)	
	Number of pulses	
	Cancellation (SNR improvement ratio)	
	Compression ratio	
External parameters - Defines the other scenario parameters needed to calculate the radar performance metrics once the propagation modelling is completed	Wind speed (m/s)	
	Wind direction (°)	
	Target RCS (dB)	
	Target height (m)	
	Land clutter type (model and terrain type)	
	Sea clutter type (model)	

D.2 Outputs

Radar equation outputs - The raw data produced by the propagation loop	Path loss Propagation factor Surface propagation factor Surface grazing angle (°)
Intermediate quantities - Calculated quantities that feed into the metrics	SNR CNR SNCR Detection threshold to noise ratio Clutter RCS (m^2) Clutter spikiness (Weibull and K)
Radar performance metrics - Examine the system effects either qualitatively or quantitatively	Clutter PPI simulation (with appropriate spatial statistical variation) False alarm rate Probability of detection

E   Further Trials Radar Data

Presented here are pictures of some of the other data extracted into Matlab during analysis of the HMS Richmond trial. The aim of this section is to show some of the other clutter phenomena found in real environments that are outside of the analysis in the thesis.
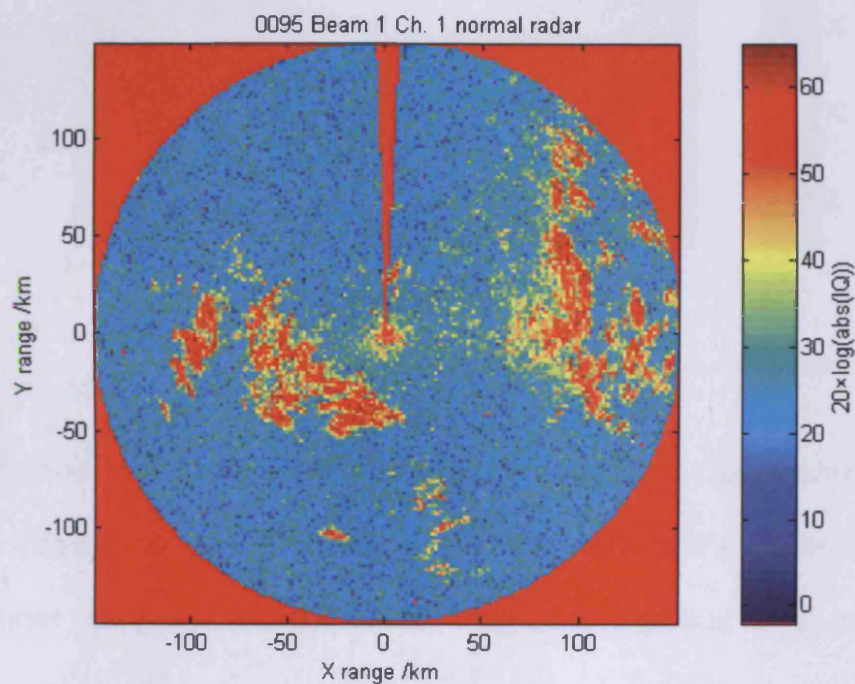
Figure E-1 Data from the Red Sea in normal radar mode

The plot above (Figure E-1) shows the increased level of sea clutter and interference between the ship and the land features to the East and West of the ship in anaprop conditions.

0113 Beam 1 Ch. 1 normal radar
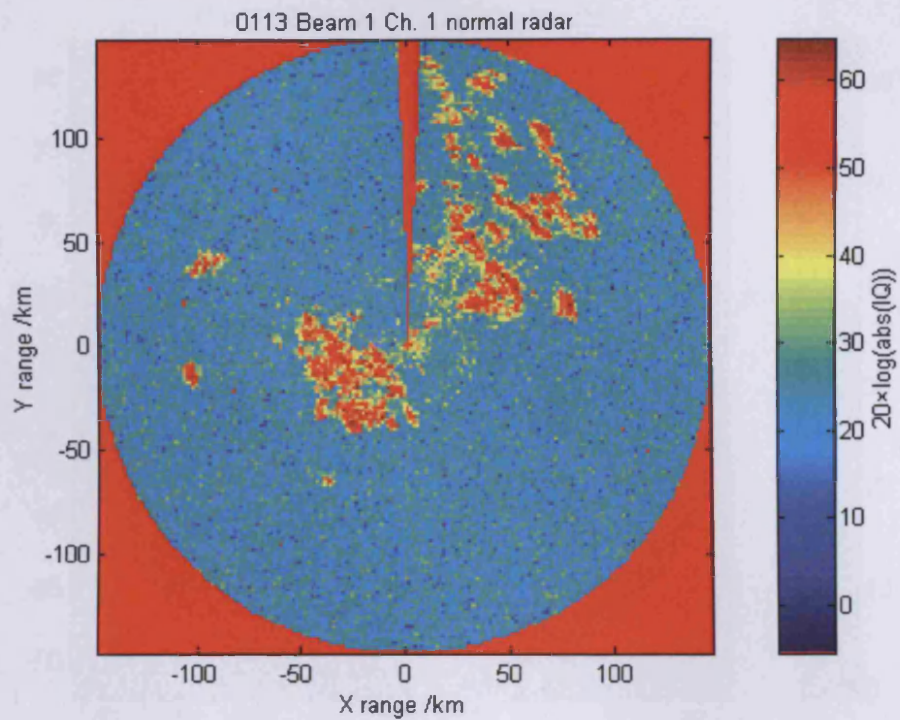
Figure E-2 Further Red Sea data in normal radar mode

Figure E-2 shows an example of strongly reflective land clutter shown by the red/orange regions to the north east and south west of the radar. There are areas of clutter close in to the radar which may be ambiguous range clutter.

Run 0296 Beam 1 Ch. 1 normal radar
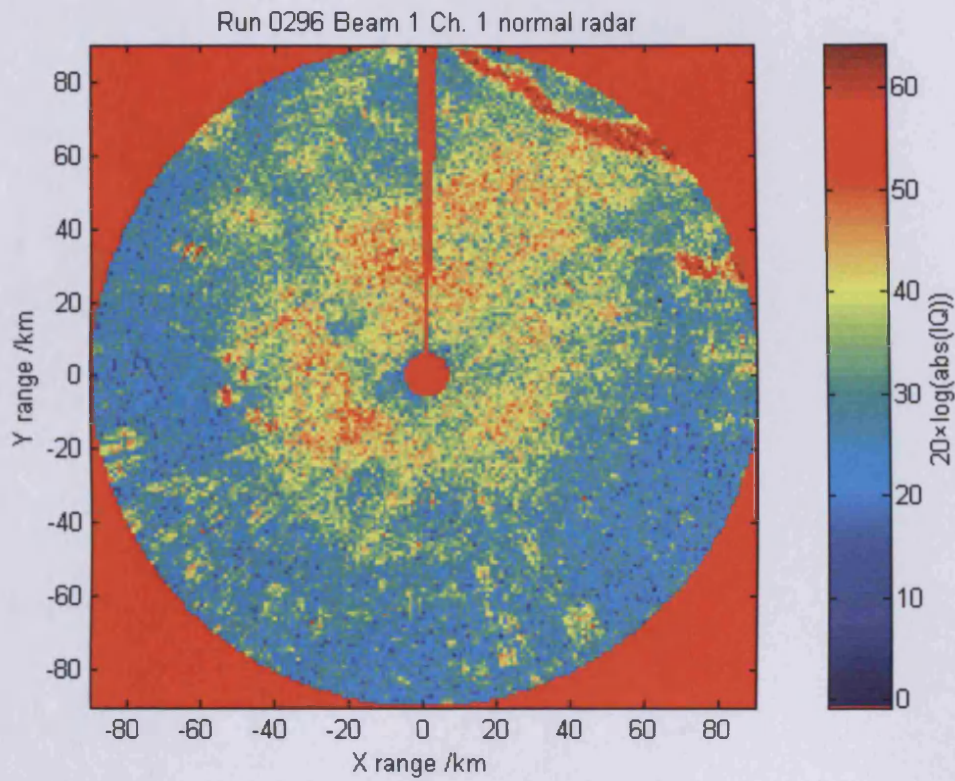
Figure E-3 Radar data showing rain clutter

The plot above (Figure E-3) shows strong clutter returns in heavy rain. Note that this clutter looks very similar to the increased levels of sea clutter seen in the presence of anaprop.